Title
Two-Dimensional Semiconductors for Next-Generation Optoelectronics

Author
Kim, Hyungjin

Publication Date
2021

Peer reviewed|Thesis/dissertation

Two-Dimensional Semiconductors for Next-Generation Optoelectronics

By

Hyungjin Kim

A dissertation submitted in partial satisfaction of the

requirements for the degree of

Doctor of Philosophy

in

Engineering – Electrical Engineering and Computer Sciences

in the

Graduate Division

of the

University of California, Berkeley

Committee in charge:

Professor Ali Javey, Chair
Professor Ming Wu
Professor Daryl Chrzan

Spring 2021

Abstract

Two-Dimensional Semiconductors for Next-Generation Optoelectronics

by

Hyungjin Kim

Doctor of Philosophy in Electrical Engineering and Computer Sciences
University of California, Berkeley

Professor Ali Javey, Chair

With the innovation of technologies that will impact our daily life such as the internet of things (IoT), wearable health care systems, digitally extended reality, and autonomous vehicles, the development of next-generation optoelectronic devices that possess advanced functionality and high performance has emerged as a substantial component for the evolution of future technology. Two-dimensional (2D) semiconductors have been extensively studied in the exploration of new phenomena and properties that are not seen in conventional bulk semiconductors, especially for optoelectronic applications such as light-emitting diodes (LEDs) and photodetectors. While the majority of existing technology relies on bulk crystalline semiconductors, unprecedented possibilities can be opened up for developing next-generation optoelectronics owing to the unique properties and the tuning capabilities that 2D semiconductors offer.

Chapter 2 presents the material processing approaches that are applied in atomically-thin semiconductor monolayers to enhance their luminescence efficiency. A combination of optimized doping and growth conditions enables extraordinarily bright luminescence in 2D transition-metal dichalcogenide (TMDC) monolayers with large scale and high stability.

Chapter 3 describes the first critical step towards highly efficient LEDs at all brightness using monolayer semiconductors. The fundamental limitations of degraded luminescence efficiency in 2D semiconductors at high photocarrier densities have been identified and overcome by applying small mechanical strain to the materials, leading to the complete suppression of nonradiatvie recombination at all exciton densities.

Chapter 4 demonstrates the room-temperature infrared optoelectronic devices whose operating wavelengths can be widely modulated by utilizing strain-tunable bandgap in black phosphorus. Mid-wavelength infrared (MWIR) LEDs with large spectrum tunability are developed and applied in non-dispersive infrared gas sensing technology. Highly-responsive photodetectors exhibit their detectivity exceeding those of state-of-the-art photodetectors with their detection wavelengths spanning from short-wavelength infrared (SWIR) to MWIR range.

To Yoonhee and Sophie Seowoo

Table of Contents

Acknowledgements

It has been a memorable journey until I write this page to try my best to give credits to everyone who made it possible. First of all, I would like to thank my mentor Professor Ali Javey who discovered small talents in me and offered me the opportunity to join his group. I was extremely lucky to have a Ph.D. training from him at Berkeley and I will keep every advice I received from him. He is not only a Ph.D. advisor to me but he also gave me a lifelong mentorship which helped me to become a better person. When I first arrived at rainy Berkeley, I was in my twenties and he was in thirties and now I am in thirties while he is in his forties. Although I could not be as wise as him at his age, I think I have learned from him how to become a good parent, teacher, and colleague for the people who will stay together with me.

Also, I would appreciate other professors for their fruitful guidance. Prof. Ming Wu, Prof. Daryl Chrzan, and Prof. Joel Ager gave me critical feedbacks during my qualification exam (which made me very embarrassed) and I still remember their new ideas and visions which were really insightful. I would like to specifically thank for their significant contributions to develop the theoretical backgrounds of my research. I was also truly grateful to have great guidance from Prof. Eran Rabani and Prof. Ken Crozier for my research projects. I cannot imagine completing my two important projects without their substantial advice and suggestions. My graduation would not have been possible without their guidance for the projects.

I was so lucky to be surrounded by the excellent people in our lab. Shiekh is the most brilliant and considerate person I met at Berkeley. Whenever I go to a new place and meet a new person, I would wish every colleague I will meet would be like him. So many days we have worked and discussed together (especially during the pandemic), laughed, got food, and joked together will be the one of the most enjoyable assets of my Ph.D. memory. Also, Danny, Matin, and Geun Ho were my great mentors, colleagues, and friends who helped me to start and learn many things in our lab. I really wish we can meet all together some day at a good place. Although I could not list everyone's name, I wish the best luck to everyone– Sujay, Fahad, James, Peter, Jerry, Joy, Matt, Vivian, Naoki, and Jonghwa.

About 13 years ago, I was just an unpredictable young pre-college student who just finished a high school study and got admitted to both College of Medicine at Yonsei University in Seoul campus and Electrical and Computer engineering department at Seoul National University. Likewise, whenever I face the moment to decide between distinct options, now I know where I should put myself. In this regard, I would also like to acknowledge everything I learned and got from Berkeley. To me, Berkeley was the beautiful place with uncertainty but also with most resources and opportunities. Probably in many cases, our life will not go to the directions which we intended. If that is the case, I would like to be a person who will dive into the sea and just do my best for a

given hour and given day. Of course, I will get lost or frustrated, but they will eventually let me land at somewhere I deserve. Although the last one and half year of my Ph.D. was also not what I expected, as Professor Javey said, I am sure this will be also one of my interesting memory if I do my best and just forget regret.

Lastly, I would like to dedicate my dissertation to my family who gave me infinite supports, sincere love, and motivation during last 5 years. Although I was still not confident when I left Korea for my graduate study, I think now I am fully proud that I made it and I am glad I followed the encouragement from my parents to do Ph.D. in U.S. following the footsteps of my father. Although my life journey at Berkeley is probably about to be finalized, I am more excited to open the next chapter of our life. Needless to say, it has been the most amazing time for us so far and I am sure Yoonhee, Seowoo, and I will have even more fantastic journey together in the future.

1

Introduction

1.1 Transition-metal dichalcogenide monolayers for optoelectronic applications

Two-dimensional (2D) transition metal dichalcogenide (TMDC) monolayers such as MoS_2, WS_2, and WSe_2 have aroused significant attention among researchers over past years due to their unique properties which possess the promise for future optoelectronic applications. With their direct optical bandgaps in the range of near-infrared (NIR) to visible wavelengths, atomically thin TMDC monolayers exhibit the tunability of their properties through electric field and strain as well as the capability to achieve van der Waals heterostructures free of lattice mismatch. While these advantages enable their application for various optoelectronic devices including light-emitting diodes (LEDs) and photodetectors, there exist a number of obstacles to their implementation in practical applications. One of the main constraints is the low photoluminescence (PL) quantum yield (QY), a ratio of the number of photons a material emits to the number of photons a material absorbs, which is reported in the range of 0.01 to 6% at room temperature. PL QY is a key figure of merit in optoelectronic applications because it directly determines the maximum efficiency that the device can achieve. The low PL QY of TMDC monolayers at room temperature is associated with the dominance of nonradiative recombination processes, which is attributed to the interactions between excitons, trions, and free carriers. Therefore, the development of a simple and general method to achieve high PL QY in 2D TMDC monolayers, especially at high photocarrier densities where most optoelectronic devices operate, remains a key challenge for their potential applications in optoelectronic devices with high efficiency.

1.2 Infrared optoelectronics with black phosphorus

Room-temperature optoelectronic devices that are operating in infrared wavelength ranges can be used for numerous applications including optical communications, thermal imaging, health monitoring, spectroscopy, and gas sensing. Black phosphorus (bP) has recently gained great interest arising from its unique properties that are advantageous for developing optoelectronic devices such as LEDs and photodetectors. Specifically, owing to its direct bandgap even in a bulk form, bP has emerged as a potential alternative for optoelectronics whose operating wavelengths are in the mid-wavelength infrared (MWIR) and long-wavelength infrared (LWIR) range. BP can also be combined with other 2D layered materials to form heterostructures by van der Waals bonding, which allows for a new type of device architectures. Although the majority of commercially available MWIR and LWIR optoelectronic devices are based on narrow bandgap III-V and II-VI semiconductors, these materials require cryogenic cooling to reduce thermal noise during operation and have stringent requirements for epitaxial growth. With its self-terminated surfaces without dangling bonds, dramatic reduction of the active volume, and non-epitaxial membrane nature which readily enables the integration with other materials or various device structures, bP can thus overcome the key challenges of conventional infrared optoelectronics. Furthermore, next-generation high-performance infrared optoelectronic devices can be developed which benefit from bP's low Auger recombination velocity and wide bandgap tuning capability by strain at room temperature.

2

Monolayer Semiconductors with High Luminescence Efficiency

2.1 Introduction

Among various studies that have tried to improve the QY of TMDCs using different methods,[1-3] the chemical treatment by the nonoxidizing organic superacid, bis(trifluoromethane)sulfonamide (TFSI) has been suggested to dramatically enhance the PL QY of exfoliated MoS_2 monolayer to near 100% at low injection levels, achieving an optoelectronically-perfect TMDC monolayer despite high native defect density.[4] The superacid treatment induces counterdoping to reduce free carriers in electron-rich sulfur-based TMDCs, such as MoS_2 and WS_2, leading to entirely radiative recombination from neutral exictons. Despite its feasibility and effectiveness towards realization of TMDCs with perfect optoelectronic properties, the practical applications of superacid treatment for optoelectronic devices, however, have been restricted because of the poor yield of the treatment and its lack of stability. That is, although the treatment is carried out in ambient conditions, the significant improvement of PL QY by more than two orders of magnitude is observed in only few of treated samples and it appears to be nonuniform among the treated samples. Furthermore, the enhancement in PL QY is easily removed when exposed to harsh environments, because as-treated TMDC materials are vulnerable to water, low pressure, and organic solvents including acetone and isopropyl alcohol (IPA).

While chemical or electrical counterdoping significantly enhances the PL QY in sulfur-based TMDC monolayers by reducing free carriers, it is observed that selenide-based materials are largely unaffected by this method. Moreover, large-area growth of high quality TMDC monolayers

is essential in order to translate their unique properties into practical devices. In this regard, various growth techniques have been reported in literature, including sulfurization/selenization of oxide films,[5,6] chemical vapor deposition (CVD)[7-9] and metal organic chemical vapor deposition (MOCVD).[10] This research has now progressed to the growth of wafer-scale monolayer films.[11] Furthermore, direct synthesis of vertical and lateral heterostructures,[12,13] spatially controlled synthesis of full atomically thin circuitry,[14] and strain-engineered growth of 2D materials[15] have been demonstrated. However, the grown monolayers exhibit inferior optoelectronic performance compared to micromechanically exfoliated materials. Specifically, the PL QY of the grown films is often lower than their mechanically exfoliated counterparts.[16-20] This presents a major challenge for realization of high performance TMDC optoelectronics, where PL QY is the key figure of merit for determining the eventual device characteristics.[21,22]

Due to strong Coulomb interaction, photogenerated carriers in TMDC monolayers form excitons with binding energy over an order of magnitude larger than in conventional semiconductors.[23,24] These excitons can turn into positive or negative trions in the presence of background holes or electrons, respectively.[25] Energy transport in monolayer semiconductors occurs mainly by the diffusion of these tightly bound quasiparticles. Therefore, the operation of a wide array of optoelectronic devices such as light-emitting diodes,[22,26] solar cells[27] and excitonic switches[28] that utilize monolayer semiconductors is governed by exciton and trion diffusion. Understanding and manipulating the exciton diffusion in these monolayers can improve device performance and lead to the development of next-generation room-temperature excitonic technologies.

References

1 Tongay, S. *et al.* Broad-Range Modulation of Light Emission in Two-Dimensional Semiconductors by Molecular Physisorption Gating. *Nano Letters* **13**, 2831-2836 (2013).

2 Mouri, S., Miyauchi, Y. & Matsuda, K. Tunable Photoluminescence of Monolayer MoS2 via Chemical Doping. *Nano Letters* **13**, 5944-5948 (2013).

3 Peimyoo, N. *et al.* Chemically Driven Tunable Light Emission of Charged and Neutral Excitons in Monolayer WS2. *ACS Nano* **8**, 11320-11329 (2014).

4 Amani, M. *et al.* Near-unity photoluminescence quantum yield in MoS2. *Science* **350**, 1065 (2015).

5 Song, J.-G. *et al.* Controllable synthesis of molybdenum tungsten disulfide alloy for vertically composition-controlled multilayer. *Nature Communications* **6**, 7817 (2015).

6 Salitra, G., Hodes, G., Klein, E. & Tenne, R. Highly oriented WSe2 thin films prepared by selenization of evaporated WO3. *Thin Solid Films* **245**, 180-185 (1994).

7 Lee, Y.-H. *et al.* Synthesis of Large-Area MoS2 Atomic Layers with Chemical Vapor Deposition. *Advanced Materials* **24**, 2320-2325 (2012).

8 Huang, J.-K. *et al.* Large-Area Synthesis of Highly Crystalline WSe2 Monolayers and Device Applications. *ACS Nano* **8**, 923-930 (2014).

9 Liu, B. *et al.* Chemical Vapor Deposition Growth of Monolayer WSe2 with Tunable Device Characteristics and Growth Mechanism Study. *ACS Nano* **9**, 6119-6127 (2015).

10 Eichfeld, S. M. *et al.* Highly Scalable, Atomically Thin WSe2 Grown via Metal–Organic Chemical Vapor Deposition. *ACS Nano* **9**, 2080-2087 (2015).

11 Kang, K. *et al.* High-mobility three-atom-thick semiconducting films with wafer-scale homogeneity. *Nature* **520**, 656-660 (2015).

12 Li, M.-Y. *et al.* Epitaxial growth of a monolayer WSe2-MoS2 lateral p-n junction with an atomically sharp interface. *Science* **349**, 524 (2015).

13 Kang, K. *et al.* Layer-by-layer assembly of two-dimensional materials into wafer-scale heterostructures. *Nature* **550**, 229-233 (2017).

14 Zhao, M. *et al.* Large-scale chemical assembly of atomically thin transistors and circuits. *Nature Nanotechnology* **11**, 954-959 (2016).

15 Ahn, G. H. *et al.* Strain-engineered growth of two-dimensional materials. *Nature Communications* **8**, 608 (2017).

16 McCreary, A. *et al.* Distinct photoluminescence and Raman spectroscopy signatures for identifying highly crystalline WS2 monolayers produced by different growth methods. *Journal of Materials Research* **31** (2016).

17 Zhu, Y. *et al.* Strongly enhanced photoluminescence in nanostructured monolayer MoS2 by chemical vapor deposition. *Nanotechnology* **27**, 135706 (2016).

18 Kim, J. *et al.* Observation of ultralong valley lifetime in WSe2/MoS2 heterostructures. *Science Advances* **3**, e1700518 (2017).

19 Jin, C. *et al.* On Optical Dipole Moment and Radiative Recombination Lifetime of Excitons in WSe2. *Advanced Functional Materials* **27**, 1601741 (2017).

20 Choi, W. *et al.* Recent development of two-dimensional transition metal dichalcogenides and their applications. *Materials Today* **20**, 116-130 (2017).

21 Ye, Y. *et al.* Monolayer excitonic laser. *Nature Photonics* **9**, 733-737 (2015).
22 Lien, D.-H. *et al.* Large-area and bright pulsed electroluminescence in monolayer semiconductors. *Nature Communications* **9**, 1229 (2018).
23 Ramasubramaniam, A. Large excitonic effects in monolayers of molybdenum and tungsten dichalcogenides. *Physical Review B* **86**, 115409 (2012).
24 Zhu, B., Chen, X. & Cui, X. Exciton Binding Energy of Monolayer WS2. *Scientific Reports* **5**, 9218 (2015).
25 Ross, J. S. *et al.* Electrical control of neutral and charged excitons in a monolayer semiconductor. *Nature Communications* **4**, 1474 (2013).
26 Ross, J. S. *et al.* Electrically tunable excitonic light-emitting diodes based on monolayer WSe2 p–n junctions. *Nature Nanotechnology* **9**, 268-272 (2014).
27 Liu, Y. *et al.* Approaching the Schottky–Mott limit in van der Waals metal–semiconductor junctions. *Nature* **557**, 696-700 (2018).
28 Unuchek, D. *et al.* Room-temperature electrical control of exciton flux in a van der Waals heterostructure. *Nature* **560**, 340-344 (2018).

2.2 Highly stable near-unity photoluminescence yield in monolayer MoS_2*

While the achievement of counterdoping with superacid treatment on TMDCs is encouraging, the treatment does not persist during subsequent device fabrication and processing. For example, the enhancement in PL QY is easily removed after exposure to water and commonly used organic solvents including acetone. In this work, encapsulation of MoS_2 monolayers with CYTOP, which is an amorphous perfluorinated polymer with environmental stability and high optical transparency, is explored. This CYTOP-encapsulated TMDC monolayer is subsequently treated by TFSI, resulting in the near-unity PL QY with excellent stability under subsequent processing. We show that the dramatically improved optoelectronic properties of the TMDC monolayer can be directly attributed to the TFSI diffusion through the encapsulating layer which leads to effective counterdoping effect, suggesting that this technique can be employed generally for the development of monolayer optoelectronic devices with high efficiency.

Fig. 1a shows a schematic of the encapsulation/doping scheme. First, a MoS_2 monolayer is encapsulated by CYTOP deposited by spin-coating followed by thermal annealing. Next, the encapsulated MoS_2 is immersed in a TFSI solution (see methods for details). It should be noted that although the superacid treatment can also be applied to the other sulfur based TMDCs such as WS_2 as shown in Fig. S1, we focus on the process and characterization of exfoliated MoS_2 monolayers, for the scope of this paper. The PL QY measured at a laser power below the onset of biexitonic recombination is used as a figure of merit. The optimal CYTOP thickness for maximizing the PL QY was found to be 60-200 nm when the TFSI concentration of the solution is 0.2 mg/ml. As shown in the histogram in Fig. 1b, compared with the QY of untreated CYTOP-coated MoS_2 and the QY of as-exfoliated MoS_2 monolayers, the QY of CYTOP-coated MoS_2 monolayers after superacid treatment was consistently enhanced by over two orders of magnitude. Based on the optimized CYTOP and TFSI treatment for 20 samples, the QY of MoS_2 monolayers was within the range of 55% to near 100%.

Optical and PL images of pristine, untreated CYTOP-coated, and treated CYTOP-coated MoS_2 monolayer are shown in Fig. 1c-e. In addition to the uniform enhancement of PL emission in the CYTOP-coated MoS_2 monolayer after superacid treatment, these images show that there were no significant visible changes in the surface by encapsulation or superacid treatment. In addition, the surface morphologies of MoS_2 monolayer after encapsulation and superacid treatment were characterized by atomic force microscopy (AFM) and showed no visible changes, as shown in Fig.

* The following section was published in a similar form in ACS Nano. (H. Kim, D.-H. Lien, M. Amani, J. W. Ager, A. Javey, "Highly Stable Near-Unity Photoluminescence Yield in Monolayer MoS_2 by Fluoropolymer Encapsulation and Superacid Treatment", ACS Nano, 11 (5), 5179-5185, 2017)

S2.

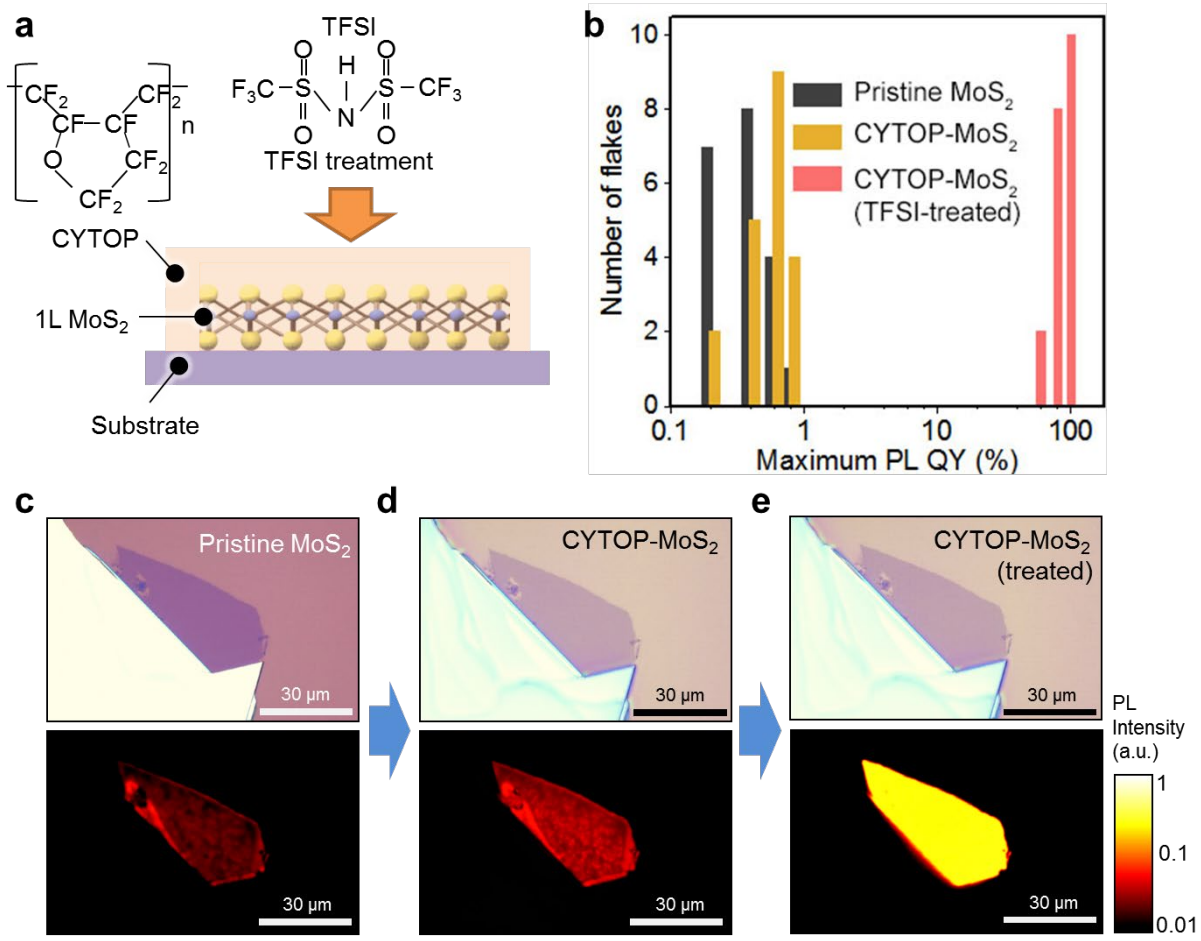

Fig. 1. a, Schematic of sample encapsulation/passivation scheme, showing a monolayer of MoS_2 coated by CYTOP and subsequently treated by TFSI. **b,** Histogram showing the PL quantum yield of 20 MoS_2 flakes measured at an incident laser power of 1×10^{-2} W cm^{-2} after exfoliation, coating by CYTOP, and treatment by TFSI. **c** to **e**, photoluminescence images and corresponding optical micrographs of a MoS_2 monolayer **c,** after exfoliation, **d,** coating by CYTOP, and **e,** treatment by TFSI; PL images are plotted on a common logarithmic scale.

We performed detailed steady-state and transient PL measurements to characterize the optoelectronic properties of MoS_2 before and after treatment. PL spectra of MoS_2 monolayers measured at an incident power of 2 W cm^{-2} are shown in Fig. 2a and indicate that the PL intensity was enhanced by over two orders of magnitude after superacid treatment. Furthermore, as shown

in the inset of Fig. 2a, we do not detect a measureable peak shift after both CYTOP encapsulation and TFSI treatment, with the only significant spectral change being the reduction in the low-energy tail after treatment. Additionally, using the quantitative absorption measurements with two different methods as described in previous studies,[1,2] we observed that CYTOP coating and the superacid treatment do not have significant effects on the light absorption in the range of 1.6 to 2.6 eV, as shown in Fig. 2b. The pump-power behavior of the PL QY in MoS_2 monolayers was measured over dynamic range of six orders of magnitude as shown in Fig. 2c. The PL QY of CYTOP-encapsulated MoS_2 monolayer after superacid treatment approaches 100% at a low pump intensity ($< 5 \times 10^{-2}$ W cm^{-2}). We found that the encapsulation of MoS_2 with CYTOP affects the biexcitonic recombination rate which can most likely be attributed to the change of the dielectric surroundings from air/MoS_2/substrate to CYTOP/MoS_2/substrate where CYTOP has a refractive index of 1.34. Biexcitonic recombination rate is expected to vary with encapsulation layers because the exciton-exciton interaction is strongly coupled with dielectric environments due to screening effects.

The impact of superacid treatment on the CYTOP-encapsulated MoS_2 monolayers was further evaluated *via* the carrier recombination dynamics measured from time-resolved PL measurements. Multiple decay spectra were also measured at various initial exciton concentrations as shown in Fig. S3. The resulting spectra were then combined to form a single decay curve with over five orders of magnitude of dynamic range. The radiative lifetime (τ_r) of the treated CYTOP-encapsulated MoS_2 was measured to be 15 ns, which is similar to what has been reported in our previous work without CYTOP.[1,2]

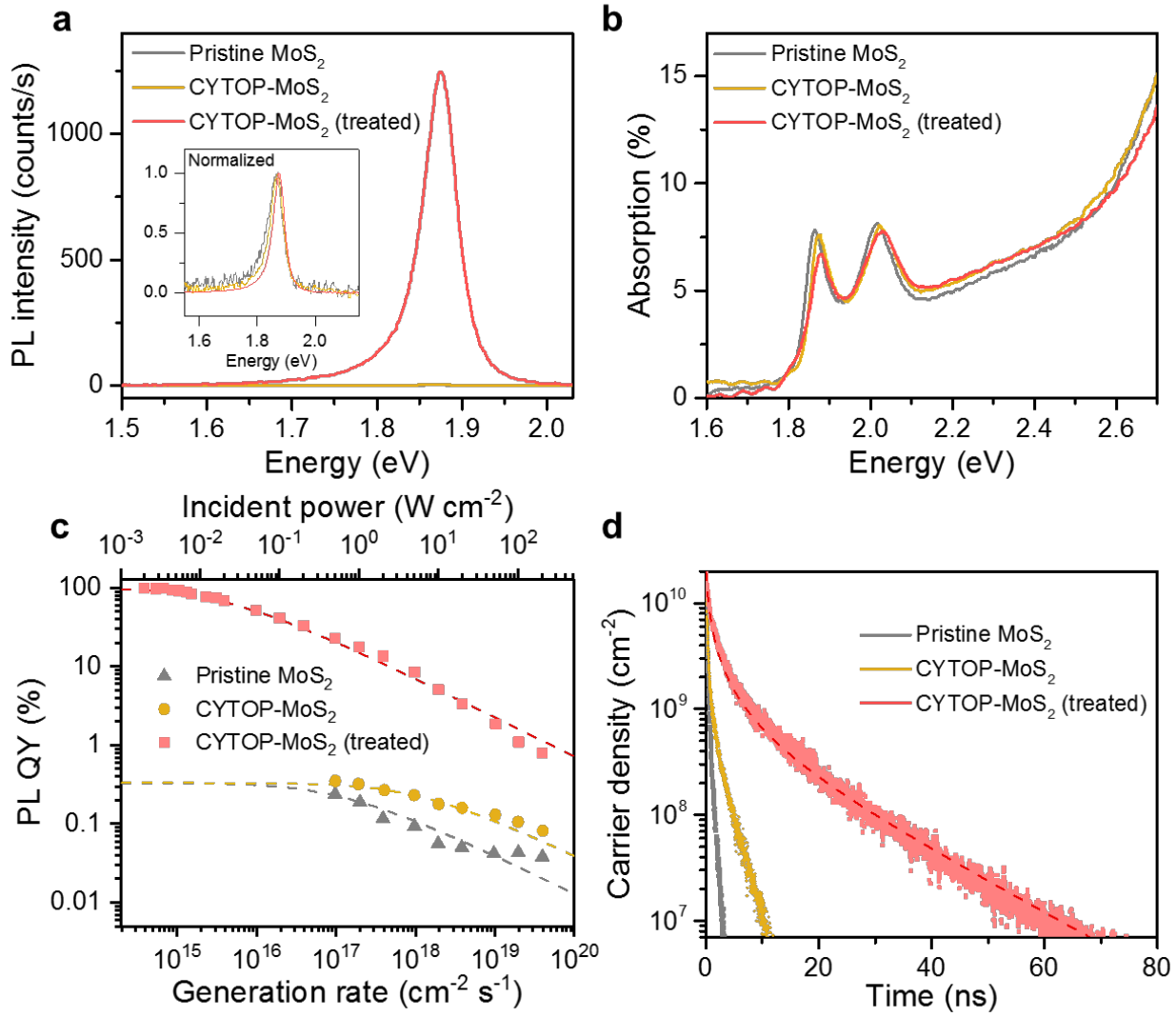

Fig. 2. a, Photoluminescence spectra measured at an incident power of 2 W cm^{-2} for an as-exfoliated MoS_2 monolayer, after coating by CYTOP, and after treatment by TFSI; inset shows normalized spectra. **b,** Absorption spectra measured for an as-exfoliated MoS_2 monolayer, after coating by CYTOP, and after treatment by TFSI. **c,** PL QY as a function of incident laser power measured on an as-exfoliated MoS_2 monolayer, after coating by CYTOP, and after treatment by TFSI. **d,** Time-resolved photoluminescence decay measured on an as-exfoliated MoS_2 monolayer, after coating by CYTOP, and after treatment by TFSI.

To investigate the mechanism of TFSI passivation of CYTOP-encapsulated MoS_2, QY was measured at a low pump intensity ($\sim 3 \times 10^{-3}$ W cm^{-2}) as a function of treatment time and CYTOP thickness, as shown in Fig. 3a. Both the increase in QY with TFSI exposure time and with

decreasing CYTOP thickness suggest a diffusional mechanism. We constructed a simple model for the process as follows. First, based on other studies which discussed the diffusion kinetics regarding TFSI or polymer film,[3-7] the diffusion of TFSI through CYTOP satisfies the criterion of Fickian diffusion. It is assumed that the swelling effect of the CYTOP film by the solvent is negligible, allowing the concentration of TFSI $c(x,t)$ to be described as

$$\frac{c(x,t) - c(x,0)}{c_s - c(x,0)} = 1 - \mathrm{erf}\left(\frac{x}{2\sqrt{Dt}}\right) \tag{4}$$

where x is the distance from the interface between the bulk solution and the surface of the CYTOP, t is diffusion time, D is the TFSI diffusion coefficient in CYTOP, and c_S is the TFSI concentration at the interface between the bulk solution and the surface of the CYTOP ($x = 0$). We used Fourier transform infrared (FTIR) spectroscopy to measure the TFSI diffusion into the CYTOP. Here, the samples were rinsed with 1,2-dichloroethane (DCE)/1,2-dichlorobenzene (DCB), which were solvents for TFSI solution, to remove residual TFSI molecules from the top surface. As shown in Fig. 3b, absorption peaks associated with TFSI were observed after treatment, and increased with increasing treatment time. While CYTOP contains a significant number of C-F bonds, the S-N-S and S=O peaks can directly be attributed to the diffused TFSI. As such, the enhanced peak intensities can be used to measure the concentration of diffused TFSI within the CYTOP layer. Fig. 3c shows the time-dependent absorption A_t at 1325 ± 25 and 1140 ± 25 cm^{-1} for a 100 nm CYTOP layer normalized to the steady state values, A_{eq}, measured after 40 minutes of exposure. The diffusion coefficient measured from FTIR spectroscopy is 1.1 × 10^{-14} cm^2 s^{-1} and the dotted line is a fit to $c(x,t)$ integrated from 0 to L, which is described as[3,8]

$$\frac{A_t}{A_{eq}} = 1 - \frac{8}{\pi^2}\sum_{m=0}^{\infty}\frac{1}{(2m+1)^2}\exp\left(\frac{-D(2m+1)^2\pi^2 t}{L^2}\right) \tag{5}$$

This increase of QY over treatment time can be explained through diffusion of TFSI into the CYTOP layer.

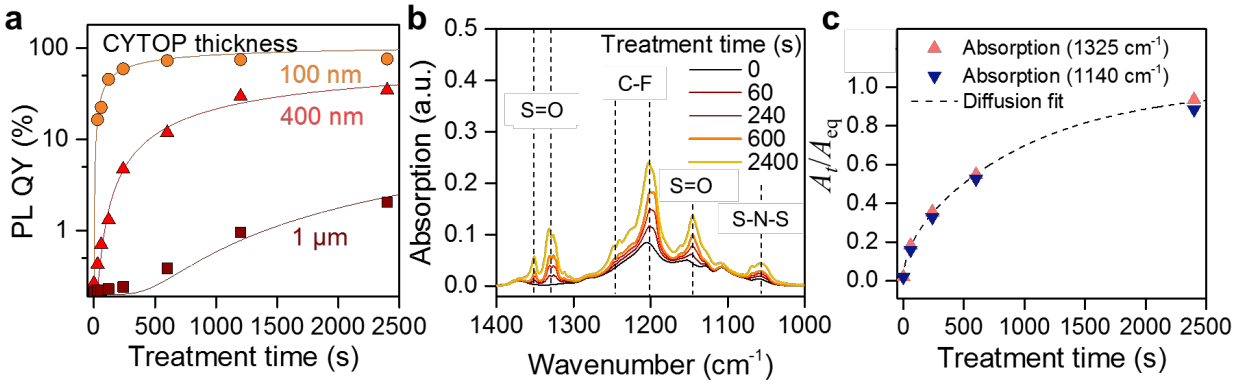

Fig. 3. a, PL QY as a function of treatment time for MoS_2 samples coated by 100 nm, 400 nm, and

1 μm thick CYTOP films. **b,** Absorption spectra measured on a 100 nm CYTOP film coated on a KBr substrate as a function of TFSI treatment time. **c,** IR absorption near 1325 and 1140 cm^{-1} of the TFSI diffused through 100 nm CYTOP film coated on a KBr substrate as a function of the TFSI treatment time. A_t and A_{eq} denote the absorption at time t and at equilibrium. Line is a fit to Eq 5 with a TFSI diffusion coefficient of 1.1×10^{-14} cm^2 s^{-1}.

We found that CYTOP-encapsulation not only promotes a high yield and control of PL QY enhancement during treatment, but also preserves the near-unity PL QY against external conditions. Fig. 4a and b illustrate the stability of CYTOP-encapsulated MoS_2 monolayers after TFSI treatment, compared to treated samples without encapsulation. For TFSI treated MoS_2 without encapsulation, the PL QY is significantly degraded after processing with each solvent for 15 seconds or when the sample is exposed to low pressure (~10^{-5} Torr). Due to the high chemical resistance and hydrophobicity of CYTOP, we find that it is also able to act as a protective capping layer.[9-12] For vacuum measurement, to minimize the release of diffused TFSI by degassing of the fluoropolymer at low pressure, a secondary, thicker CYTOP (~ 2 um) layer was additionally spin-coated after CYTOP encapsulation and subsequent TFSI treatment. Also, for the vacuum-processed sample, the Raman spectrum of CYTOP-encapsulated MoS_2 monolayer after treatment was measured to ensure that there is negligible strain, which may be caused by the volume change of CYTOP under vacuum condition (Fig. S4). The PL QY of CYTOP-encapsulated WS_2 monolayer is also stable against post-rinsing processing and the various external conditions.

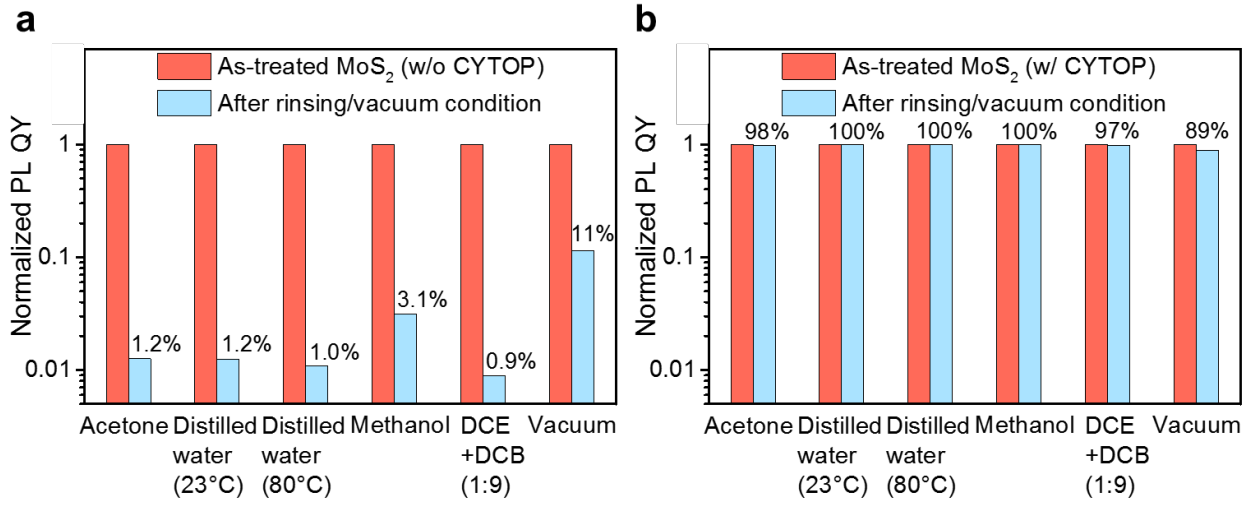

Fig. 4. a, PL QY of TFSI treated MoS_2 samples (not coated by CYTOP) after various processing **b,** PL QY of TFSI treated MoS_2 samples (coated by 100 nm of CYTOP) after various processing. Solvent exposure was conducted by immersing the sample in each solvent for 15 seconds. For vacuum conditions, MoS_2 sample was coated by 2 μm of secondary CYTOP layer after 100 nm of

CYTOP and subsequent TFSI treatment.

Finally, we demonstrate that CYTOP encapsulant can be patterned, which provides a potential route towards the fabrication of practical devices. We develop a patterning method that consists of photolithography and lift-off of CYTOP. Fig. 5 shows the PL images and corresponding optical micrographs of a MoS_2 monolayer with CYTOP patterns which were examined after treatment and after subsequent rinsing in water. After treatment, both exposed and CYTOP encapsulated portions of the monolayer showed high and uniform PL QY. When the treated MoS_2 monolayer with CYTOP patterns was rinsed with water, significant degradation of the PL in the un-encapsulated regions was observed. However, as shown in Fig. 5f, the part of the MoS_2 monolayer with CYTOP encapsulation retained high PL QY. This result indicates that our encapsulating layer, which is compatible with a general patterning process, can be stable during subsequent fabrication process and be suitable for future device applications, preserving dramatically enhanced PL QY against external conditions.

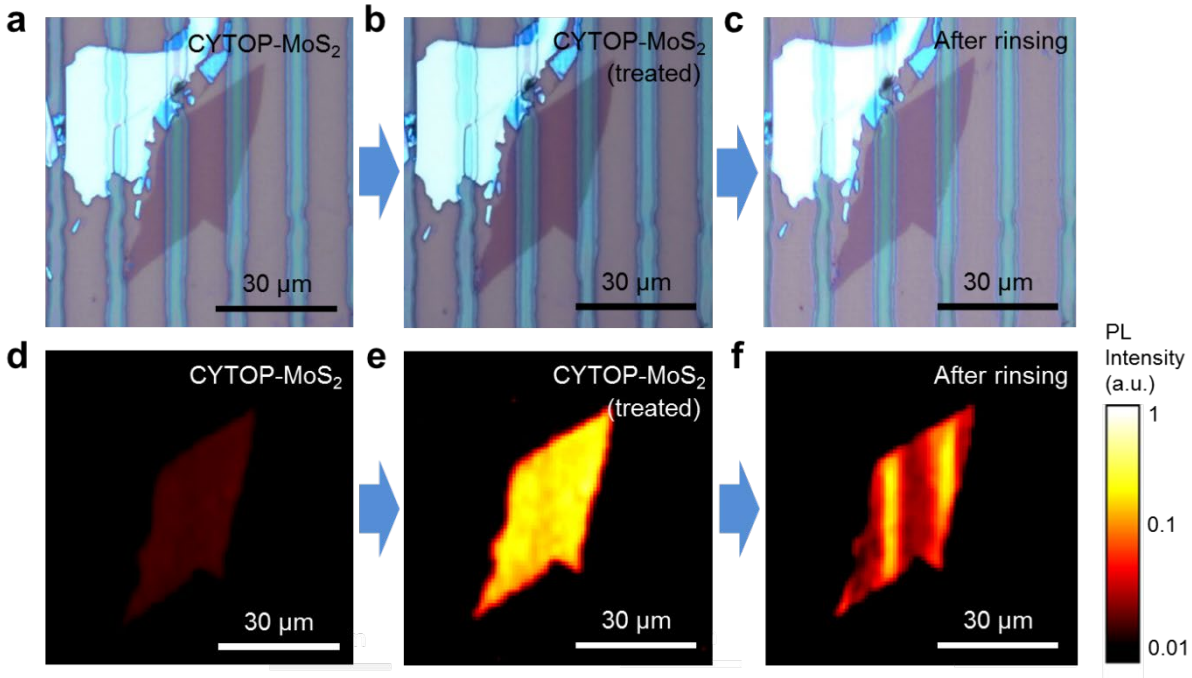

Fig. 5. a to **c** Optical micrographs, and **d** to **f** corresponding photoluminescence images of an as-prepared CYTOP-patterned MoS_2 monolayer, after treatment by TFSI, and after rinsing with water for 15 seconds; PL images are plotted on a common logarithmic scale.

In conclusion, we have demonstrated 2D TMDCs with near-unity PL QY and excellent stability through superacid treatment after encapsulation by an environment-resistive fluoropolymer. Based on the diffusion mechanism, TFSI is able to penetrate through CYTOP encapsulant and suppresses non-radiative recombination in the monolayer, resulting in near-unity PL QY in both MoS_2 and WS_2 at low injection levels. Due to its ability to be directly patterned and its compatibility with general fabrication processes, this method can potentially be utilized for the fabrication of high performance 2D optoelectronic devices.

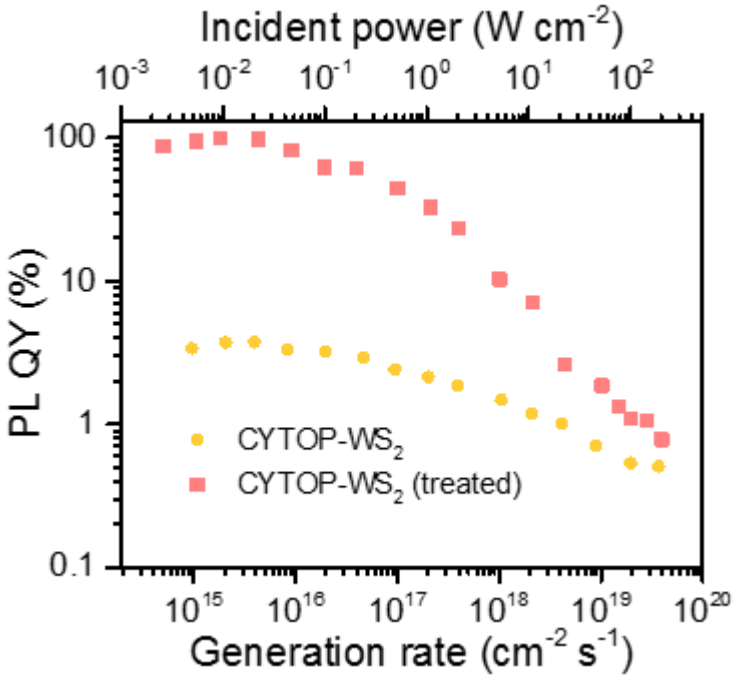

Fig. S1. Pump-power dependence of the PL QY for an as-exfoliated and chemically treated CYTOP-WS_2 monolayer.

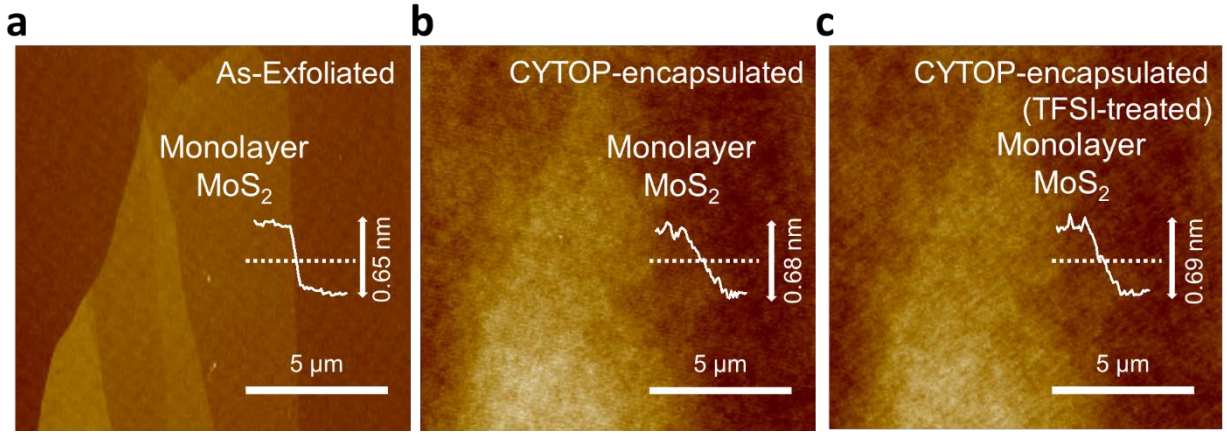

Fig. S2. AFM images of **a,** an as-exfoliated, **b,** CYTOP-encapsulated, and **c,** TFSI-treated CYTOP-encapsulated MoS_2 monolayer.

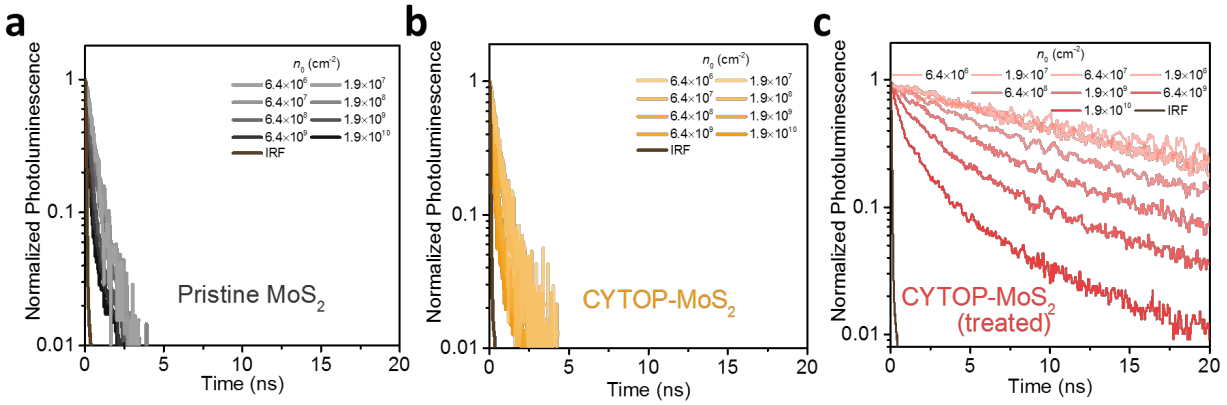

Fig. S3. Radiative decay spectra of **a,** a pristine, **b,** CYTOP-encapsulated, and **c,** TFSI-treated CYTOP-encapsulated MoS_2 monolayer measured at different pump fluences.

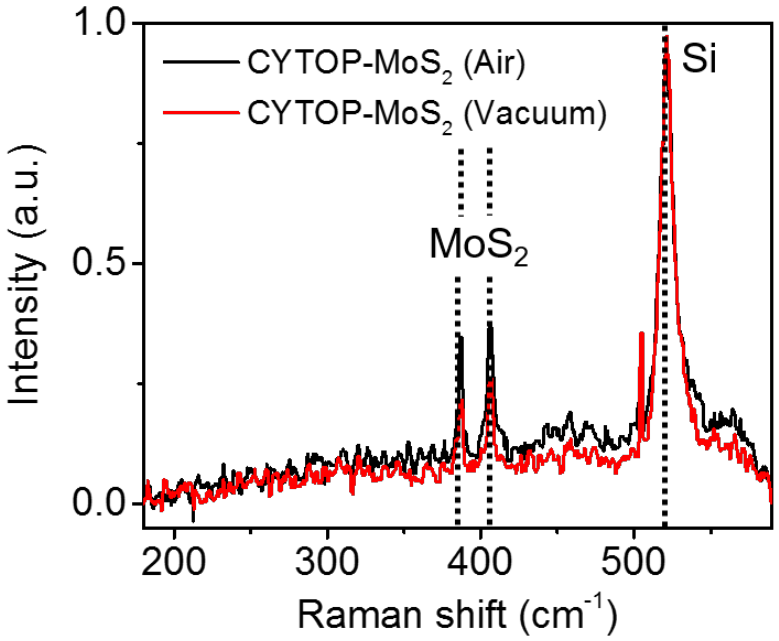

Fig. S4. Raman spectrum of a CYTOP-encapsulated MoS_2 monolayer measured under normal pressure and the vacuum condition.

Experimental and theoretical details

Sample Preparation and Encapsulation

Quartz was used as the substrate for all calibrated optical measurements. The substrates were cleaned in a piranha solution for 15 min and subsequently rinsed with acetone, isopropyl alcohol (IPA), and deionized (DI) water for 5 min. MoS_2 was mechanically exfoliated on quartz substrate from bulk crystals (SPI). Prior to spin-coating, samples were annealed in forming gas (5% H_2, 95% N_2) at 300ºC for 3 hours. In order to obtain 100 nm thick CYTOP film, a CYTOP solution (CTL-809M, Asahi Glass Co.) was diluted in its solvent (CT-Solv.180, Asahi Glass Co.) to make a 3 wt % CYTOP solution and spin-coated at 500 rpm for 10 s, then at 4000 rpm for 30 s, followed by thermal annealing in a N_2 ambient, where the temperature was gradually increased from 30 to 200ºC over a span of 50 min.

Chemical Treatment

A procedure for superacid treatment used in this work was similar to the method described in the previous studies,[1,2] but with further optimization. Prior to solution preparation, all chemical bottles were first opened inside a N_2 atmosphere. 20 mg of TFSI (Sigma-Aldrich) was dissolved in 10 ml of 1,2-dichloroethane (DCE) (Sigma-Aldrich) to make a 2 mg/ml TFSI solution and further diluted with 1,2-dichlorobenzene (DCB) (Sigma-Aldrich) to make a 0.2 mg/ml TFSI solution in a 1:9 mixture of DCE and DCB. For treatment, samples and solution were taken out from the glovebox and then samples were immersed in the 0.2 mg/ml TFSI solution for 40 min under ambient air condition at room temperature. After the samples were removed from the solution, they were blow-dried with nitrogen without rinsing or annealing.

Optical Spectroscopy

The instruments and procedures used for calibrated steady-state and transient optical characterization utilized here were same as our previous study.[1] In brief, the 514.5 nm line of Ar^+ laser (Lexel 95) was used for excitation in steady-state PL and Raman measurements, and the power density was adjusted by neutral density filters. The power of incident laser beam was continuously monitored by a photodiode power meter (ThorLabs S120C); in order to accurately measure low laser powers, the power on the laser diode was approximately 100× higher than the power incident on the sample. A CCD detector (Andor iDus BEX2-DD) on a f = 340 mm spectrometer with a 150 g/mm grating was used for steady state measurements. The CCD background was measured prior to the PL measurement and subtracted from the PL acquisition. The external sample PL efficiency was determined using the wavelength dependent response and the collection efficiency of the instrument, which were estimated using previously described methods after the measurement. The absolute internal PL QY was extracted using the quantitative absorption data. Time resolved measurements were performed using a 514 nm line selected from a supercontinuum laser (Fianium WhiteLase SC-400) using a double monochromator, and subsequently detected using a single photon counting avalanche photodiode (IDQuantique) and analyzed using a time-correlated single photon counting module (Becker-Hickl GmbH). Raman measurements were measured in the backscattering geometry and using a triple spectrometer configured in subtractive mode with a 2400 g/mm grating in the final stage. For all measurements, the laser was focused on the sample using a 50× objective lens with a numerical aperture of 0.55. Photoluminescence images were acquired on MoS_2 monolayers prepared by gold-exfoliation[13] using a florescence microscopy setup and a 470 nm LED as the excitation source. IR absorption measurements were performed using an FTIR microscope (Nicolet, ThermoFisher). Prior to IR absorption measurements, the samples were rinsed with DCE/DCB to remove residual TFSI molecules on the sample surface.

Stability Characterization

Stability tests were performed on TFSI treated MoS_2 samples with and without CYTOP encapsulation. After PL QY measurement for as-treated samples, each sample was immersed in acetone, distilled water (80ºC), methanol, and DCE/DCB (1:9 in weight ratio) for 15 seconds, respectively. When the samples were removed from solvents, they were blow-dried with nitrogen and the QY was measured using the same procedure as was performed for as-treated samples. For

vacuum measurement, after CYTOP encapsulation and subsequent TFSI treatment, a secondary, thicker CYTOP (~ 2 um) layer was additionally spin-coated and annealed at 80ºC for 30 min in a N_2 ambient. PL QY measurements in the vacuum chamber were performed at a pressure < 10^{-5} Torr.

Patterning process

MoS_2 monolayers were prepared on a cleaned 260 nm SiO_2/Si substrate and spin-coated with a positive photoresist (S1818, Shipley) at 500 rpm for 5 s and then at 3000 rpm for 30 s, followed by baking at 115ºC for 60 s on a hotplate. After UV exposure at a constant intensity of 100 mJ/cm^2, the sample was developed with MF-26A (Microchem) for 1 min, rinsed with DI water, and blow-dried with nitrogen. A 3 wt % CYTOP solution was then spin-coated at 500 rpm for 10 s / 4000 rpm for 30 s. The sample was heated on a hotplate at 80ºC for 2 min. To remove the photoresist and the CYTOP layer on the remaining photoresist, the lift-off was carried out by immersing the sample in warm acetone for 1 h. Finally, the sample was thermally annealed to post-bake the CYTOP patterns using the same procedure described as above.

References

1 Amani, M. *et al.* Near-unity photoluminescence quantum yield in MoS2. *Science* **350**, 1065 (2015).

2 Amani, M. *et al.* Recombination Kinetics and Effects of Superacid Treatment in Sulfur- and Selenium-Based Transition Metal Dichalcogenides. *Nano Letters* **16**, 2786-2791 (2016).

3 Alfrey Jr, T., Gurnee, E. F. & Lloyd, W. G. Diffusion in glassy polymers. *Journal of Polymer Science Part C: Polymer Symposia* **12**, 249-261 (1966).

4 Crank, J. *The mathematics of diffusion*. (Oxford university press, 1979).

5 Masaro, L. & Zhu, X. X. Physical models of diffusion for polymer solutions, gels and solids. *Progress in Polymer Science* **24**, 731-775 (1999).

6 Bowyer, W. J., Xu, W. & Demas, J. N. Determining Proton Diffusion in Polymer Films by Lifetimes of Luminescent Complexes Measured in the Frequency Domain. *Analytical Chemistry* **81**, 378-384 (2009).

7 Wapner, K. & Grundmeier, G. Spatially resolved measurements of the diffusion of water in a model adhesive/silicon lap joint using FTIR-transmission-microscopy. *International Journal of Adhesion and Adhesives* **24**, 193-200 (2004).

8 Musto, P., Galizia, M., La Manna, P., Pannico, M. & Mensitieri, G. Diffusion and molecular interactions in a methanol/polyimide system probed by coupling time-resolved FTIR spectroscopy with gravimetric measurements. *Frontiers in Chemistry* **2** (2014).

9 Kalb, W. L., Mathis, T., Haas, S., Stassen, A. F. & Batlogg, B. Organic small molecule field-effect transistors with Cytop gate dielectric: Eliminating gate bias stress effects. *Applied Physics Letters* **90**, 092104 (2007).

10 Walser, M. P., Kalb, W. L., Mathis, T., Brenner, T. J. & Batlogg, B. Stable complementary inverters with organic field-effect transistors on Cytop fluoropolymer gate dielectric. *Applied Physics Letters* **94**, 053303 (2009).

11 Cheng, X. *et al.* Air Stable Cross-Linked Cytop Ultrathin Gate Dielectric for High Yield Low-Voltage Top-Gate Organic Field-Effect Transistors. *Chemistry of Materials* **22**, 1559-1566 (2010).

12 Choi, S., Jang, J., Kim, J. & Han, M. Low-Temperature Organic (CYTOP) Passivation for Improvement of Electric Characteristics and Reliability in IGZO TFTs. *IEEE Electron Device Letters* **33**, 381-383 (2012).

13 Desai, S. B. *et al.* Gold-Mediated Exfoliation of Ultralarge Optoelectronically-Perfect Monolayers. *Advanced Materials* **28**, 4053-4058 (2016).

2.3 Synthetic WSe_2 monolayers with high photoluminescence quantum yield*

WSe_2 monolayers grown *via* CVD possess strong interactions with the substrate. We and others have utilized this effect for controlled strain engineering of the grown monolayers based on the thermal coefficient of expansion mismatch between the substrate and monolayer.[1,2] The substrate coupling and the strain can be released by utilizing poly(methyl methacrylate) (PMMA) mediated transfer of the monolayer onto a secondary substrate. However, this process often requires harsh environments, *i.e.* hydrofluoric acid, potassium hydroxide or the use of sonication to detach the monolayer from the substrate. Complete removal of the polymer used for transfer is also challenging and often requires subsequent thermal annealing of the sample.

As a less damaging alternative, we developed the SEMD process to decouple grown monolayers from the substrate (Fig. 1a). The process is very simple and begins by placing a droplet of solvent with high vapor pressure (e.g., acetone) on an as-grown WSe_2 monolayer. As the solvent evaporates, the surface-tension pulls on the grown material and decouples the material from the substrate. A balance of forces allows the process to decouple the monolayer.

The effect of SEMD was characterized by PL spectroscopy. We find that the emission peak blue shifts by ~80 meV from 1.57 eV for the as-grown sample to 1.65 eV after SEMD (Fig. 1B). The post-SEMD emission peak position closely matches that of unstrained CVD WSe_2 monolayers and that of micromechanically exfoliated samples,[3,4] indicating the full release of the built-in strain and, thus, complete decoupling of the synthetic monolayer from the substrate. Critically, the substrate-decoupled WSe_2 monolayers exhibit more than an order of magnitude brighter PL emission intensity compared with substrate-coupled as-grown monolayers before SEMD. To further investigate the SEMD mechanism, we performed in situ PL imaging as the solvent evaporates (Fig. 1, C to G, and Fig. S1). Imaging was performed using a bandpass filter centered at 1.65 eV, which blocks the emission of the substrate-coupled as-grown sample under biaxial tensile strain. Before and immediately after dispensing of the solvent, we observed no strong emission, as can be seen in Fig. 1 (C and D). In addition, in situ PL spectra measurement in acetone baths (Fig. S2) shows no change in PL intensity or spectra unlike the changes observed in Fig. 1B. This suggests that the presence of the solvent by itself does not influence the built-in substrate coupling in as-grown samples. However, at the onset of solvent evaporation from the monolayer, we start to observe strong emission at 1.65 eV at the edge of the crystal (Fig. 1E). Once the solvent

* The following section was published in a similar form in Science Advances. (H. Kim, G. H. Ahn, J. Cho, M. Amani, J. P. Mastandrea, C. K. Groschner, D.-H. Lien, Y. Zhao, J. W. Ager III, M. C. Scott, D. C. Chrzan, A. Javey, "Synthetic WSe_2 Monolayers with High Photoluminescence Quantum Yield", Science Advances, 5, eaau4728, 2019)

is fully evaporated (Fig. 1F), the emission becomes uniform over the full sample domain (Fig. 1G). As plotted in Fig. 1 (C to G) and Fig. S1, the PL intensity profile across the WSe_2 monolayer shows that the PL intensity at 1.65 eV starts to increase from the edge and becomes uniformly enhanced over the SEMD process. This indicates that the substrate decoupling is mediated by the solvent evaporation and is initiated from the edges of the monolayer. Subsequently, the emission remains stable over time. It is worth noting that the SEMD process is also applicable to other growth substrates, including sapphire (Fig. S3). For this work, we primarily focused on using acetone as the solvent, given its high vapor pressure and minimal effects to the grown material quality (30). Other solvents with varying vapor pressures were also investigated and show similar decoupling results (Fig. S4).

We used transmission electron microscopy (TEM) electron diffraction to directly measure the lattice constant of the grown WSe_2 before and after SEMD to verify the release of biaxial tensile strain of the as-grown films. WSe_2 monolayers were prepared via direct growth on SiO_2 membranes, and the SEMD process was performed on these samples. Fig. 1H shows the overlay of diffraction spots for the as-grown and substrate-decoupled WSe_2 monolayers. We calculated the diffraction spots as the center of mass of individual diffraction spots from the measurements shown in Fig. S5. All the electron diffraction measurements for as-grown WSe_2 were taken with the identical lens settings, so as not to alter the calibration of the camera length and the lens aberrations. A polycrystalline Cu standard was used for the calibration. From the electron diffraction measurements and the subsequent comparison of lattice constants from each of the diffraction patterns, we find that ~1.54 ± 0.05% tensile strain was released from the as-grown WSe_2 monolayer after SEMD. The strain value in the as-grown films is consistent with our previous study using similar growth conditions. Note that the diffraction pattern of an as-exfoliated WSe_2 monolayer is also shown in Fig. S5. Here, the calculated lattice constant value from the exfoliated sample matches that of substrate-decoupled WSe_2, verifying the complete release of built-in strain after the SEMD process.

While the development of a detailed understanding of the process awaits further study, we propose the following model as a guide to understand the experimental results. First, assume that the experimentally observed intrinsic biaxial tensile strain from growth is stabilized by the friction-induced resistance to sliding of the monolayer on the substrate. There might be, of course, local pinning sites that more strongly couple the film and substrate, and these would change the details of the strain relief process, but friction will still play a role. Typically, one expects that the friction force is proportional to the contact force between the film and substrate and that a reduced contact force would allow for the relaxation of the strain present in the as-grown monolayer. The geometry of a free-standing thin film with a droplet placed on it has been the subject of some studies.[5-8] In the mechanism considered here, the interaction of the film with the substrate and the imposed biaxial strain in the film must be considered. Figure 1I illustrates the structure of the droplet as it evaporates, and it shows forces acting on the system near the triple point (junction of liquid, air, and WSe_2). For the process, the interfacial energy of the liquid/air junction ($\gamma_{liq/air}$), the interfacial

energy of the liquid/WSe_2 ($\gamma_{liq/WSe2}$), the stress in the WSe_2 monolayer itself (γ_{WSe2}), and the attractive force between the substrate and the WSe_2 are considered. The resulting forces can be balanced only if the monolayer is slightly raised from the substrate at the triple point, as shown in Fig. 1I, and it is hypothesized that this reduces the contact force between the film and the substrate. This reduction in friction would enable the local strain relief of the monolayer, as the distortion of the film is expected to be localized to the region of the triple point. It is expected that once the triple point has passed a region, the film re-adheres to the substrate. Therefore, for larger films, one pass of the triple point may be insufficient to completely relax the strain, and multiple passes may be required.

We also investigated the effect of solvent evaporation on exfoliated WSe_2 monolayer samples, which are mechanically relaxed as processed. As shown in Fig. S6, we used different WSe_2 crystals from three different vendors and found that the process has no significant effect on the exfoliated monolayers. Specifically, we observed minimal change in the emission intensity and peak position. The substrate-decoupled monolayers are also stable after acetone evaporation. As shown in Fig. S7, the PL characteristic is stable after rinsing with various solvents, under vacuum, and over time in a humid condition. The results show that acetone does not chemically modify the monolayers and does not by itself affect the recombination processes. Instead, acetone evaporation induces surface tension–mediated decoupling of the monolayer.

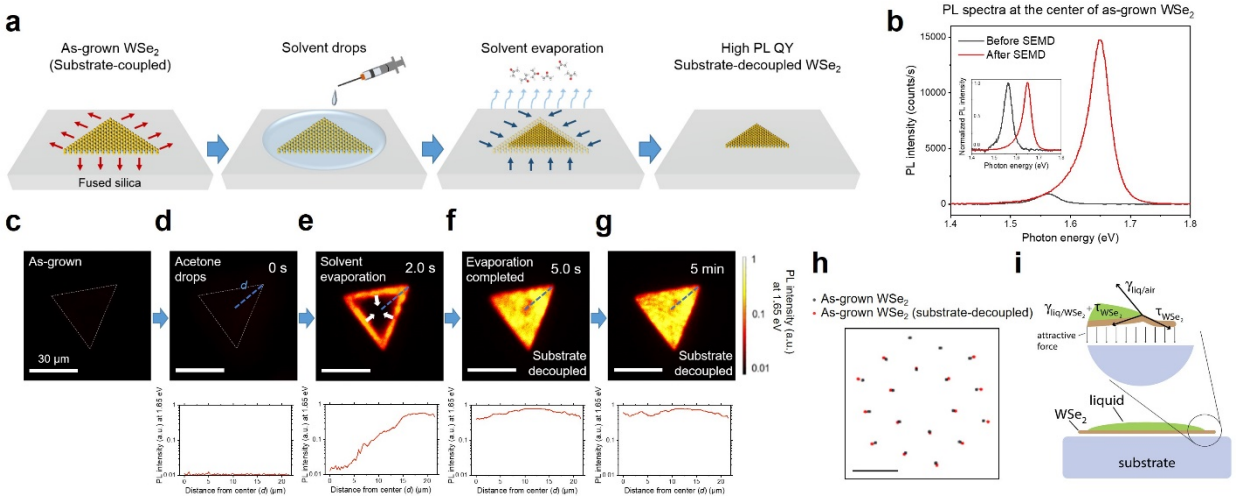

Fig. 1. a, Schematic of SEMD process. An as-grown WSe_2 monolayer is immersed in a droplet of solvent. During the solvent evaporation, the substrate decoupling process of the WSe_2 monolayer is accomplished with the enhanced PL QY. **b,** Schematic describing the factors influencing the SEMD process of WSe_2 monolayer. **c,** Overlay of diffraction spots for as-grown and substrate-decoupled samples; 1.54 ± 0.05% tensile strain in the as-grown sample is released after the SEMD process. The scale bar is 5 nm^{-1}. Original diffraction patterns of the samples are shown in Fig. S2. **d,** PL spectra measured at the center of as-grown WSe_2 monolayer with an excitation power of 15

W cm^{-2} prior to and after the SEMD process; inset shows normalized spectra. **e-i,** *In-situ* PL imaging of the SEMD process in a WSe_2 monolayer. The scale bar is 30 μm for all PL images. Note that the images were taken using a 1.65 eV bandpass filter which blocks the emission from the as-grown monolayer and plotted on a logarithmic scale. PL images at additional timestamps are shown in Fig. S3.

In parallel, optimized growth conditions are important for obtaining high PL QY. We find the role of the growth-promotor particularly critical. In our case, a halide based promotor was found to be essential to obtain WSe_2 with grain sizes on the order of 100 μm as well as continuous films. Previous studies have shown that halide based salts result in formation of volatile tungsten-based halide species due to chemical reaction between the tungsten oxide precursor and the alkali metal halides.[9,10] The role of the halide promotor (KBr for this work) on the PL QY of the monolayer films is highlighted in Fig. 2a by varying the KBr to WO_3 precursor weight ratio. For the explored range, no significant effect is observed on the PL QY as a function of KBr content for as-grown monolayers. By decoupling the monolayers, the intrinsic properties of the material can be assessed, following which, the strong effect of KBr weight ratio on the PL QY is observed (Fig. 2a). We find that in the case of higher promotor weight ratio (2:1; KBr:WO_3), the overall average PL QY after SEMD is one order of magnitude lower than samples grown with lower KBr amount (1:2; KBr:WO_3), while there was no WSe_2 growth if the promoter weight ratio was further reduced to 1:4; KBr:WO_3. Subsequently, all characterization is performed on samples prepared with 1:2; KBr:WO_3.

Fig. 2 (b and c) depict the histograms of the low-pump (2 W cm^{-2}) PL QY and the emission peak position, respectively for exfoliated WSe_2 monolayers and WSe_2 monolayers grown using optimized growth condition, before and after SEMD. No statistically significant difference is observed for the emission peak position of the monolayer after SEMD and exfoliated WSe_2 monolayers. On the other hand, the as-grown samples consistently show a ~80 meV red-shift due to tensile strain, which is consistent with the previous report.[11] The PL QY of as-grown WSe_2 (1.4%) is slightly lower than that of exfoliated samples (3.1%). The grown monolayers after SEMD on the other hand show average PL QY of 31.2%, with the highest observed value of 60%. This represents the highest PL QY reported in WSe_2 prepared by any method.

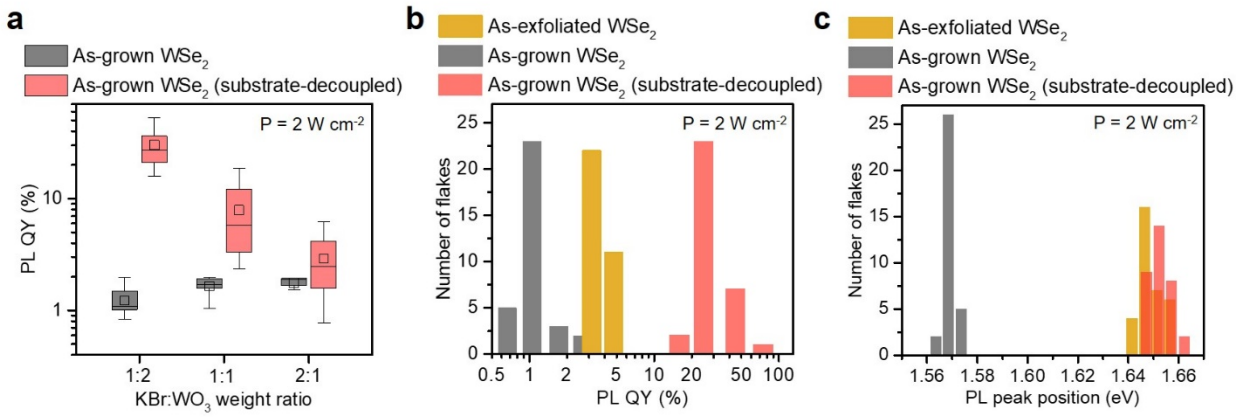

Fig. 2. a, Box and whisker plot showing the PL QY of synthetic WSe_2 grown using varying promotor weight ratios both before and after the SEMD process. Error bars indicate standard deviation of PL QY obtained from 10 different locations on the samples from the same growth. Histogram showing the **b,** PL QY and **c,** PL peak position of as-grown WSe_2 monolayers before and after the SEMD process as well as exfoliated WSe_2 monolayers. PL QY of as-exfoliated samples prepared from bulk crystals provided by three different vendors are shown in Fig. S6.

The reduction in PL when the sample is strongly coupled to the substrate may be attributed to a number of factors. As shown in Fig. 1c, TMDCs grown *via* the CVD method possess intrinsic strain owning to the thermal expansion mismatch between the substrate and the material at the high growth temperature.[1,11,12] This intrinsic strain results in modification of the band structure, which could affect its recombination dynamics. Theoretical calculations of band structure as a function of strain show that high biaxial tensile strain in WSe_2 monolayer leads to indirect bandgap transition.[13] Therefore, the band structure modification from intrinsic biaxial tensile strain can possibly reduce the PL of as-grown WSe_2 monolayer. However, it is important to note that the exact band structure of TMDCs is yet to be understood. In addition to the impact of band structure change, the quenched PL in the as-grown samples could be a result of the close coupling to the surface roughness of fused silica or electronic coupling between the semiconductor and the substrate.[14]

The dependence of the PL QY as a function of the excitation intensity (i.e., generation rate) is shown in Fig. 3a for an exfoliated monolayer, and a CVD monolayer before and after SEMD. The data depicts the dramatic enhancement of PL QY upon SEMD process at the generation rates spanning six orders of magnitudes. The QY exhibits a sublinear excitation pump-power dependence with a peak value of 60% at the low generation rates followed by a drop at high generation rates ($>\sim 10^{18}$ $cm^{-2}s^{-1}$). The recombination kinetics of the TMDCs have been studied previously on as-exfoliated and TFSI-treated TMDCs.[15,16] The sublinear behavior of QY at high excitation levels has been attributed to biexcitonic non-radiative recombination process. In particular, the biexcitonic recombination rate in our synthetic WSe_2 monolayer after SEMD is much lower than that of TFSI-treated MoS_2 monolayer with near-unity PL QY.[17] The low

biexcitonic recombination rate of WSe_2 is attractive as it determines the onset of the generation rate at which the QY drop takes place, thus ultimately affecting the QY at high pump-power. For light emitting devices, the QY at high pump-power is the figure of merit for projecting the efficiency as the device is operated at high charge injection levels to achieve high brightness. We obtain a PL QY of ~12% at the high pump-power of 120 W cm^{-2}, which corresponds to generation rate of 3.5×10^{19} $cm^{-2}s^{-1}$. Notably, this is the highest reported PL QY at this high injection regime for TMDCs, and is 20 times higher value than that of TFSI-treated MoS_2 monolayer with near-unity low pump-power PL QY.[17] This presents an important advantage of WSe_2 over MoS_2 for light emitting devices, as high current density operations can be envisioned.[18]

TRPL measurements are shown in Fig. 3b and Fig. S8. The extracted lifetime values are consistent with the PL QY measurement shown in Fig. 3a. Particularly for grown WSe_2 monolayers after SEMD, we observe a lifetime of 4.1 ns, while exfoliated and as-grown samples show lifetimes of one or sub-one nanosecond, respectively. In addition, we performed absorption measurements on as-exfoliated, as-grown, and after SEMD as shown in Fig. 3c. Consistent with previous results, we observe a shift in the A and B exciton resonances for the as-grown samples with the biaxial tensile strain, while no measurable shift is measured in the C exciton resonance,[11,19] which is consistent with previous report on bending experiments.[4] However, it should be noted that the strain was uniaxial for those experiments.

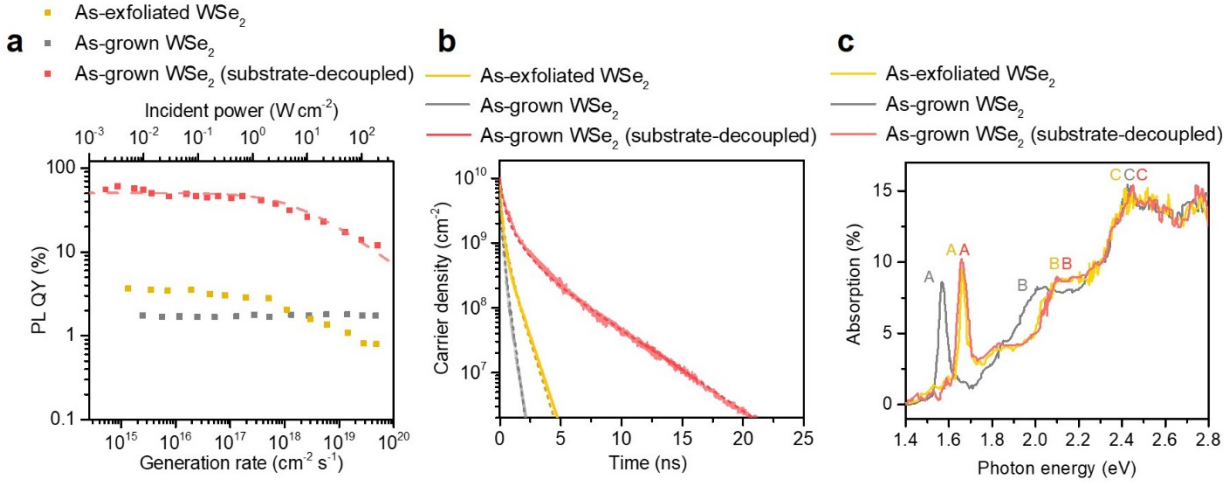

Fig. 3. a, Pump-power dependence, **b,** TRPL decay, and **c,** absorption spectra of as-grown, substrate-decoupled, and as-exfoliated WSe_2 monolayers. Additional TRPL decay curves are shown in Fig. S8.

Lastly, we show the scalability of the growth and SEMD process by demonstrating a centimeter scale WSe_2 monolayer film with bright PL. The growth conditions of centimeter scale monolayer films are specified in the Methods section. Fig 4 (a and b) are representative optical microscopic

images of a single crystalline WSe_2 domain with short growth time of 20 minutes and monolayer film samples with longer growth time of 45 minutes, respectively, on fused silica. Fig. 4c is a representative photograph of fused silica substrate after monolayer film growth. The monolayer film samples were excited by a blue LED with an incident power density of 0.2 W cm^{-2}, as illustrated in Fig. 4d. Using this excitation method, microscopic PL images of WSe_2 monolayer film before and after SEMD were captured with a CCD, and is shown in Fig. 4 (e and f). The microscopic PL image shows uniformly bright PL after SEMD. Furthermore, macro-scale PL imaging was performed using a commercial CMOS camera with the cold filter removed before and after SEMD of as-grown monolayer film. While the emission of the as-grown WSe_2 monolayer cannot be observed in this measurement configuration due to its low PL QY (Fig. 4g), the sample after SEMD results in a very strong emission from the monolayer film, as shown in Fig. 4h.

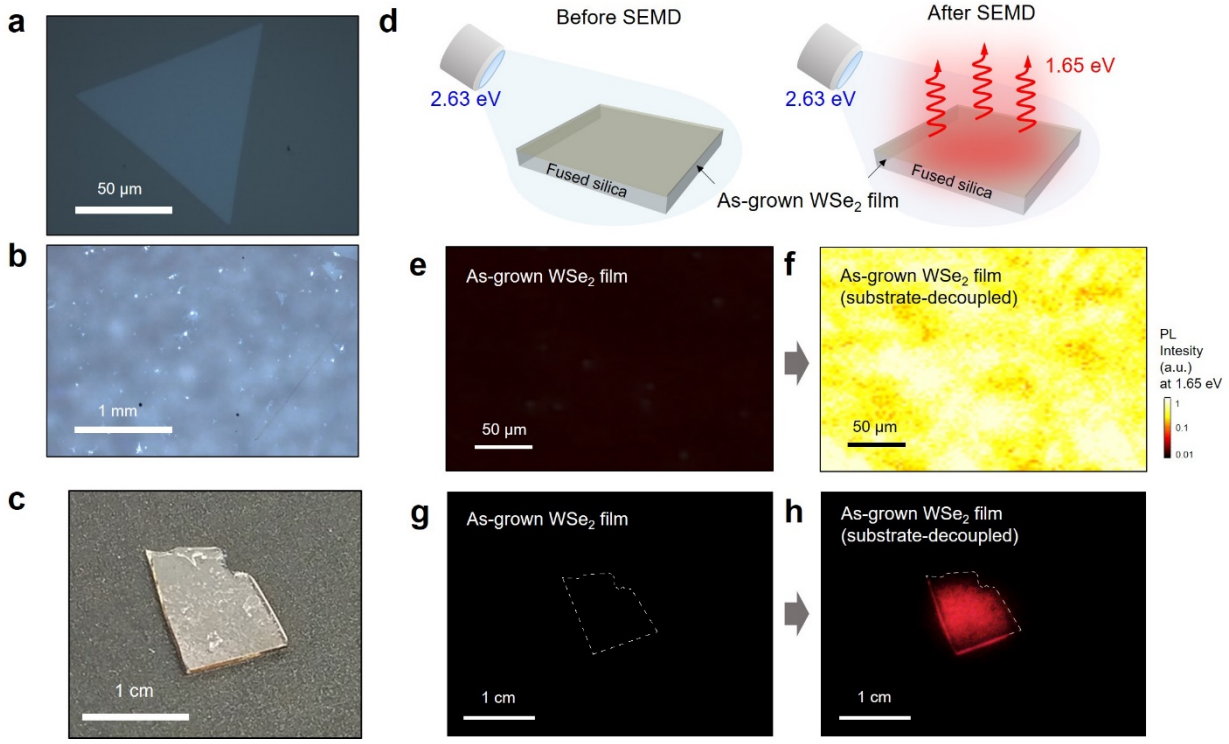

Fig. 4. Optical microscopic images of **a,** single crystalline monolayer WSe_2 and **b,** monolayer WSe_2 film grown on fused silica. **c,** Photographic image of a centimeter scale WSe_2 film sample on fused silica. **d,** Schematic illustration describing the macro-scale PL imaging of a centimeter scale monolayer WSe_2 film on fused silica. High magnification PL images of **e,** as-grown and **f,** post SEMD process monolayer WSe_2 film. Note that the images were taken using a 1.65 eV bandpass filter which blocks the emission from the as-grown monolayer and plotted on a logarithmic scale. Macro-scale PL images of a centimeter scale grown WSe_2 film **g,** before and **h,** after the SEMD process. The images were taken using a commercial CMOS camera with the cold filter removed and a long-pass filter to block the excitation signal and the power density was 0.2

W cm^{-2}.

In summary, we demonstrate a pathway to achieve scalable WSe_2 monolayers with high PL QY for optoelectronic applications. Upon achieving the high quality growth conditions *via* promotor ratio tuning, we find that the key requirement for probing the intrinsic optical property of the synthetic material is to decouple as-grown material from the substrate. We achieved this decoupling *via* the SEMD process. The effect of SEMD on monolayers is characterized by electron diffraction, absorption and PL spectroscopy. As the result, we observe PL QY of ~60% in synthetic WSe_2 monolayers, which is the highest reported value for grown TMDC monolayers and is also higher than mechanically exfoliated WSe_2 monolayers by an order of magnitude. The results demonstrate that through proper material processing, TMDC monolayers with high optoelectronic quality can be obtained by direct growth over large areas.

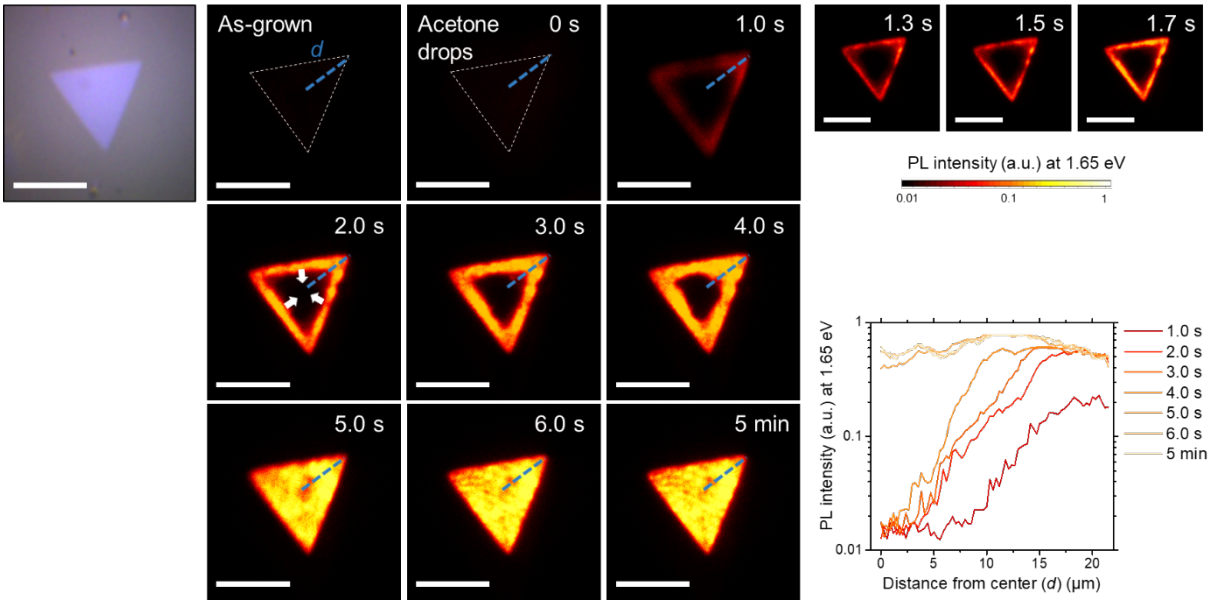

Fig. S1. *In-situ* PL imaging of as-grown WSe_2 monolayer during the SEMD process. The scale bars are 30 μm for all images. Note that the PL images were taken with 1.65 eV bandpass filter to block the emission from as-grown WSe_2 monolayer. The bottom right plot shows the PL intensity profile of the WSe_2 monolayer at 1.65 eV during the SEMD process.

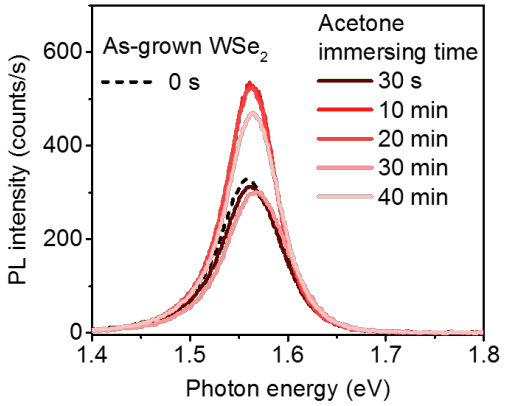

Fig. S2. PL spectra of as-grown WSe_2 monolayer immersed in acetone over time at a pump power of 3 W cm^{-2}.

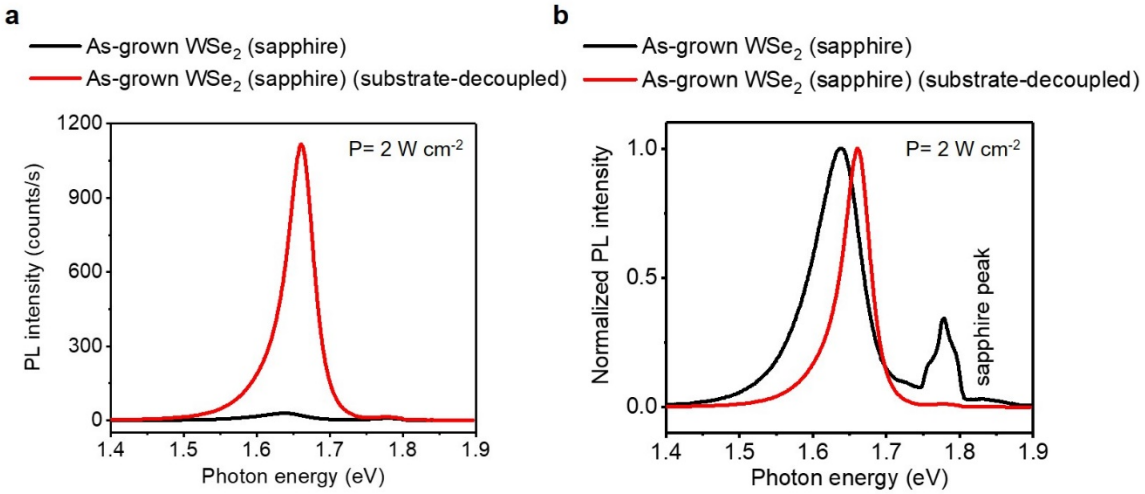

Fig. S3. a, PL Spectra and **b,** normalized PL spectra of as-grown WSe_2 on sapphire substrate, before and after the SEMD process.

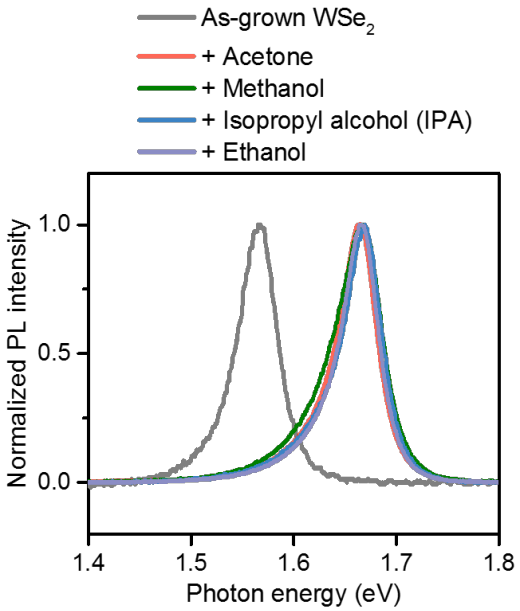

Fig. S4. Normalized PL spectra of as-grown WSe_2 monolayer before and after the SEMD using different solvents, measured at a pump power of 2 W cm^{-2}.

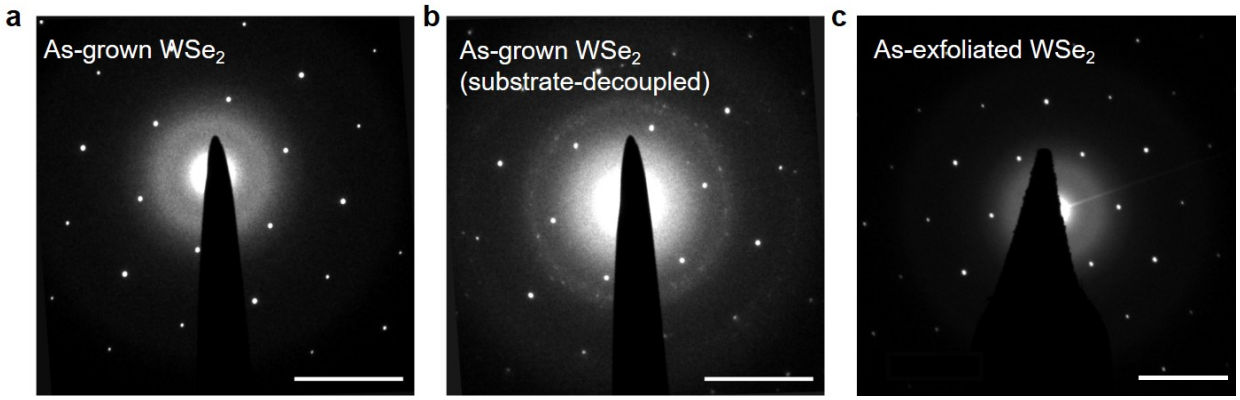

Fig. S5. Electron diffraction patterns of WSe_2 monolayer grown on SiO_2 TEM grids **a,** before and **b,** after the SEMD process, and **c,** exfoliated WSe_2 monolayer. The scale bars are 5 nm^{-1}.

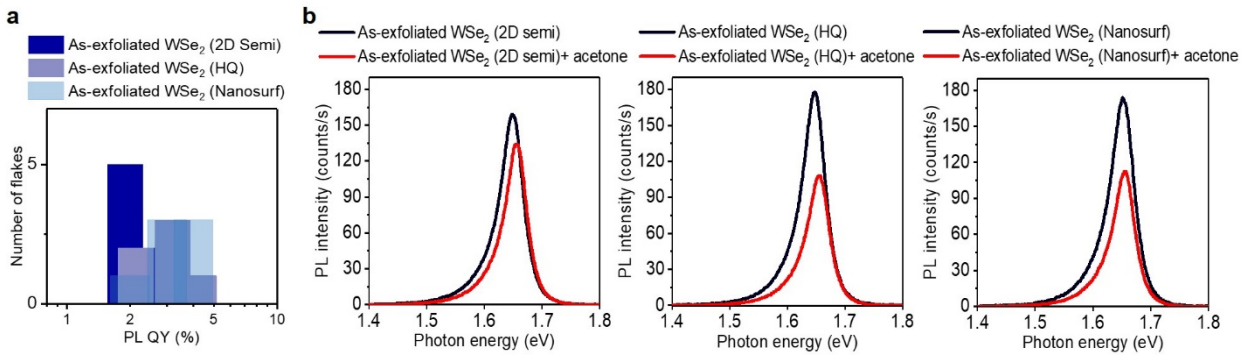

Fig. S6. a, Histogram showing the PL QY of as-exfoliated WSe_2 monolayers prepared from bulk crystals provided by three different vendors. **b,** PL spectra of exfoliated WSe_2 monolayer before and after acetone evaporation, measured at a pump power of 1 W cm^{-2}.

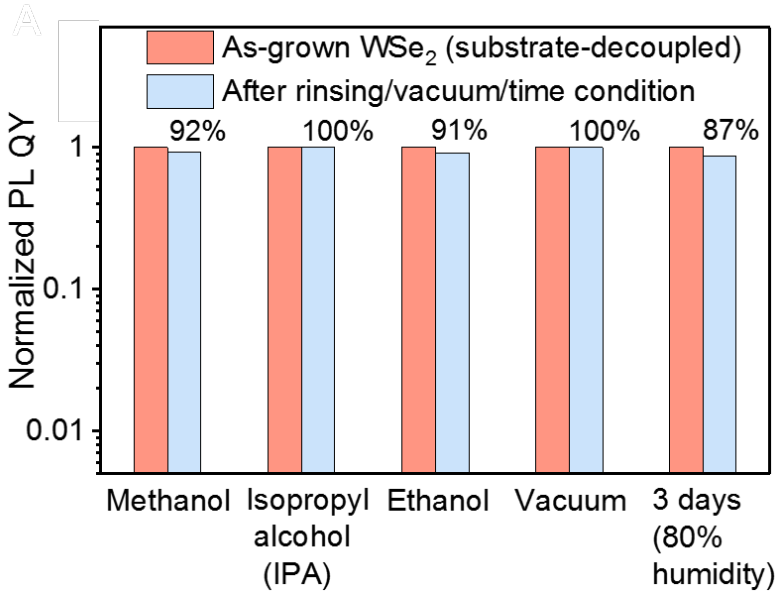

Fig. S7. PL QY of post SEMD process WSe_2 monolayer after various processing and condition, measured at an excitation power of 2 W cm^{-2}.

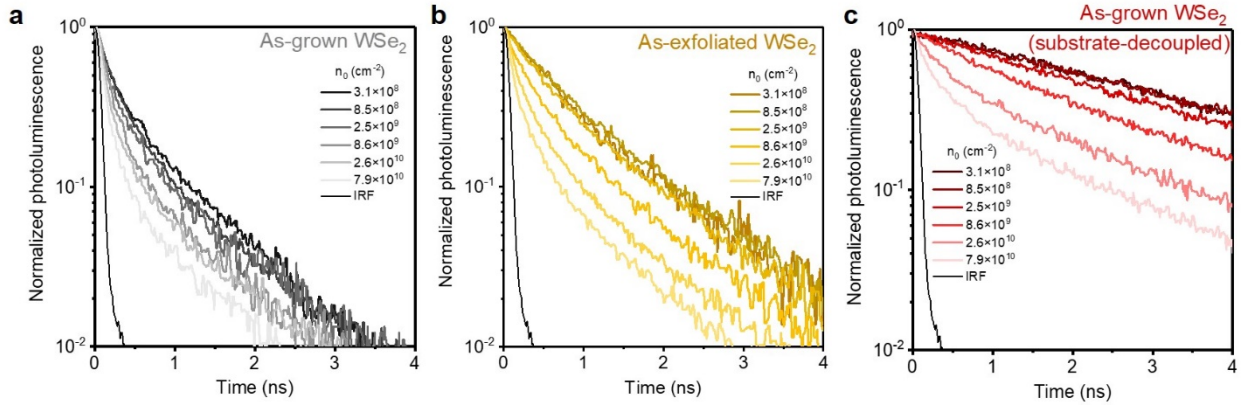

Fig. S8. Radiative decay spectra of **a,** as-grown, **b,** as-exfoliated, and **c,** post SEMD process WSe_2 monolayer measured at different pump fluence.

Experimental and theoretical details

WSe_2 Growth and Transfer

The utilized WSe_2 monolayers in this work resemble the growth process described in detail in previous report.[11] However, further optimizations have been made, and the WSe_2 monolayers were grown with predominantly with two conditions. One growth condition was to produce single crystalline domains ranging from 10 to 100 μm, and another growth condition was used to produce centimeter scale monolayer WSe_2 films. Both growth processes were performed *via* low pressure (~3 Torr) CVD with presence of Ar/H_2 as the carrier gas. All WSe_2 monolayers studied in the main text were grown on quartz substrate, except for Fig. S5 on sapphire substrate. The substrates had been previously cleaned by 10 minutes of sonication in acetone and IPA. The cleaned substrates were loaded into the downstream of the furnace. For the micro-scale WSe_2 samples, Ceramic boat containing mixture of KBr and WO_3 at the weight ratio of 1:2 is placed next to the substrates with KBr as the promotor, similar to the process described in reference.[9] This promotor-to-precursor weight ratios between KBr and WO_3 were tuned to optimize the growth. The utilized weight ratios in the manuscript consist of 1:2, 1:1, and 2:1. After placing another ceramic boat with Se at the upstream, the heating zones are ramped up to temperature of 850 ºC and 130 ºC respectively, and the synthesis begins with presence of H_2. The growth is performed for 20 minutes upon the introduction of H_2. For the WSe_2 monolayer film, a ceramic boat containing mixture of KBr and WO_3 at the weight ratio of 1:1, and the growth is done for 45 minutes instead of 20 minutes.

Optical Characterization

For steady-state and transient optical characterization and calibration, the same instruments and procedures were used here as our previous study.[20] As an excitation source, an Ar^+ laser (Lexel 95) with 514.5 nm line was utilized in steady-state PL and the power density was adjusted by neutral density filters and simultaneously monitored by photodiode power sensor (ThorLabs S120C). It should be noted that the ratio of laser power on the diode to incident power onto sample was 50 so that the low laser power can be accurately measured. A 50x MD Plan (Olympus) objective lens (NA = 0.55) was used for all measurements. A Si CCD detector (Andor iDus BEX2-DD) on an f = 340 mm spectrometer with a 150 g/mm grating was used to collect the steady-state PL spectra and the dark background of CCD was measured and subtracted each time from the acquired signal. Calibration for the external sample PL efficiency was performed using the wavelength-dependent instrument function and the collection efficiency of the instrument which was previously described in our work.[17] The absolute internal PL QY was extracted from the measured external quantum efficiency using the quantitative absorption at the pump wavelength and by the fraction of light within escape cone ($1/4n^2$, where n is the refractive index of the medium). Time-resolved measurements were performed with a 514.5 nm line source (2 nm bandwidth, 20-30 ps pulse duration) selected from a supercontinuum laser (Fianium WhiteLase SC-400) using a double monochromator. The signal was subsequently detected using a single photon counting avalanche photodiode (IDQuantique) with a time-correlated single photon counting module (Becker-Hickl GmbH). *In-situ* PL imaging was performed using the 514.5 nm Ar^+ laser with a diffuser as an excitation source. A fluorescence microscopy setup with a 470 nm LED as an excitation source was used for centimeter scale film imaging and the images were acquired using a commercial camera with a 58 mm lens (f/5.6) after removing a cold filter where the excitation power density on the sample plane was ~0.2 W/cm^2. A 550 nm colored glass long-pass filter was used to block the excitation signal for PL imaging as well as PL spectroscopy measurements.

Transmission Electron Microscopy

Diffraction data were collected on an FEI Titan at 300 keV. All images, including diffraction from a polycrystalline Cu standard, were collected with the same microscope alignments. To correct for small amounts of ellipticity in the diffraction patterns due to microscope aberrations, peak positions were identified in the Cu diffraction data. A correction matrix was calculated from the elliptical fit to the points. The correction matrix was then used to determine a corrected set of image coordinates. Resampling the images according to the corrected coordinates yielded corrected images. After calculating and applying the correction to the Cu standard, the same procedure was carried out on the WSe_2 diffraction patterns.

References

1 Liu, Z. *et al.* Strain and structure heterogeneity in MoS2 atomic layers grown by chemical vapour deposition. *Nature Communications* **5**, 5246 (2014).

2 Plechinger, G. *et al.* Control of biaxial strain in single-layer molybdenite using local thermal expansion of the substrate. *2D Materials* **2**, 015006 (2015).

3 Kim, J. *et al.* Observation of ultralong valley lifetime in WSe2/MoS2 heterostructures. *Science Advances* **3**, e1700518 (2017).

4 Desai, S. B. *et al.* Strain-Induced Indirect to Direct Bandgap Transition in Multilayer WSe2. *Nano Letters* **14**, 4592-4597 (2014).

5 Cao, Z. & Dobrynin, A. V. Polymeric Droplets on Soft Surfaces: From Neumann's Triangle to Young's Law. *Macromolecules* **48**, 443-451 (2015).

6 Nadermann, N., Hui, C.-Y. & Jagota, A. Solid surface tension measured by a liquid drop under a solid film. *Proceedings of the National Academy of Sciences* **110**, 10541 (2013).

7 Hui, C.-Y. & Jagota, A. Planar equilibrium shapes of a liquid drop on a membrane. *Soft Matter* **11**, 8960-8967 (2015).

8 Schulman, R. D. & Dalnoki-Veress, K. Liquid Droplets on a Highly Deformable Membrane. *Physical Review Letters* **115**, 206101 (2015).

9 Li, S. *et al.* Halide-assisted atmospheric pressure growth of large WSe2 and WS2 monolayer crystals. *Applied Materials Today* **1**, 60-66 (2015).

10 Schmidt, P., Binnewies, M., Glaum, R. & Schmidt, M. *Chemical vapor transport reactions–methods, materials, modeling*. (InTech Rijeka, Croatia, 2013).

11 Ahn, G. H. *et al.* Strain-engineered growth of two-dimensional materials. *Nature Communications* **8**, 608 (2017).

12 Amani, M. *et al.* High Luminescence Efficiency in MoS2 Grown by Chemical Vapor Deposition. *ACS Nano* **10**, 6535-6541 (2016).

13 Johari, P. & Shenoy, V. B. Tuning the Electronic Properties of Semiconducting Transition Metal Dichalcogenides by Applying Mechanical Strains. *ACS Nano* **6**, 5449-5456 (2012).

14 Yu, Y. *et al.* Enhancing Multifunctionalities of Transition-Metal Dichalcogenide Monolayers via Cation Intercalation. *ACS Nano* **11**, 9390-9396 (2017).

15 Amani, M. *et al.* Recombination Kinetics and Effects of Superacid Treatment in Sulfur- and Selenium-Based Transition Metal Dichalcogenides. *Nano Letters* **16**, 2786-2791 (2016).

16 Goodman, A. J., Willard, A. P. & Tisdale, W. A. Exciton trapping is responsible for the long apparent lifetime in acid-treated MoS2. *Physical Review B* **96**, 121404 (2017).

17 Amani, M. *et al.* Near-unity photoluminescence quantum yield in MoS2. *Science* **350**, 1065 (2015).

18 Lien, D.-H. *et al.* Large-area and bright pulsed electroluminescence in monolayer semiconductors. *Nature Communications* **9**, 1229 (2018).

19 Li, Y. *et al.* Measurement of the optical dielectric function of monolayer transition-metal dichalcogenides: MoS2, MoSe2, WS2, and WSe2. *Physical Review B* **90**, 205422 (2014).

20 Kim, H., Lien, D.-H., Amani, M., Ager, J. W. & Javey, A. Highly Stable Near-Unity Photoluminescence Yield in Monolayer MoS2 by Fluoropolymer Encapsulation and

Superacid Treatment. *ACS Nano* **11**, 5179-5185 (2017).

2.4 Neutral exciton diffusion in monolayer MoS_2*

While diffusion in monolayer semiconductors has been studied extensively,[1-10] the effect of background carriers has been largely overlooked. Since almost all as-exfoliated monolayer semiconductors have some amount of unintentional doping,[11] a mixture of excitons and trions are created after photoexcitation and previous approaches have produced an averaged diffusion length of both excitons and trions. In this work, we electrostatically tune the background carrier concentration of monolayer MoS_2, a prototypical monolayer semiconductor, to retrieve the separated exciton and trion diffusion length. Our findings demonstrate that excitons and trions in monolayer MoS_2 have very different diffusion lengths ($1.5\mu m$ and $300\ nm$ at a power density of $0.6\ Wcm^{-2}$, respectively). This finding has wide implications for the design of excitonic devices utilizing monolayer semiconductors.

We tune the background carrier concentration (electron and hole population densities) of the monolayer MoS_2 by varying the back-gate voltage (V_g) in a capacitor structure (Fig. 1a). The schematic of the device is shown in Fig. 1a, and an optical micrograph of a device is shown in the inset of Fig. 1a. We also tune the photocarrier generation rate by varying the incident pump power. MoS_2 monolayers are mechanically exfoliated on top of PMMA (100 nm), which is spin-coated on SiO_2 (50 nm)/Si substrate. The Au contacts (thickness 30 nm) are then transferred on the monolayer using a dry transfer technique.[11] Exciton recombination in monolayer MoS_2 was probed spatially, spectrally and temporally in an inverted fluorescence microscope (Fig. 1b). PL was excited at $\lambda = 532\ nm$ wavelength by either a continuous wave (CW) laser or a 100 fs pulsed laser focused to a near-diffraction-limited spot with a full width at half maximum (FWHM) of $w_0 = 287\ nm$. When excited by the CW laser, the resulting PL is either imaged or sent to a spectrometer. When excited by the pulsed laser, the PL is sent to a time-resolved single photon counting detector, which is then scanned across the image to obtain a map of the time-dependent exciton density as a function of position. All measurements reported in this paper are taken at room temperature, in an ambient lab environment.

* The following section was published in a similar form in ACS Nano. (S. Z. Uddin, H. Kim, M. Lorenzon, M. Yeh, D.-H. Lien, E. S. Barnard, H. Htoon, A. Weber-Bargioni, A. Javey, "Neutral Exciton Diffusion in Monolayer MoS_2", ACS Nano, 14, 13433–13440, 2020)

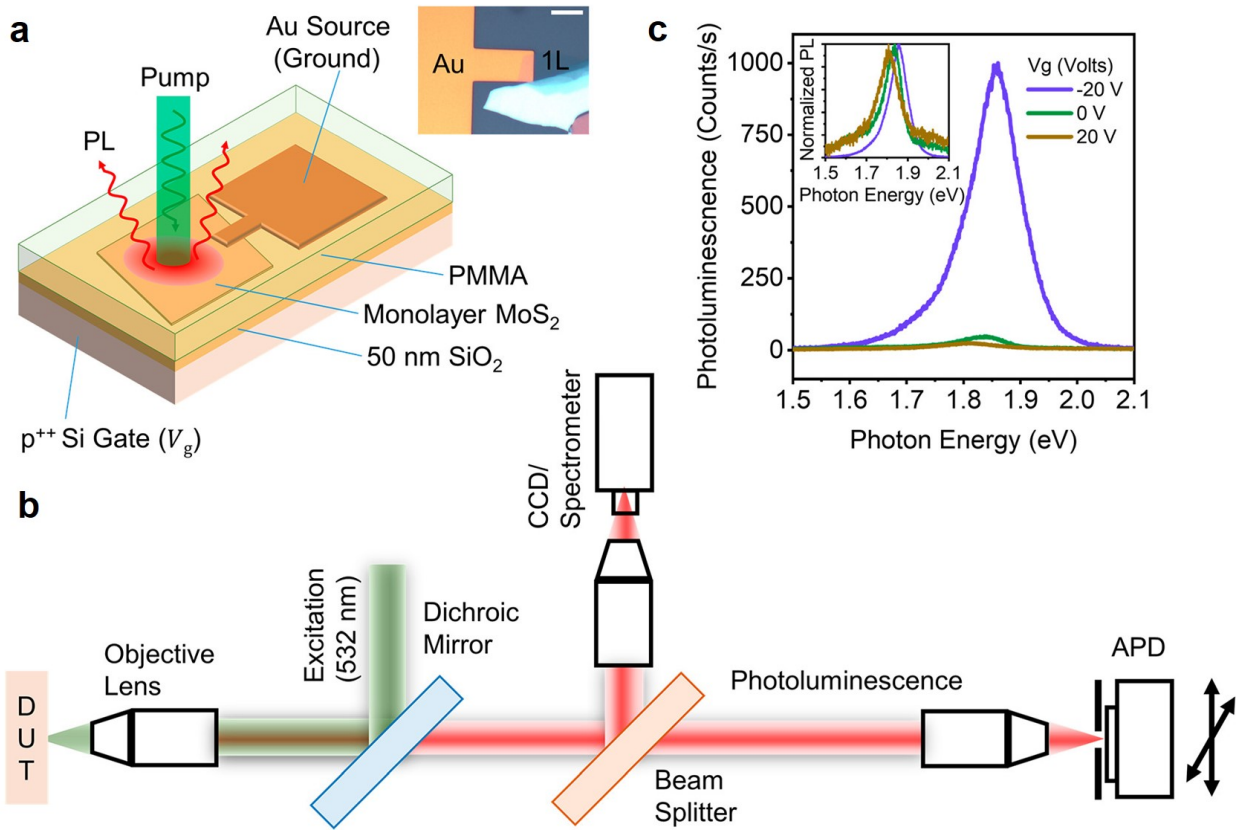

Fig. 1. a, Schematic of the device, inset shows optical micrograph of the device (Scale bar $10\ \mu m$). **b**, Schematic of the exciton diffusion imaging setup. Photoluminescence excited by either pulsed or continuous wave excitation can be sent to a camera for imaging, a spectrometer for PL spectra or an APD for time-resolved single photon counting. The time resolved APD can be scanned across the emission spot to obtain a map of emission intensity as a function of position and time. **c**, PL spectra of the MoS_2 monolayer device under gate voltages V_g = -20 V, 0 V and 20 V at the pump density of 10^2 Wcm^{-2}.

We first discuss the results of CW excitation. The PL spectra (Fig. 1c) of a MoS_2 monolayer measured at V_g = -20 V and 0 V show a ~20-fold difference in the PL peak intensity at a pump power of 10^2 Wcm^{-2}, with a peak energy shift of 30 meV. This difference in PL intensity and spectra has been attributed to the different photo-emitting quasiparticles in the monolayer[3] (Fig. 2). The time-dependent concentrations of excitons, trions and background carriers in a monolayer semiconductor are locally determined by three dynamic processes: generation, recombination and transport (Fig. 2). At a specific location, exciton concentration increases if they are generated from a photon-absorption event or a trion-ionization at that location, or if excitons diffuse in from surrounding points. Concurrently, exciton concentration decreases through trion formation, radiative recombination and biexciton annihilation. Similar generation, recombination and transport processes also occur for trions. The ratio of exciton and trion concentration is determined

by the local background carrier concentration, which can be controlled by the gate voltage.[11] As-exfoliated monolayer MoS_2 is electron-rich due to substrate-induced doping and intrinsic chalcogenide vacancies.[12] At V_g = -20 V, the background electrons are removed from the monolayer MoS_2 and it is close to intrinsic (Fermi level is at mid-bandgap). In this case, emission is observed primarily from neutral excitons which show high PL intensity. Positive V_g moves the Fermi level closer to the conduction band, introducing a large number of background electrons that turn photogenerated excitons into trions. These negative trions show low PL intensity. As both neutral excitons and negative trions coexist at V_g= 0 V, previously reported diffusion lengths of as-exfoliated MoS_2 monolayers are a result of combined diffusion from both excitons and trions and do not reflect the true neutral exciton diffusion length in MoS_2.

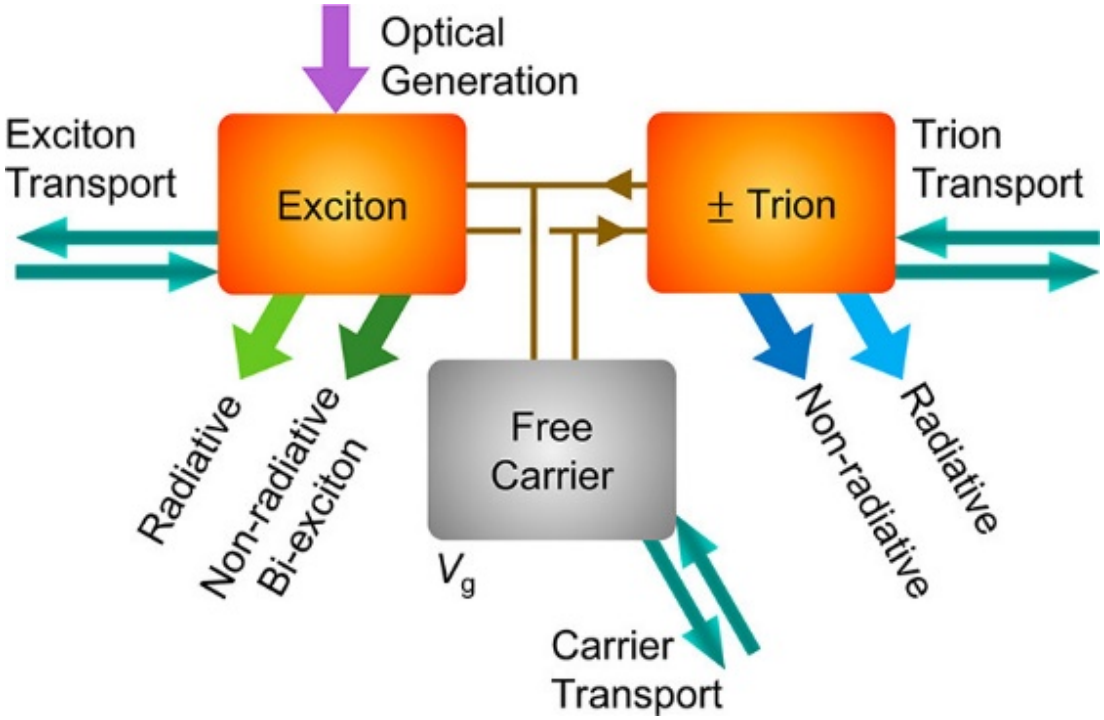

Fig. 2. In a differential area, exciton concentration increases by 1. generation upon absorption of a photon, 2. exciton transport into the area resulting from concentration or potential gradients, and 3. ionization of trions. Exciton concentration decreases by 1. trion formation, 2. radiative recombination and 3. bi-excitonic recombination. Similar generation and recombination processes occur for trions. The ratio of excitons and trions are controlled by the background carrier concentration, which also can drift and diffuse.

PL images of a MoS_2 monolayer excited by a diffraction-limited CW laser at different V_g and different pump powers are shown in Fig 3. In the figure, images in the same row are captured at the same pump power, while images in the same column are captured at the same V_g. For the lowest

pump power, we note that PL at V_g= -20 V is bright, while at V_g= 20 V it is below the noise floor, indicating neutral excitons are much brighter than the negative trions. For neutral excitons, (V_g= -20 V column) slight power dependence is observed in the measured diffusion map. Also, for all powers, neutral excitons diffuse much further than the negative trions. This is related to the difference in their effective lifetime. As neutral excitons have longer effective lifetime (~10 ns) compared to trions (~50 ps),[11] they also diffuse to a larger distance compared to trions.

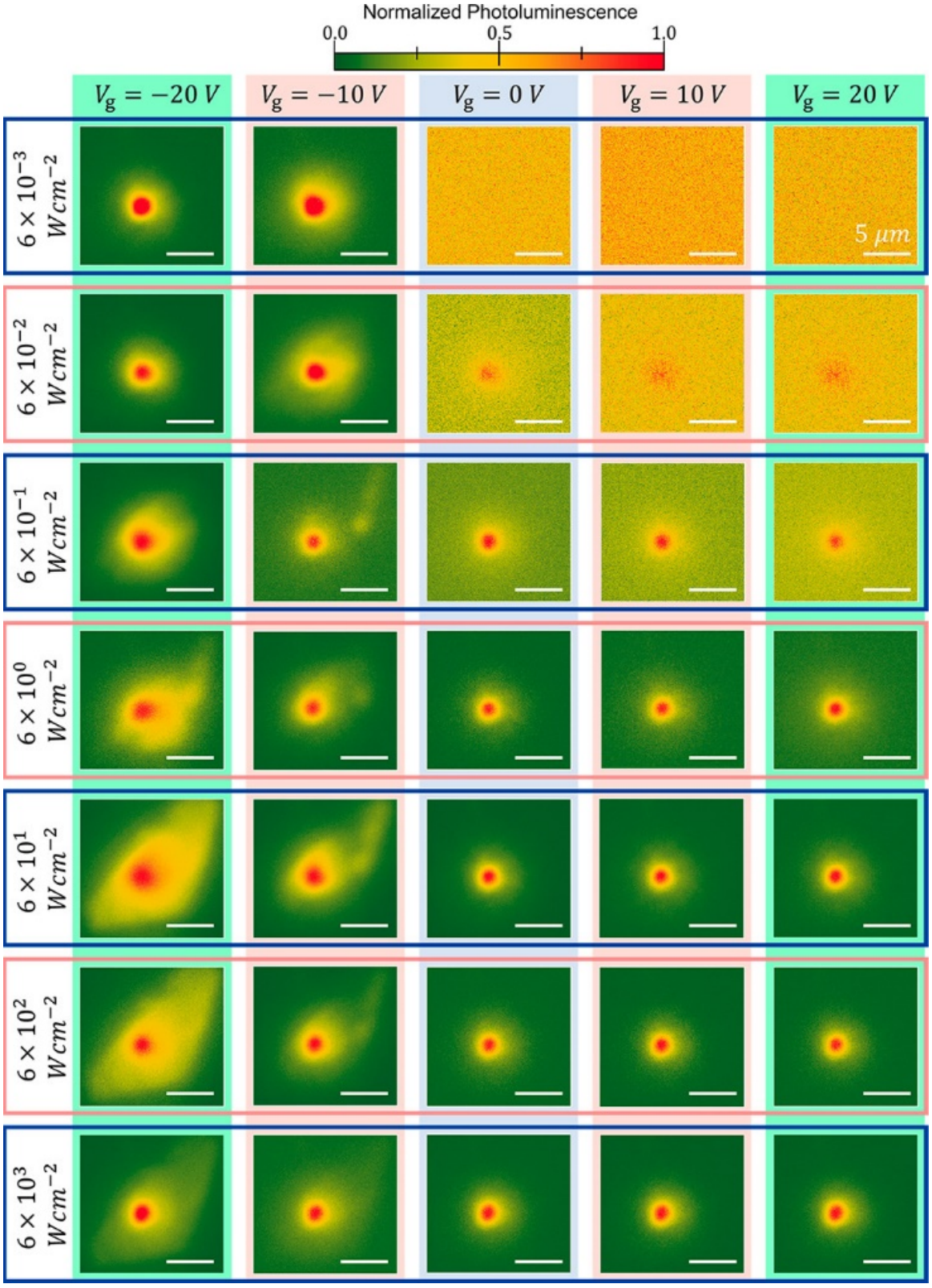
Normalized Photoluminescence
0,0
0,5
1,0
$V_g = -20\ V$
$V_g = -10\ V$
$V_g = 0\ V$
$V_g = 10\ V$
$V_g = 20\ V$
$6 \times 10^{-3}\ Wcm^{-2}$
$6 \times 10^{-2}\ Wcm^{-2}$
$6 \times 10^{-1}\ Wcm^{-2}$
$6 \times 10^{0}\ Wcm^{-2}$
$6 \times 10^{1}\ Wcm^{-2}$
$6 \times 10^{2}\ Wcm^{-2}$
$6 \times 10^{3}\ Wcm^{-2}$
5 μm

Fig. 3. PL excited by a CW laser focused on a diffraction-limited spot for various pump powers and gate voltages. Images in the same row have the same pump power, and in the same column have the same gate voltage. Scale bar is $5\ \mu m$. Radial anisotropy arises from the finite size of the monolayer.

PL QY is defined as the ratio of the number of photons the material radiates to the number of absorbed photons. We first present the PL QY of monolayer MoS_2 in Fig. 4a as a function of pump power and V_g. The details of calibrated PL QY measurement and quantitative recombination kinetics at different V_g and pump have been discussed elsewhere.[11] At V_g= -20 V all photogenerated carriers create neutral excitons, as there are no excess background carriers. We note that the PL QY *vs*. pump profile at V_g= -20 V has two distinct regions, indicated by different background colors in Fig. 4a. At low pump the PL QY does not change with pump. PL QY reaches near unity in this linear regime. At high pump the PL QY decreases with pump power. This nonlinear droop has been attributed to the bi-exciton annihilation process at high exciton densities.[13] At V_g= 20 V a large concentration of excess electrons accumulates in the monolayer, and almost all photogenerated carriers turn into negative trions (Fig. 4b). Trions can non-radiatively recombine by transferring their excess energy into secondary electrons in an Auger-like process,[14] so the PL QY is low.

We now present the diffusion length of monolayer MoS_2 in Fig 4c as a function of pump power and V_g. Throughout the manuscript, we define the squared width of the diffusion pattern as

$$w^2(t) = \frac{\int d^2r|r|^2 I(r,t)}{\int d^2r I(r,t)} \tag{1}$$

where $I(r,t)$ is PL intensity, r is the radial coordinate, t is time and the integrations are limited to the area of the monolayer. The steady state diffusion length (L_D) is then defined as the mean-square radius of the diffusion map deconvoluted by the laser spot size. At low pump we observe diffusion lengths of $1.5\ \mu m$ and $300\ nm$ at $V_g = -20\ V$ and $20\ V$, respectively. At V_g= -20 V, the diffusion length shows a slight increase over six orders of magnitude of pump power, while at V_g= 20 V the diffusion length is low at moderate pumps and increases by ~5x at high pump. Note that we could not measure the diffusion length of trions at very low pumps due to low signal.

To extract the diffusion coefficient of neutral excitons, we extend the kinetic model of exciton recombination to incorporate diffusion. Considering only neutral excitons (at V_g= -20 V), we can write the time-dependent continuity equation as:

$$\frac{\partial n_X(r,t)}{\partial t} = \nabla \cdot [D_X(\mathrm{n_X, t})\nabla n_X] + G(r,t) - \frac{n_\mathrm{X}}{\tau_\mathrm{X}} - C_\mathrm{bx} n_\mathrm{X}^2 \tag{2}$$

where n_X and τ_X are the neutral exciton population density and lifetime, respectively, and C_bx is the bi-exciton annihilation coefficient. Both the exciton lifetime (τ_X~$10\ ns$) and bi-exciton

annihilation coefficient (C_{bx}~$3.5\ cm^2s^{-1}$) have been experimentally measured previously[18] and are known. At steady state, $\frac{\partial n_X}{\partial t} = 0$. We consider a Gaussian generation rate given by

$$G(r) = G_0 \exp(-2r^2/w_0^2) \tag{3}$$

where the peak G_0 is determined by pump intensity. The only unknown parameter in Eq. 2 is D_X. We extract an effective diffusion coefficient D_X at different pump intensity that gives the experimentally measured diffusion length shown in Fig. 4c. This extraction process is done by assuming a constant diffusion coefficient and numerically solving Eq. 2 for exciton concentration n_X. The extracted effective diffusion coefficient at different powers is shown in Fig. 4d. We note that the effective diffusion coefficient increases with pump power. This increase in effective diffusion coefficient has been observed in other excitonic systems such as 2D heterostructures and as-exfoliated WS_2 monolayers and is attributed to correlation driven diffusion.[1,3,15] At the lowest pump density where neutral excitons recombine completely radiatively, a diffusion length of $1.5\ \mu m$ and a diffusion coefficient of $2.1\ cm^2s^{-1}$ has been observed for neutral excitons.

Unlike the case of neutral excitons, extracting the trion diffusion coefficient is more complex due to its charged nature. Diffusion of trions would perturb the local charge neutrality, and the free carriers will respond to the resultant lateral electric field. Furthermore, the observed PL is a result of radiative recombination of both excitons and trions. Thus, we calculate an effective diffusion coefficient ($L_D^2/\tau_{\mathrm{T}}^-$) at $V_g = -20\ V$ using the known trion effective lifetime of $\tau_{\mathrm{T}}^- = 50\ ps$.[11] At a pump power density of $0.6\ Wcm^{-2}$, we observe a trion diffusion length of 300 nm (Fig. 4c), which corresponds to an effective diffusion coefficient of 18 cm^2s^{-1}. This large diffusion coefficient could be a result of strong Coulomb interaction between charged trions. We also note that, at very high pump, the diffusion length at any V_{g} will converge to the neutral exciton diffusion length. This is because the number of trions cannot be larger than the number of background carriers, and thus once the trion population saturates, recombination and diffusion must be dominated by excitons. This explains the increase of diffusion length with pump at V_{g}= 20 V and 0 V.

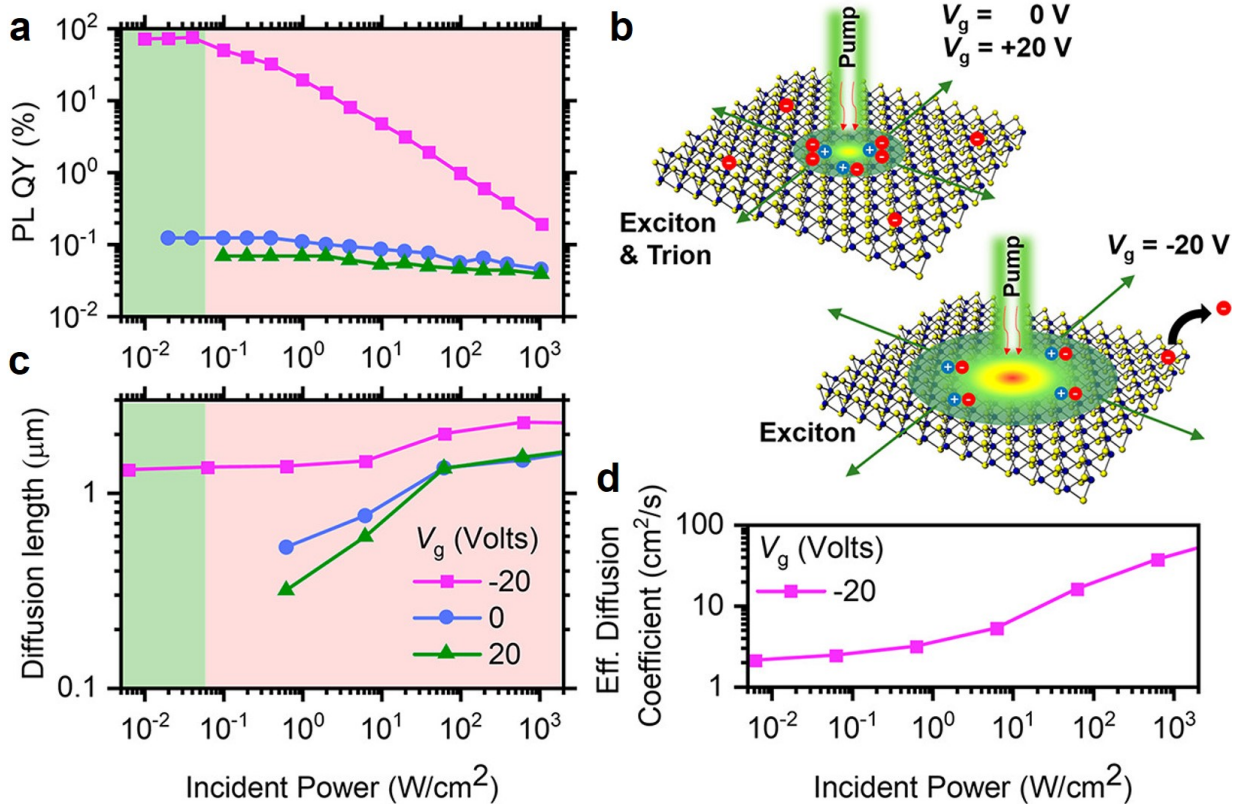

Fig. 4. a, Pump-power dependence of the PL QY for electrostatically-doped MoS_2. **b,** Exciton and trion diffusion in MoS_2. **c,** Diffusion length of a MoS_2 device under V_g = 0V, V_g = -20 V and V_g = 20 V. **d**, Effective diffusion coefficient for neutral excitons in MoS_2 at different pump power.

Now we discuss the results of pulsed excitation. Figure 5a, b, and c show the spatial and temporal evolution of the emission intensity distribution $I(r,t)$ after pulsed excitation at $t = 0$ at V_g= -20 V, 0 V, and 20 V, respectively at a pump fluence of 75 $\mu J cm^{-2}$. We can see the neutral excitons spread further in time due to their considerably longer lifetime. The neutral exciton distribution variance can be obtained directly from the measured intensity distribution variance $\Delta w^2(t) = w^2(t) - w^2(0)$, which is shown in Fig. 5D, E and F for different optical pump fluences at V_g = -20 V, 0V and 20 V, respectively. $\Delta w^2(t)$ does not depend on the width of the initial distribution created by the laser pulse. In general, the variance can be written as

$$\Delta w^2(t) = At^{\alpha} \tag{4}$$

The exponent α characterizes the type of diffusion and A is the empirically observed proportionality factor which has fractional time units. For $\alpha = 1$, we get linear diffusion. In the case of $\alpha > 1$ and $\alpha < 1$ the transport is called superdiffusive and subdiffusive, respectively,

which results from the concentration dependence of the effective diffusion coefficient.[16,17] We note that in monolayer MoS_2 the nature of diffusion changes from linearly diffusive at low pump to subdiffusive at high pump (Fig. 5d). This could be because of exciton-exciton interaction at high pump densities. At low fluence excitons recombine completely radiatively and diffuse linearly with $\alpha = 1$. For linear diffusion, the halved slope of $\Delta w^2(t)$ gives the diffusion coefficient. An effective diffusion coefficient of $\sim 1.2\ cm^2 s^{-1}$ has been found at low fluence, which matches well with the steady state measurements. At high fluence, biexciton recombination dominates the recombination kinetics and subdiffusive ($\alpha < 1$) behavior is observed, indicative of a reaction-diffusion process. This could also be related to the relaxation of nonresonantly excited hot exciton gas by losing its excess kinetic energy[18] and further careful study is required to shed light on these mechanisms. At V_g= 0 V and 20 V, subdiffusive behavior ($\alpha < 1$) is observed (Fig. 5e, f). As previously discussed, this is a result of diffusion of both excitons and trions at high fluence.[19] The PL signal of trions is too low to measure diffusion at low pump.

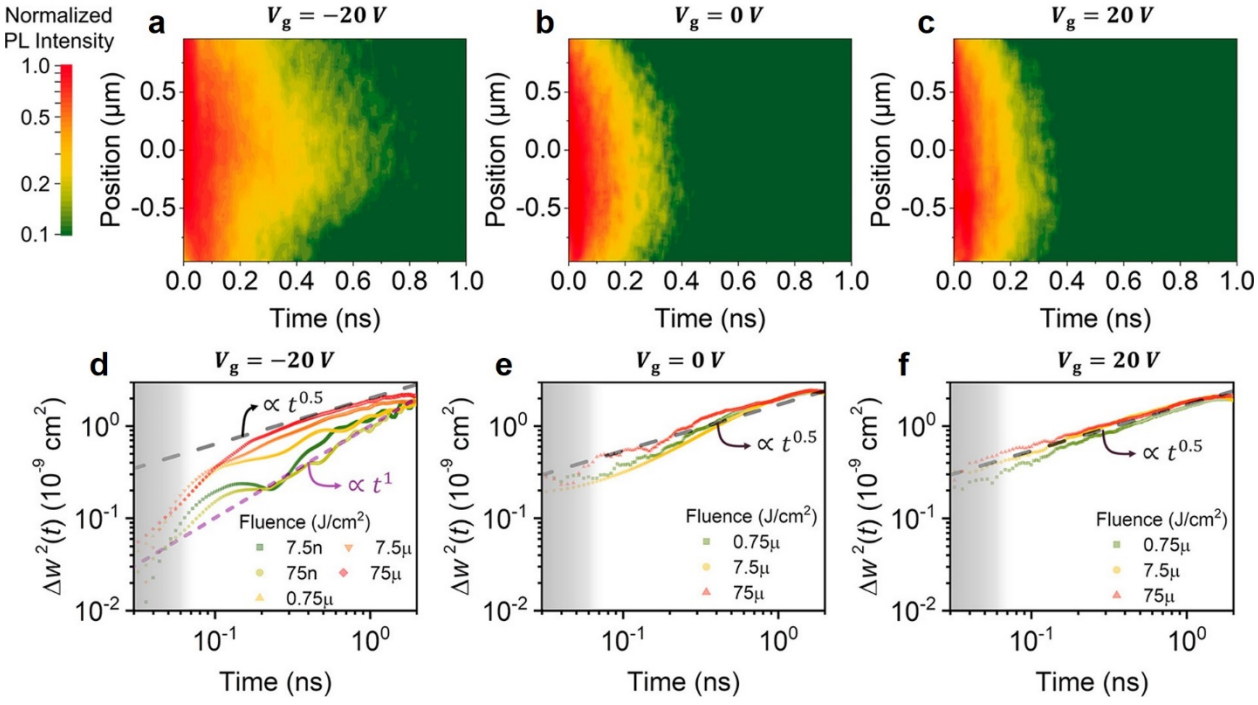

Fig. 5. a, b, c, Map of emission intensity as it evolves in space and time at V_g = -20 V, 0 V, and 20 V, respectively at a pump fluence of 75 $\mu J cm^{-2}$. **d, e, f,** Time evolution of differential squared width for various pump fluence at V_g = -20 V, 0 V and 20 V, respectively. The instrument response function (IRF) has a FWHM of ~50 ps, which is shown as a shaded region.

Exciton diffusion length is not only of essential importance for understanding the energy transport physics in excitonic semiconductors, but also an imperative design consideration for

optoelectronic applications.[20-24] The physical process of bi-exciton annihilation involves the diffusion of excitons and the rate of bi-exciton annihilation increases with diffusivity. In light emitting devices, the emission region must be located at least a diffusion length away from the injection region to avoid quenching. On the contrary, in energy harvesting devices the contacts must be closer to the absorption region to collect excitons. Materials with different diffusion coefficients can therefore be suitable for different applications. Some examples of different classes of excitonic materials with their diffusion lengths are shown in Table 1. Generally, quasi-0D systems such as molecular films and quantum dot films have very low diffusion lengths ($1\ nm - 50\ nm$) at room temperature, as the diffusion mainly occurs by site hopping.[25] One dimensional excitonic semiconductors, such as semiconducting single wall carbon nanotube (SWCNT) have larger ($\sim 300\ nm$) diffusion lengths,[26-28] depending on the chirality and dielectric environment. A two-dimensional excitonic semiconductor, such as the monolayer MoS_2 discussed here can have an exciton diffusion length of ~ 1500 nm and a trion diffusion length of $300\ nm$ at room temperature. In a three-dimensional bulk semiconductor, strong dielectric screening generally leads to low exciton binding energy, so excitons exist only at cryogenic temperatures. At those low temperatures they show the largest diffusion length ($10 - 1000\ \mu m$), however the required operating temperature limits their practical usability. Therefore, among the classes of excitonic semiconductors discussed here, two dimensional materials such as monolayer MoS_2 achieve the highest diffusion lengths at room temperature and are particularly suitable for applications that require a large diffusion length.[20-24] Furthermore, excitons in MoS_2 achieve near-unity PL QY at room-temperature, even in the presence of defects. Exciton transport in MoS_2 can also be tuned by electrostatic doping, strain[4] and dielectric environment,[1,29] further adding to their appeal. These qualities make two-dimensional semiconductors an ideal candidate for future room-temperature excitonic devices.

Dimension	Material	Diffusion Length	Diffusion Coefficient ($cm^2 s^{-1}$)	Reference
Molecules and 0D	Tris(8-hydroxyquinolinato) aluminum, Alq_3	$3 - 25\ nm$	$(3 - 2000) \times 10^{-6}$	[25,30]
	Spin-coated poly (p-phenylene vinylene) (PPV)	$4 - 6\ nm$	6×10^{-4}	[25,31]
	CdSe/CdS core/shell QD film	$19 - 24\ nm$	2×10^{-4}	[32]
	Cesium Lead Bromide Perovskite nanocrystal film	$200\ nm$	0.5	[26]
One Dimensional	Air Suspended (9,8) SWCNT	$290 - 610\ nm$	44	[27]
	Micelle encapsulated SWCNT	$100 \pm 20\ nm$	$2.5 - 10$	[28]
	(6,5) single-wall carbon nanotube (SWCNT)	$120 \pm 25\ nm$	10.7 ± 0.4	[33]

	15 nm wide GaAs quantum wire (15 K)	4 μm	–	[34]
Two Dimensional	AlAs/GaAs Coupled Quantum Well (200 K)	5 μm	3×10^5	[35]
	As-exfoliated Monolayer WSe_2	500 nm-1.8 μm	$0.6 - 1.8$ 2.2 (± 1.1)	[2,4]
	As-exfoliated Monolayer WS_2	$360 - 750$ nm	0.41	[1,36]
	As-exfoliated Monolayer $MoSe_2$	400 nm	12 ± 3	[37]
	Monolayer 2D Perovskite	160 nm	0.06	[38]
Three Dimensional	Undoped Si (11 K)	25 μm	100	[39]
	Doped Silicon (11 K)	24 μm	11	[40]
	Germanium (4.2 K)	900 μm	1000	[41]
	Cu_2O (1.2 K)	70 μm	1000	[42]

Table 1. Exciton diffusion length and diffusion coefficient of various materials. All measurements are at room temperature unless specified.

In summary, we have measured the diffusion length of neutral excitons in monolayer MoS_2. The steady state exciton diffusion length is found to be between $1.5 - 4$ μm depending on the pump intensity. Our measurements demonstrate that with increasing exciton concentration the diffusion coefficient increases and transport of neutral excitons in MoS_2 changes from linear diffusion to subdiffusive. The diffusion coefficient of neutral excitons measured by steady state measurements and time resolved measurements are found to be in excellent agreement. These results are direct spatial and temporal observation of isolated neutral exciton diffusion in a monolayer semiconductor, which will be invaluable for the design and characterization of systems that rely on neutral and charged exciton diffusion at room-temperature.

Experimental and theoretical details

Device Fabrication

TMDC monolayers are mechanically exfoliated on top of PMMA (100 nm), which is spin-coated on SiO_2 (50 nm)/Si substrate. MoS_2 (SPI supplies), WS_2 (HQ Graphene), WSe_2 (HQ Graphene) and $MoSe_2$ (HQ Graphene) were mechanically exfoliated onto 50 nm SiO_2/Si p^{++} substrates. Monolayers were identified by optical contrast. 40 nm thick Au contacts were evaporated on 280 nm SiO_2/Si, and then picked up and placed on the monolayer by a dry transfer method, using PMMA as the transfer medium. Electron-beam lithography was used to open a window in the

transferred PMMA, allowing probe tip contact.

Electrical and Optical Characterization

Devices were charged from a Keithley 2410 Source Meter applied to the gate electrode, while the Au source contact was grounded. The PL QY was measured using a customized micro-PL instrument described in detail in previous study.[11,13] For steady state measurements, a green diode laser was used as the excitation source.[32] Laser source was collimated and then focused to a diffraction-limited spot by a 100X 0.95 NA objective lens. The back aperture of the objective was overfilled to assure diffraction-limited performance. Emission from the sample was collected by the same objective and additionally magnified 5.3X for a total magnification of 530X and imaged on a camera (Andor Neo sCMOS 5.5, sensor size 16.6 mm x 14 mm, 2560 x 2160 pixels) with pixel size 6.5 μm, which provided an effective imaging pixel size of 8.63 nm. A long-pass dichroic filter and two long-pass edge filters (Semrock) were used to remove the excitation laser beam from the PL signal. To ensure no Fresnel broadening of the PL by the top PMMA, we compared the reflected laser profile from a thick reflective MoS_2 with and without top PMMA and found no significant broadening. For time-resolved measurements, a Ti-Sapphire laser along with an OPO was used as the excitation source. The laser beam was collimated and focused by a 100X 0.95 NA objective lens. The back aperture of the objective was overfilled to assure diffraction-limited performance. Emission from the sample was collected by the same objective and imaged on a single-mode fiber (P1-405P-FC-2, Thorlabs) attached to a translation stage (Attocube ECS series) that scanned the emission focal plane. The stage was moved in 5 μm steps corresponding to 50 nm at the sample. The signal was detected by a single-photon counting avalanche photodiode (MPD PDM-series) connected to a time-correlated single-photon counting unit (Picoharp 300). The temporal resolution was approximately 50 ps, as determined by the FWHM of the instrument response function.

We simulated the processes of exciton generation and recombination by discretizing and solving the continuity equation (Eq. 2) in MATLAB. The spatial grid was sampled at 5 nm distances. Time was nonuniformly sampled, denser sampling points when concentration is higher to ensure convergence.[16,17]

References

1 Kulig, M. *et al.* Exciton Diffusion and Halo Effects in Monolayer Semiconductors. *Physical Review Letters* **120**, 207401 (2018).

2 Cadiz, F. *et al.* Exciton diffusion in WSe2 monolayers embedded in a van der Waals heterostructure. *Applied Physics Letters* **112**, 152106 (2018).

3 Zipfel, J. *et al.* Exciton diffusion in monolayer semiconductors with suppressed disorder. *Physical Review B* **101**, 115430 (2020).

4 Cordovilla Leon, D. F., Li, Z., Jang, S. W., Cheng, C.-H. & Deotare, P. B. Exciton transport in strained monolayer WSe2. *Applied Physics Letters* **113**, 252101 (2018).

5 Wang, J. *et al.* Diffusion dynamics of valley excitons by transient grating spectroscopy in monolayer WSe2. *Applied Physics Letters* **115**, 131902 (2019).

6 Glazov, M. M. Phonon wind and drag of excitons in monolayer semiconductors. *Physical Review B* **100**, 045426 (2019).

7 Hao, S., Bellus, M. Z., He, D., Wang, Y. & Zhao, H. Controlling exciton transport in monolayer MoSe 2 by dielectric screening. *Nanoscale Horizons* **5**, 139-143 (2020).

8 Perea-Causín, R. *et al.* Exciton Propagation and Halo Formation in Two-Dimensional Materials. *Nano Letters* **19**, 7317-7323 (2019).

9 Fu, Y. *et al.* Effect of Dielectric Environment on Excitonic Dynamics in Monolayer WS2. *Advanced Materials Interfaces* **6**, 1901307 (2019).

10 Raja, A. *et al.* Dielectric disorder in two-dimensional materials. *Nature Nanotechnology* **14**, 832-837 (2019).

11 Lien, D.-H. *et al.* Electrical suppression of all nonradiative recombination pathways in monolayer semiconductors. *Science* **364**, 468 (2019).

12 Radisavljevic, B., Radenovic, A., Brivio, J., Giacometti, V. & Kis, A. Single-layer MoS2 transistors. *Nature Nanotechnology* **6**, 147-150 (2011).

13 Amani, M. *et al.* Near-unity photoluminescence quantum yield in MoS2. *Science* **350**, 1065 (2015).

14 Jha, P. P. & Guyot-Sionnest, P. Trion Decay in Colloidal Quantum Dots. *ACS Nano* **3**, 1011-1015 (2009).

15 Jauregui, L. A. *et al.* Electrical control of interlayer exciton dynamics in atomically thin heterostructures. *Science* **366**, 870 (2019).

16 Crank, J. *The mathematics of diffusion*. (Oxford university press, 1979).

17 Ghez, R. *A primer of diffusion problems*. (Wiley, 1988).

18 Cordovilla Leon, D. F., Li, Z., Jang, S. W. & Deotare, P. B. Hot exciton transport in WSe2 monolayers. *Physical Review B* **100**, 241401 (2019).

19 Rosati, R., Perea-Causín, R., Brem, S. & Malic, E. Negative effective excitonic diffusion in monolayer transition metal dichalcogenides. *Nanoscale* **12**, 356-363 (2020).

20 Miller, D. A. B. *et al.* Electric field dependence of optical absorption near the band gap of quantum-well structures. *Physical Review B* **32**, 1043-1060 (1985).

21 Lundstrom, T., Schoenfeld, W., Lee, H. & Petroff, P. M. Exciton Storage in Semiconductor Self-Assembled Quantum Dots. *Science* **286**, 2312 (1999).

22 Hagn, M., Zrenner, A., Böhm, G. & Weimann, G. Electric-field-induced exciton transport

in coupled quantum well structures. *Applied Physics Letters* **67**, 232-234 (1995).
23 High, A. A., Hammack, A. T., Butov, L. V., Hanson, M. & Gossard, A. C. Exciton optoelectronic transistor. *Opt. Lett.* **32**, 2466-2468 (2007).
24 High, A. A., Novitskaya, E. E., Butov, L. V., Hanson, M. & Gossard, A. C. Control of Exciton Fluxes in an Excitonic Integrated Circuit. *Science* **321**, 229 (2008).
25 Mikhnenko, O. V., Blom, P. W. M. & Nguyen, T.-Q. Exciton diffusion in organic semiconductors. *Energy & Environmental Science* **8**, 1867-1888 (2015).
26 Penzo, E. *et al.* Long-Range Exciton Diffusion in Two-Dimensional Assemblies of Cesium Lead Bromide Perovskite Nanocrystals. *ACS Nano* **14**, 6999-7007 (2020).
27 Moritsubo, S. *et al.* Exciton Diffusion in Air-Suspended Single-Walled Carbon Nanotubes. *Physical Review Letters* **104**, 247402 (2010).
28 Cognet, L. *et al.* Stepwise Quenching of Exciton Fluorescence in Carbon Nanotubes by Single-Molecule Reactions. *Science* **316**, 1465 (2007).
29 Goodman, A. J. *et al.* Substrate-Dependent Exciton Diffusion and Annihilation in Chemically Treated MoS2 and WS2. *The Journal of Physical Chemistry C* **124**, 12175-12184 (2020).
30 Wu, Y. *et al.* Excitation energy transfer between tris-(8-hydroxyquinoline) aluminum and a red dye. *Applied Physics Letters* **88**, 123512 (2006).
31 Markov, D. E., Amsterdam, E., Blom, P. W. M., Sieval, A. B. & Hummelen, J. C. Accurate Measurement of the Exciton Diffusion Length in a Conjugated Polymer Using a Heterostructure with a Side-Chain Cross-Linked Fullerene Layer. *The Journal of Physical Chemistry A* **109**, 5266-5274 (2005).
32 Lee, E. M. Y. & Tisdale, W. A. Determination of Exciton Diffusion Length by Transient Photoluminescence Quenching and Its Application to Quantum Dot Films. *The Journal of Physical Chemistry C* **119**, 9005-9015 (2015).
33 Hertel, T., Himmelein, S., Ackermann, T., Stich, D. & Crochet, J. Diffusion Limited Photoluminescence Quantum Yields in 1-D Semiconductors: Single-Wall Carbon Nanotubes. *ACS Nano* **4**, 7161-7168 (2010).
34 Nagamune, Y., Watabe, H., Sogawa, F. & Arakawa, Y. One-dimensional exciton diffusion in GaAs quantum wires. *Applied Physics Letters* **67**, 1535-1537 (1995).
35 Grosso, G. *et al.* in *Conference on Lasers and Electro-Optics 2010.* QFI5 (Optical Society of America).
36 Yuan, L. & Huang, L. Exciton dynamics and annihilation in WS 2 2D semiconductors. *Nanoscale* **7**, 7402-7408 (2015).
37 Kumar, N. *et al.* Exciton diffusion in monolayer and bulk MoSe 2. *Nanoscale* **6**, 4915-4919 (2014).
38 Deng, S. *et al.* Long-range exciton transport and slow annihilation in two-dimensional hybrid perovskites. *Nature Communications* **11**, 664 (2020).
39 Tamor, M. A. & Wolfe, J. P. Drift and Diffusion of Free Excitons in Si. *Physical Review Letters* **44**, 1703-1706 (1980).
40 Chen, Y. H. & Lyon, S. A. Photoluminescence and diffusivity of free excitons in doped silicon. *IEEE Journal of Quantum Electronics* **25**, 1053-1055 (1989).
41 Sanada, T., Ohyama, T. & Otsuka, E. Diffusion of excitons and electron-hole drops in

germanium. *Solid State Communications* **17**, 999-1001 (1975).
42 Trauernicht, D. P., Wolfe, J. P. & Mysyrowicz, A. Highly Mobile Paraexcitons in Cuprous Oxide. *Physical Review Letters* **52**, 855-858 (1984).

3

Nonradiative Recombination-Free Monolayer Semiconductors[*]

3.1 Introduction

The upper limit of efficiency that any semiconductors can achieve in a light-emitting device is directly dictated by PL QY, which is a strong function of photocarrier density. Optoelectronic devices that are ubiquitously used for display or lighting such as LEDs often operate in a high electron-hole or exciton density regime, where all semiconductors experience elevated nonradiative carrier recombination and thus diminished PL QY. Previously we have shown that, although 2D TMDC monolayers exhibit near-unity PL QY at low carrier densities, their PL QY lowers significantly at high carrier densities like all other semiconductors.[1] Despite extensive research to advance their material quality and device architecture, the inherent PL QY degradation in 2D TMDC monolayers at high exciton densities remains a major challenge for their utility towards high-performance optoelectronic devices.

Exciton-exciton annihilation (EEA) is a nonradiative process that is predominantly responsible for the nonradiative recombination at high exciton densities in excitonic semiconductors. In this work, we show that EEA is resonantly amplified in TMDC monolayers by van Hove singularities (VHSs) present in their joint density of states. Logarithmic VHSs are a hallmark of two-dimensional

[*] The following section has been submitted for journal publication in a similar form. (H. Kim, S. Z. Uddin, N. Higashitarumizu, E. Rabani, A. Javey, "Inhibited Nonradiative Decay at All Exciton Densities", submitted, 2021)

semiconductors. By applying small mechanical strain, we shift the EEA process away from the VHS resonance and circumvent the enhanced nonradiative EEA that plagues the PL QY at high exciton densities, leading to near-unity PL QY at all exciton densities in 2D TMDC monolayers (e.g. MoS_2, WS_2, WSe_2). This simple, scalable method suppresses all nonradiative recombination at all generation rates for both exfoliated and CVD-grown centimeter-scale TMDC monolayers, as long as they are direct, and their Fermi level is in the middle of the bandgap by electrostatic or chemical doping. Our results constitute the first critical step towards optoelectronic devices that retain their high efficiency at high carrier concentrations and put forth TMDC monolayers as a key material of choice for next-generation optoelectronic applications.

3.2 Complete suppression of nonradiative recombination at all exciton densities

There are three central elements that steer the exciton recombination mechanism in TMDC monolayers: exciton generation rate, background carrier concentration, and electronic band structure. The combined effect of the first two factors has been studied thoroughly,[1] where the photocarrier generation rate (G) and background carrier concentration were tuned by varying the incident pump power and the gate voltage (V_g) in a capacitor structure, respectively. Due to pronounced Coulomb interaction, if background carriers are present, photogenerated excitons turn into charged trions[2] which mostly recombine nonradiatively.[1,3] In the absence of background carriers, at low exciton densities neutral excitons in intrinsic monolayers can recombine completely radiatively even in the presence of defects.[1,4] However, at high exciton densities recombination of neutral excitons is dominated by exciton−exciton annihilation (EEA), where an exciton nonradiatively recombines while colliding with another exciton.[4-6] EEA is present in all excitonic materials found in nature[7] and are the primary reason behind the efficiency roll-off observed in all organic[8] and some inorganic[9,10] light emitting devices. EEA has some similarities to Auger recombination which is commonly observed in conventional free-carrier systems and one of the prominent reasons behind efficiency roll-off observed in light-emitting diodes and solar cells.[11,12] Through the conservation of momentum and energy the participating quasiparticles, EEA depends on the aforementioned third factor: detailed band structure.[6,13,14] Here we modulate these three factors simultaneously. Along with gate voltage and pump power, we alter the electronic band structure by applying a uniaxial strain (ϵ). Surprisingly, we find that with appropriate strain all neutral excitons recombine radiatively even at high concentrations in monolayers of WS_2, WSe_2 and MoS_2, resulting in near-unity QY at all generation rates. As far as we know, this is unprecedented in any excitonic semiconductor observed in nature.[7] The density of states of electrons in a two-dimensional periodic crystal are topologically guaranteed to exhibit logarithmic van Hove singularities (VHSs) arising from saddle points in the energy dispersion.[15] When energy of a transition is close to the VHS, weak interactions are often intensified by the enhanced density of states (DOS).[16] From energy and momentum conservation, we show that as-exfoliated TMDC monolayers experience enhanced EEA as the final energy of this process coincides with inherent VHS. Strain drives the final energy away from VHS resonance and drastically reduces EEA in both sulfur- and selenide based TMDCs. Finally, to demonstrate the practical impact of these principles, we uniformly suppress all nonradiative recombination in a centimeter-scale CVD-grown WS_2 monolayer at all generation rates. This work establishes TMDCs as a practical material of choice for light emitting device applications free of efficiency roll-off for a wide range of excitation densities.

Monolayer MOS devices were fabricated on plastic flexible substrate enabling simultaneous modulation of carrier concentration and strain while performing quantitative PL QY measurements (device fabrication details are available in the supplementary materials). Fig. 1a shows the schematic and optical micrograph of such a device using WS_2 monolayers. Mechanically

exfoliated monolayers were transferred to a polyvinyl alcohol (PVA) layer attached to polyethylene terephthalate (PET) handling substrate, a combination selected for its superior strain transfer efficiency.[17] Subsequently, exfoliated hexagonal boron nitride (hBN; 70-100 nm in thickness) and graphene (2-5 nm in thickness) were transferred sequentially on the monolayer WS_2 to serve as a gate insulator and gate electrode, respectively. The WS_2 monolayer was electrically grounded and gate voltage (V_g) was applied to the top graphene. Bending the PET substrate with positive curvature applies tensile strain to the monolayer in the direction of bending.[18] As-exfoliated monolayer WS_2 is known to be electron-rich; application of a negative gate voltage of $V_g = -30\ V$ electrostatically compensates for that unintentional electron doping and ensures that the recombination process is dominated by neutral excitons.[1] At this biasing condition, we compare PL spectra of an unstrained and strained WS_2 monolayer at a high generation rate of $G = 6.5 \times 10^{19}\ cm^{-2}s^{-1}$ (Fig. 1b). We observe both a redshift of PL spectra and ~15 times enhancement in PL intensity with the application of $\epsilon = 0.4\%$ tensile strain at this high generation rate.

To better characterize this enhancement, calibrated PL measurements at room temperature were performed to quantitatively extract the QY as a function of ϵ, V_g and G (Fig. 1c-f). Fig. 1c shows PL QY as a function of the gate voltage, V_g and the generation rate, G when no strain is applied. At zero and positive gate voltages, background electron concentration of monolayer WS_2 is large, leading to formation of negative trions which predominantly recombine nonradiatively, thus yielding a low PL QY. At negative gate voltages the background electrons are removed, and recombination of neutral excitons dominate. At low generation rates, neutral excitons recombine completely radiatively despite native defect density. At high generation rates, PL QY rolls off due to EEA. These same results have also been observed in other substrates, such as PMMA and SiO_2 and are quantitatively same to the results here.[1] With the application of 0.2% tensile strain, the PL QY droop at the high exciton generation rate is notably reduced for negative V_g. (Fig. 1d). Once a tensile strain of 0.4% is applied, no PL QY droop at high generation rate is observed (Fig. 1e). Thus, all nonradiative recombination processes in as-exfoliated monolayer WS_2 have been suppressed by applying tensile strain and gate voltage. Suppression of EEA is further elucidated in Fig. 1f, where we show PL QY as a function of strain at $V_g = -30\ V$ and at a high generation rate $G = 6.5 \times 10^{19}\ cm^{-2}s^{-1}$. When no strain is applied, PL QY is low at this generation rate, however with the application of a threshold strain of 0.3% PL QY increases sharply and asymptotically approaches unity. This PL QY enhancement by strain is also reversible, as PL QY traces for increasing and decreasing strain fully overlap. High PL QY at all pumps persists even for a tensile strain of $\epsilon = 1.0\%$ (Fig 1f, Fig. S1). In addition to electrostatic counter-doping, high PL QY can be achieved by applying tensile strain in monolayer WS_2 chemically counter-doped by Nafion, a known hole-dopant (Fig. S2).

The PL QY for neutral excitons ($V_g = -30\ V$) can be written as the ratio of radiative recombination rate of to the total recombination rate

$$QY = \frac{R_r}{R_r + R_{nr}} \qquad (1)$$

where R_{r} and R_{nr} are the exciton radiative and nonradiative recombination rates, respectively. Nonradiative recombination for neutral excitons are predominantly through the EEA process.[1] Therefore, $R_{\mathrm{nr}} = R_{\mathrm{EEA}}$ where R_{EEA} is the nonradiative EEA rate. Since even with application of strain the semiconductor remains strongly excitonic,[6] strain does not change PL QY vs G behavior at low generation rates and R_{r} is independent of strain (Fig. 1d-f). On the other hand, since strain changes the QY at high pump, R_{EEA} must depend strongly on the strain. Using the experimentally measured PL QYs at a high generation rate of $G = 6.5 \times 10^{19}\ cm^{-2}s^{-1}$, we find that

$$\frac{R_{\mathrm{EEA}}(\epsilon = 0.4\%)}{R_{\mathrm{EEA}}(\epsilon = 0.0\%)} \approx 7 \times 10^{-3} \qquad (2)$$

which would indicate roughly two orders of magnitude decrease in EEA rate at the highest generation rate. Even though the EEA rate is not rigorously zero, it is decreased by the application of strain such $R_{\mathrm{r}} \gg R_{\mathrm{EEA}}$, and the radiative relaxation dominates the total recombination.

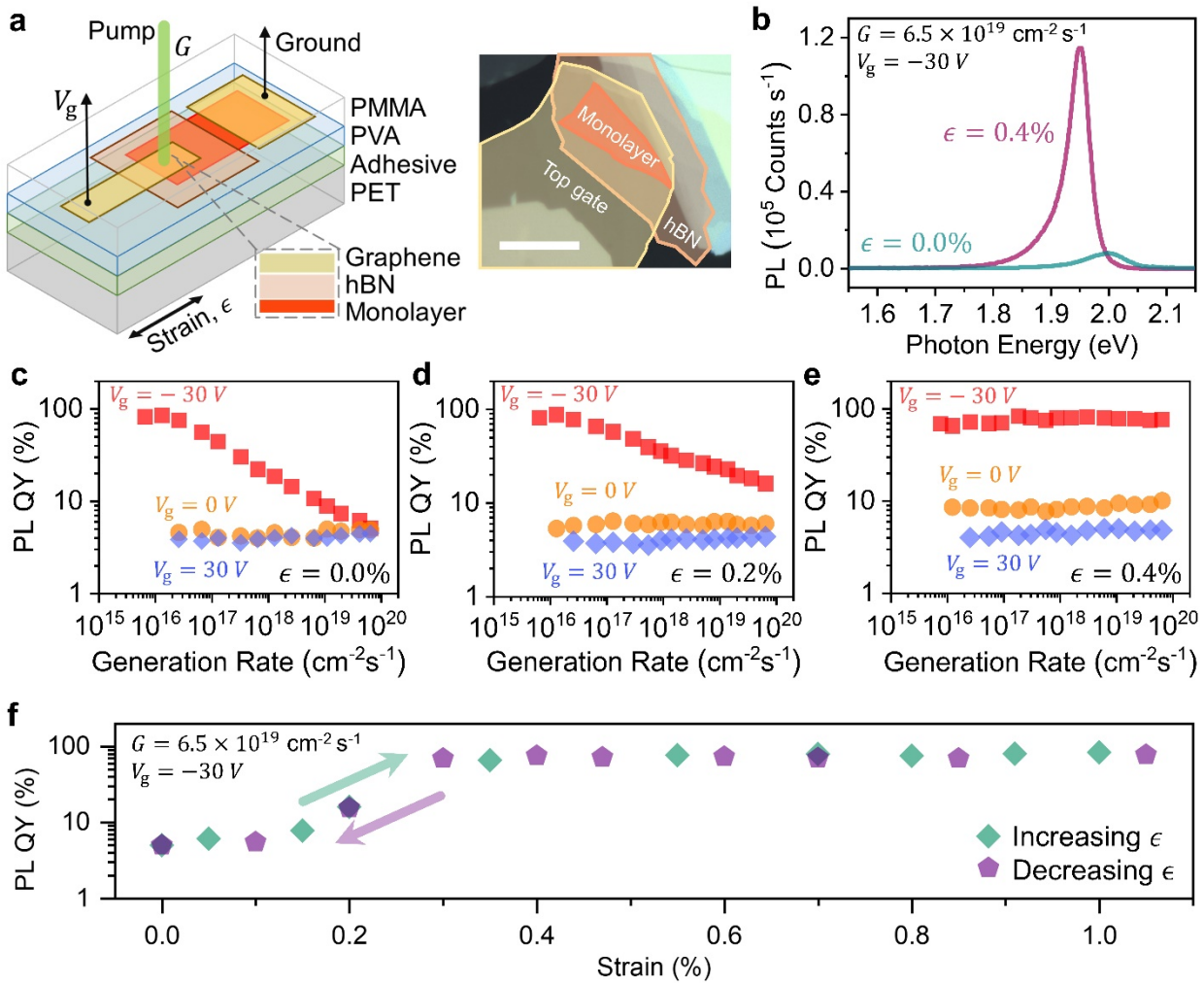

Fig. 1. a, Schematic and optical micrograph of the device structure, scale bar is 20 μm. A two-terminal MOS capacitor structure with graphene as source and gate, and hBN as insulator is fabricated on a flexible polymer substrate. **b,** Comparison of PL spectra of unstrained and 0.4% strained monolayer WS_2 at a high generation rate of $G = 6.5 \times 10^{19}$ cm^{-2}s^{-1} and a gate voltage of $V_g = -30\,V$. **c, d, e,** PL QY of monolayer WS_2 as a function of gate voltage, generation rate and strain. **f,** PL QY approaching unity with the application of strain at a high generation rate of $G = 6.5 \times 10^{19}$ cm^{-2}s^{-1}.

The rich photophysics of these monolayer semiconductors as a function of gate voltage and generation rate arises from the quasiparticle interaction and can be captured by a simple kinetic model described elsewhere.[1] Gate voltage can be used to tune the exciton to trion ratio, activating their respective recombination routes, whereas high density of neutral excitons activates the EEA process. However, suppression of EEA by strain has not been studied before and elucidating the

mechanism by which strain suppresses EEA at high pump necessitates a closer look at the EEA process itself. EEA occurs when one exciton ionizes another exciton by nonradiatively transferring its energy (Fig 2a).[6] The initial state consists of two excitons, with center-of-mass momenta $\boldsymbol{K_1}$ and $\boldsymbol{K_2}$ and energies E_1 and E_2, respectively. The exciton energy and momentum are related by [13]

$$E_1 = E_{\mathrm{G}} - E_{\mathrm{B}} + \frac{\hbar^2|\boldsymbol{K_1}|^2}{2M_{\mathrm{X}}} \qquad (3)$$

$$E_2 = E_{\mathrm{G}} - E_{\mathrm{B}} + \frac{\hbar^2|\boldsymbol{K_2}|^2}{2M_{\mathrm{X}}} \qquad (4).$$

In the above, E_G is the fundamental bandgap, E_B is the exciton binding energy and M_X is the exciton mass. The final state consists of a high energy electron and hole, with crystal momenta $\boldsymbol{k_e}$ and $\boldsymbol{k_h}$ and energies E_{e} and E_{h}, respectively. Irrespective of the details of the interaction potential, two quantities are conserved in the EEA process: total momentum and energy.[13,19,20] The condition for conservation of crystal momentum yields[13]

$$\boldsymbol{k_e} + \boldsymbol{k_h} = \boldsymbol{K_1} + \boldsymbol{K_2}. \qquad (5)$$

Since $\boldsymbol{K_1}$ and $\boldsymbol{K_2}$ are determined by the thermal motion of excitons they are negligible compared to $\boldsymbol{k_e}$ and $\boldsymbol{k_h}$, implying that the electron and the hole momentum in the final state should be almost opposite to each other.

$$\boldsymbol{k_e} \approx -\boldsymbol{k_h}, \qquad (6)$$

Therefore, momentum conservation dictates the electron and hole from the ionized exciton ends up with opposing crystal wavevectors (on top of each other in the energy dispersion, shown with the red dashed line in Fig 2a). The condition for conservation of crystal momentum yields[13]

$$E_{\mathrm{e}} + E_{\mathrm{h}} = E_1 + E_2. \qquad (7)$$

Since the exciton center of mass wavevector is negligible, $E_1 \approx E_2 \approx E_{\mathrm{G}} - E_{\mathrm{B}} = E_{\mathrm{X}}$, where E_{X} is the exciton transition energy. Therefore, energy conservation stipulates that the energy difference between the electron and hole must be $2E_{\mathrm{X}}$

$$E_{\mathrm{e}} + E_{\mathrm{h}} \approx 2E_{\mathrm{X}} \qquad (7)$$

If we denote the conduction and valance band of the semiconductor as E_{C} and E_{V}, then combined momentum and energy conservation can be written as

$$E_{\mathrm{e}} + E_{\mathrm{h}} = E_{\mathrm{C}}(\boldsymbol{k_e}) - E_{\mathrm{V}}(-\boldsymbol{k_h}) = E_{\mathrm{C}}(\boldsymbol{k_e}) - E_{\mathrm{V}}(\boldsymbol{k_e}) = 2E_{\mathrm{X}}. \qquad (8)$$

Therefore, any wavevector where the energy difference between the conduction and valance band is equal to twice the exciton transition energy can be the final wavevector of the electron from the ionized exciton (Fig. 2b). Note that, the exciton transition energy is different from the fundamental bandgap due to enhanced electron-hole interaction in TMDC monolayers. By Fermi's golden rule, the Joint density of states (JDOS) at twice the exciton transition energy determines the strength of

EEA process.[13,20]

Typically, effective mass approximation is invoked in literature to find out the energy of the ionized electron, however since the ionized electron and hole end up at a high energy, it is no longer a valid approximation. We first calculated the band structure of monolayer TMDC using an 11-band tight binding theory based on Wannier transformation of ab-initio density functional theory calculations (details of band structure are in ref.[21,22]). We then calculated energy difference between the conduction and valance band ($E_C - E_V$) for unstrained and strained monolayer WS_2, respectively. The first Brillouin zone is indicated by a gray hexagon (Fig. 2c and 2d). Red areas are the final states of the electron from the ionized exciton where the conservation laws are satisfied. We note that, possible final wavevectors in unstrained monolayer WS_2 include the saddle points Q (Fig. 2c); but in 0.4% strained WS_2 they do not include the saddle points (Fig. 2d). Saddle points in the band structure of a two dimensional semiconductor create VHS and result in a logarithmically diverging JDOS.[15,23,24] The JDOS for monolayer WS_2 $\rho_{\mathrm{CV}}(E)$ at $E = E_{\mathrm{C}} - E_{\mathrm{V}} = 2E_{\mathrm{X}}$ determines the strength of EEA. We show the JDOS of 0.4% strained and unstrained WS_2 in Fig 2e. In unstrained samples, there is a VHS at twice the exciton transition energy, resulting in an expedited EEA. Strain shifts the exciton transition energy E_{X} such that $2E_{\mathrm{X}}$ does not overlap VHS resonance, which reduces EEA rate.

We also show the JDOS of a 0.4% compressively strained WS_2 monolayer in Fig 2E. We note that compressive strain also drives the EEA process off VHS resonance by changing the exciton transition energy. This is also true for uniaxial strain applied in any direction or biaxial strain (Fig. S3, S4). The choice of tensile vs compressive strain to suppress all nonradiative recombination should ensure that the system remains direct bandgap with the application of strain to avoid nonradiative recombination through momentum-dark indirect excitons.[25] Compressive strain makes some TMDC monolayers such as WS_2 indirect. Note that, strain has also been used to reduce traditional Auger recombination in conventional 3D semiconductors, but the mechanism is different.[26] In 3D semiconductors, bandgap renormalization and effective mass equalization by applied strain can lead to one order of magnitude reduction of conventional Auger rate.[27] However, in the case of 2D TMDCs EEA is inhibited by shifting the exciton transition energy E_{X} such that $2E_{\mathrm{X}}$ does not overlap VHS resonance. Due to the existence of saddle points, logarithmic VHS always characteristically appears in two-dimensional semiconductors and are not found in three-dimensions, leading to a much stronger response to strain in monolayer TMDCs.[15]

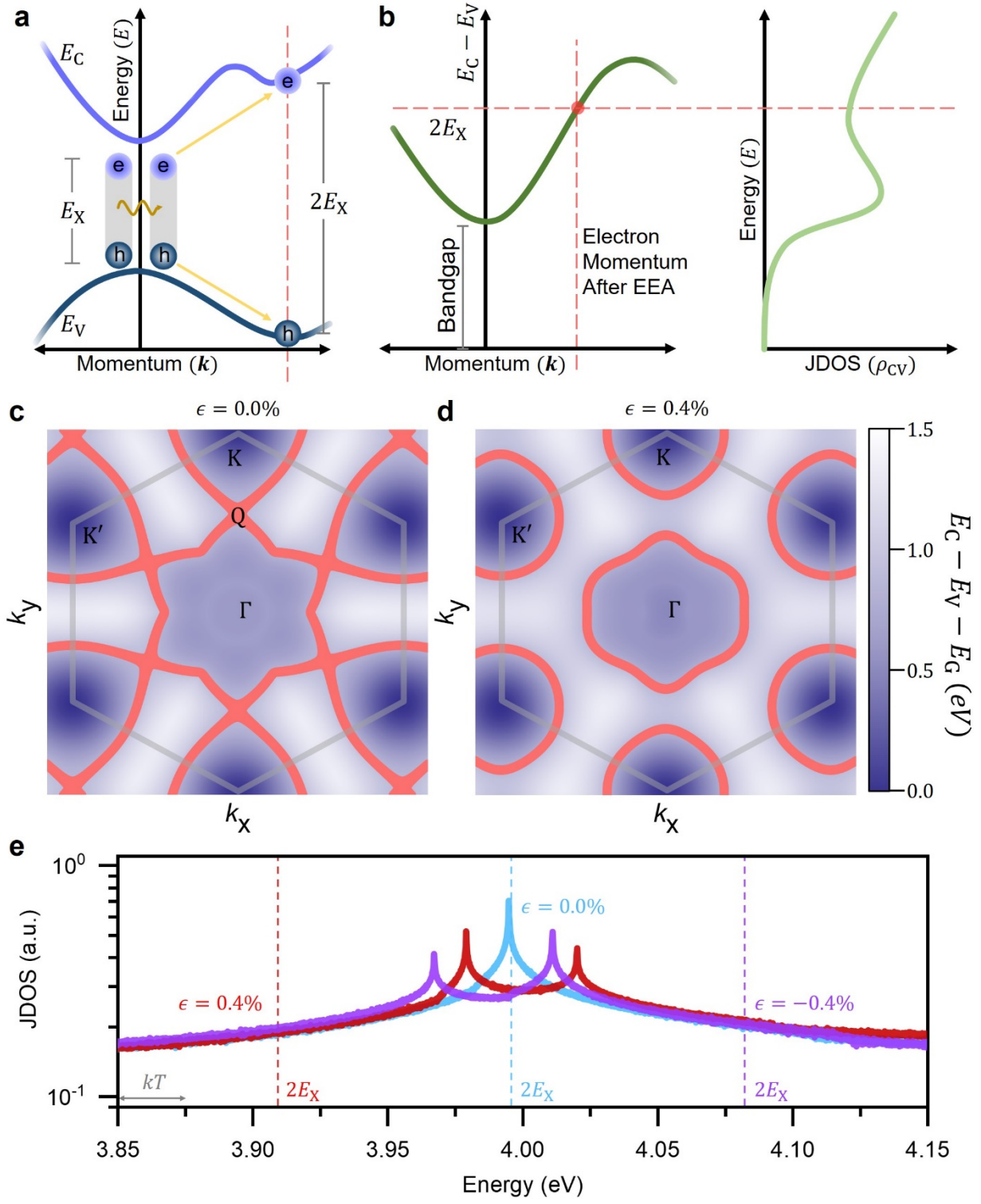

Fig. 2. a, Schematic describing microscopic mechanism of exciton-exciton annihilation (EEA).

EEA occurs when one exciton ionizes another exciton by nonradiatively transferring its energy. **b,** Momentum and energy conservation dictates that the electron from the ionized exciton ends up with a wavevector where the energy difference between the conduction and valance band is equal to twice the exciton transition energy. The Joint density of states (JDOS) at that energy determines the rate of EEA. **c, d,** Energy difference between the conduction and valance band for unstrained and 0.4% strained monolayer WS_2, respectively. Grey hexagon denotes the first Brillouin zone (each side is 19.946 nm^{-1}), whereas red areas are the possible final wavevectors. Possible final wavevectors in unstrained monolayer WS_2 include the saddle points Q, where there are VHSs; but strained samples do not. **e,** Calculated joint density of states (JDOS) for monolayer WS_2. JDOS $\rho_{CV}(E)$ at $E = E_C - E_V = 2E_X$ determines EEA rate. Dashed lines denote values of $2E_X$ at the corresponding strain.

These principles apply equally to other TMDC semiconductors. Like WS_2, exfoliated monolayer WSe_2 also exhibits near-unity PL QY at all generation rates when it is made intrinsic by electrostatic counterdoping and tensile strain is being applied (Fig. 3a, Fig S5). As-exfoliated monolayer MoS_2 has PL QY in the range of $0.1 - 1.0$ %, which drastically increases at low pump after chemical counterdoping by Nafion (Fig. 3b). Unlike WS_2 and WSe_2, monolayer MoS_2 becomes indirect when tensile strain is applied and remains direct when compressive strain is applied.[17] We found that, rather than compressively straining, downward bending of flexible substrate with negative curvature results in buckling of monolayer TMDC. Instead, we use the thermal coefficient of expansion mismatch between the glycol-modified Polyethylene terephthalate (PETG) substrate and MoS_2 to apply compressive strain. Chemically counterdoped, 0.5% compressively strained monolayer MoS_2 also exhibits roll-off fee PL QY at all generation rates. The universal, simple nature of these conditions for different TMDC monolayer semiconductors arises from their underlying excitonic photophysics.

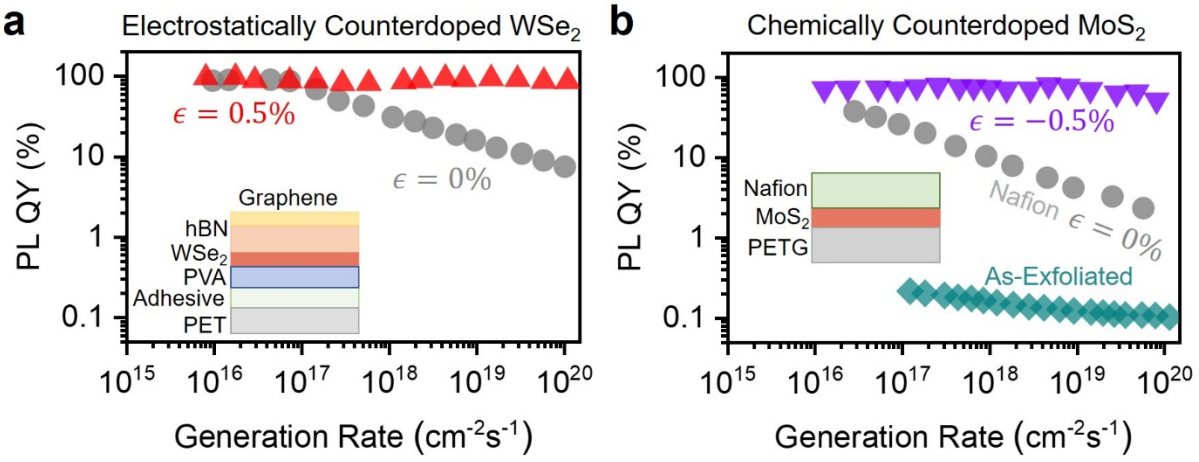

Fig. 3. a, b, Near-unity PL QY at all generation rates in electrostatically counterdoped WSe_2 and chemically counterdoped MoS_2 by tensile and compressive strain, respectively, demonstrates the universality of the conditions that suppress nonradiative recombination.

3.3 Large-scale monolayer semiconductors without exciton-exciton annihilation

Improving optoelectronic quality of large-area two-dimensional TMDCs poses one of the fundamental challenges for the development of the next-generation electronic and optical devices. The principles of suppressing all nonradiative recombination can also be applied to achieve high PL QY on centimeter-scale WS_2 monolayer grown by CVD. We first transfer a large-area CVD grown WS_2[28] on a flexible substrate and spin-coat it with Nafion (Fig. 4a). The normalized PL spectra redshifts with applied tensile strain (Fig 4b). Nafion counterdoping leads to a strain-independent PL QY of 70 ± 10 % (mean + standard deviation) at low pumps, which we see in a spatial map of the PL QY of a 2 mm $\times$ 2 cm area taken at a generation rate of $G = 10^{16}\ cm^{-2}s^{-1}$ (Fig. 4c). At a high generation rate of $G = 10^{20}\ cm^{-2}s^{-1}$ if no strain is applied, a low PL QY of 1.6 ± 0.8 % is observed uniformly, consistent with as-exfoliated monolayer WS_2. (Fig. 4d). However, at 0.4% applied tensile strain, PL QY of the same area reaches 59 ± 10 %, indicating a ~38 times uniform enhancement of PL QY for a large scale grown sample at a high generation rate of $G = 10^{20}\ cm^{-2}s^{-1}$. This demonstration showcases that ideal optoelectronic quality can be achieved in large-area grown monolayers by relatively simple and scalable application of counterdoping and strain.

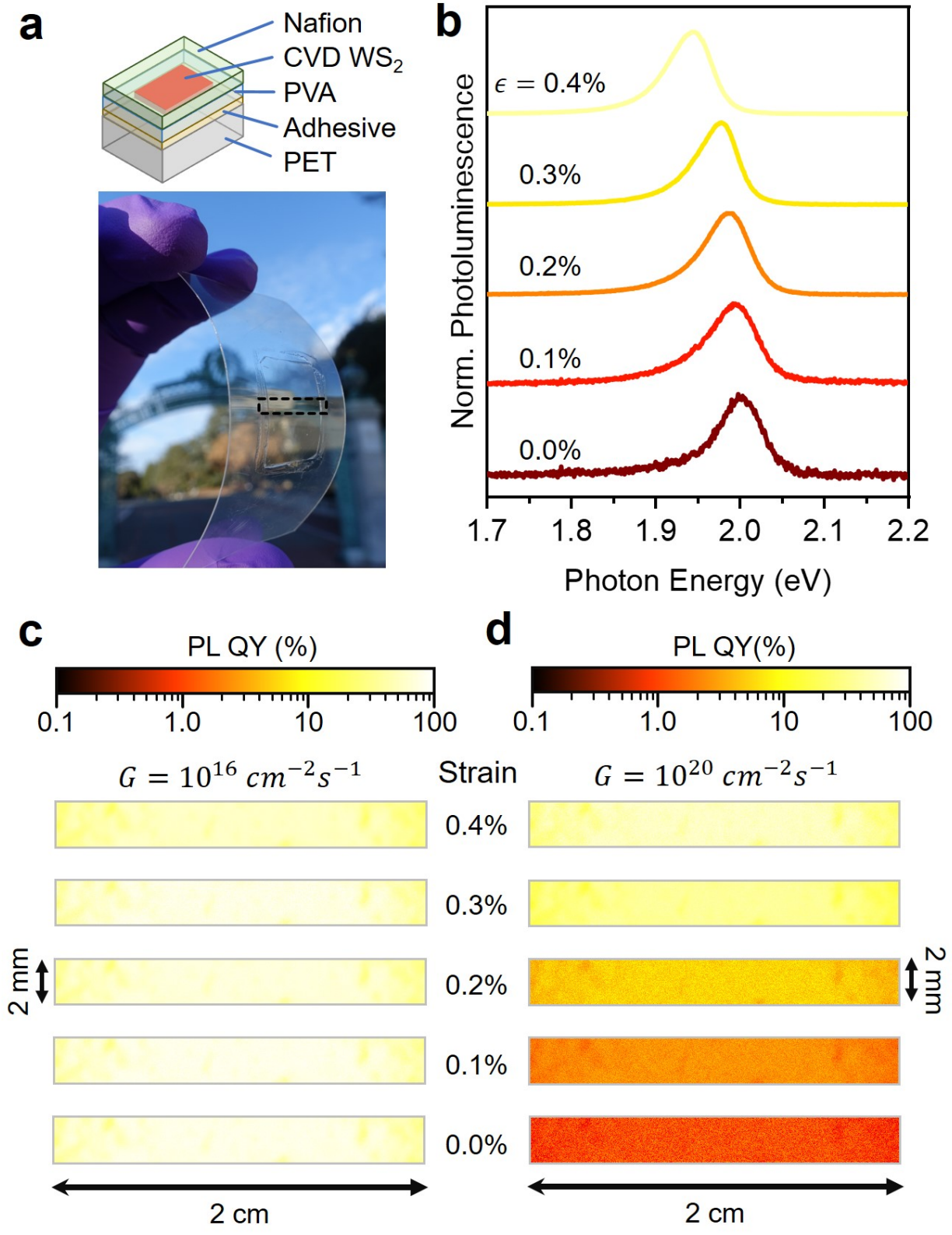
a
Nafion
CVD WS_2
PVA
Adhesive
PET
b
ϵ = 0.4%
0.3%
0.2%
0.1%
0.0%
Norm. Photoluminescence
1.7
1.8
1.9
2.0
2.1
2.2
Photon Energy (eV)
c
PL QY (%)
0.1
1.0
10
100
$G = 10^{16}\ cm^{-2}s^{-1}$
d
PL QY(%)
0.1
1.0
10
100
$G = 10^{20}\ cm^{-2}s^{-1}$
Strain
0.4%
0.3%
0.2%
0.1%
0.0%
2 mm
2 mm
2 cm
2 cm

Fig. 4. a, Schematic (top) and photograph (bottom) of the flexible substrate used to strain CVD grown, centimeter-scale WS_2. **b**, Normalized PL spectra of a typical spot at different strains. **c, d,** Spatial mapping of PL QY of a 2 mm × 2 cm area of grown WS_2 at a low generation rate of $G = 10^{16}\ cm^{-2}s^{-1}$ and a high generation rate of $G = 10^{20}\ cm^{-2}s^{-1}$, respectively, shows high PL QY is uniformly achieved by strain at the highest generation rate, while maintaining high PL QY at low pump.

Inorganic or organic, defective or unblemished, excitonic or free-carrier system, irrespective of which classification any semiconductor belongs to, nonradiative recombination has always been observed in all semiconductors at high photocarrier concentrations. Here we show that in both exfoliated and grown two dimensional semiconductors nonradiative recombination processes can be suppressed at all generation rates as long as the material is chemically intrinsic by electrostatic or chemical counterdoping, and EEA process is not in resonance with VHS as achieved by strain. Considering how common van Hove singularities are in low dimensional semiconductors these concepts in principle could apply to other systems. Our findings here present a strong case for the use of 2D materials for optoelectronic devices, although a number of challenges still need to be overcome in terms of the device design and implementation.

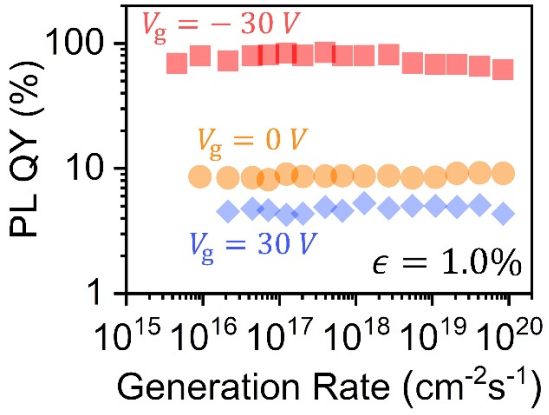

Fig. S1. PL QY of monolayer WS_2 as a function of gate voltage and generation rate at 1.0 % strain.

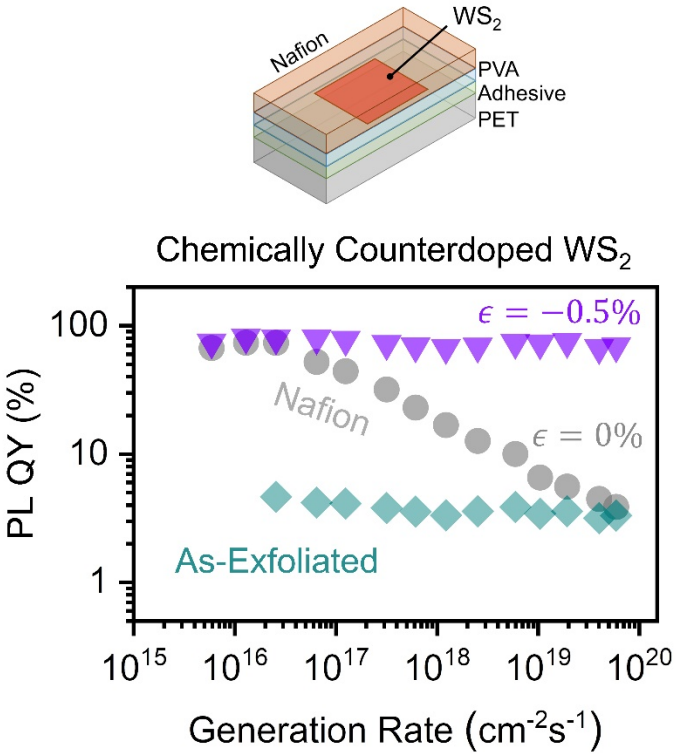

Fig. S2. PL QY of as-exfoliated and chemically counterdoped monolayer WS_2 as a function of strain.

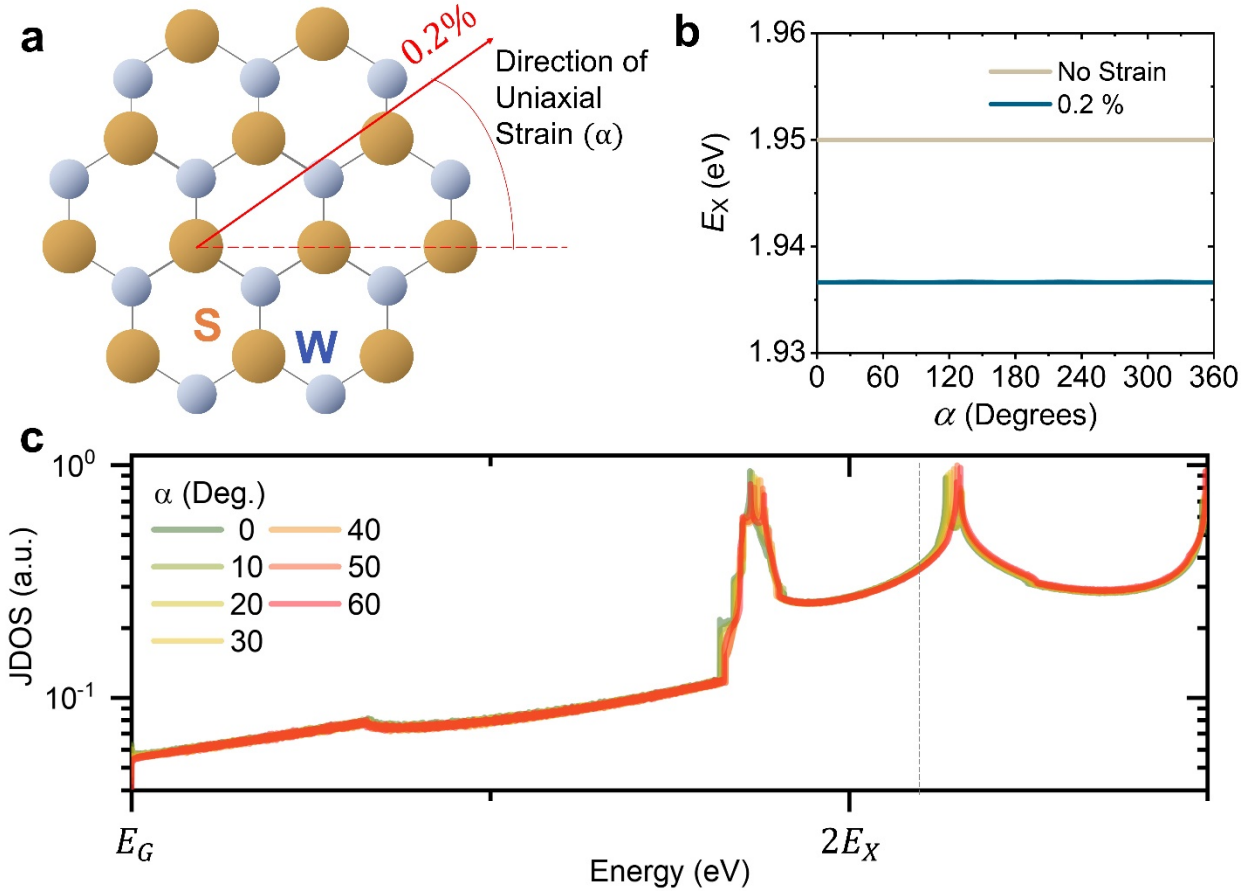

Fig. S3. a, Direction of uniaxial strain. **b,** Exciton transition energy as a function of strain direction. **c,** VHS is shifted from twice of exciton transition energy independent of tensile strain.

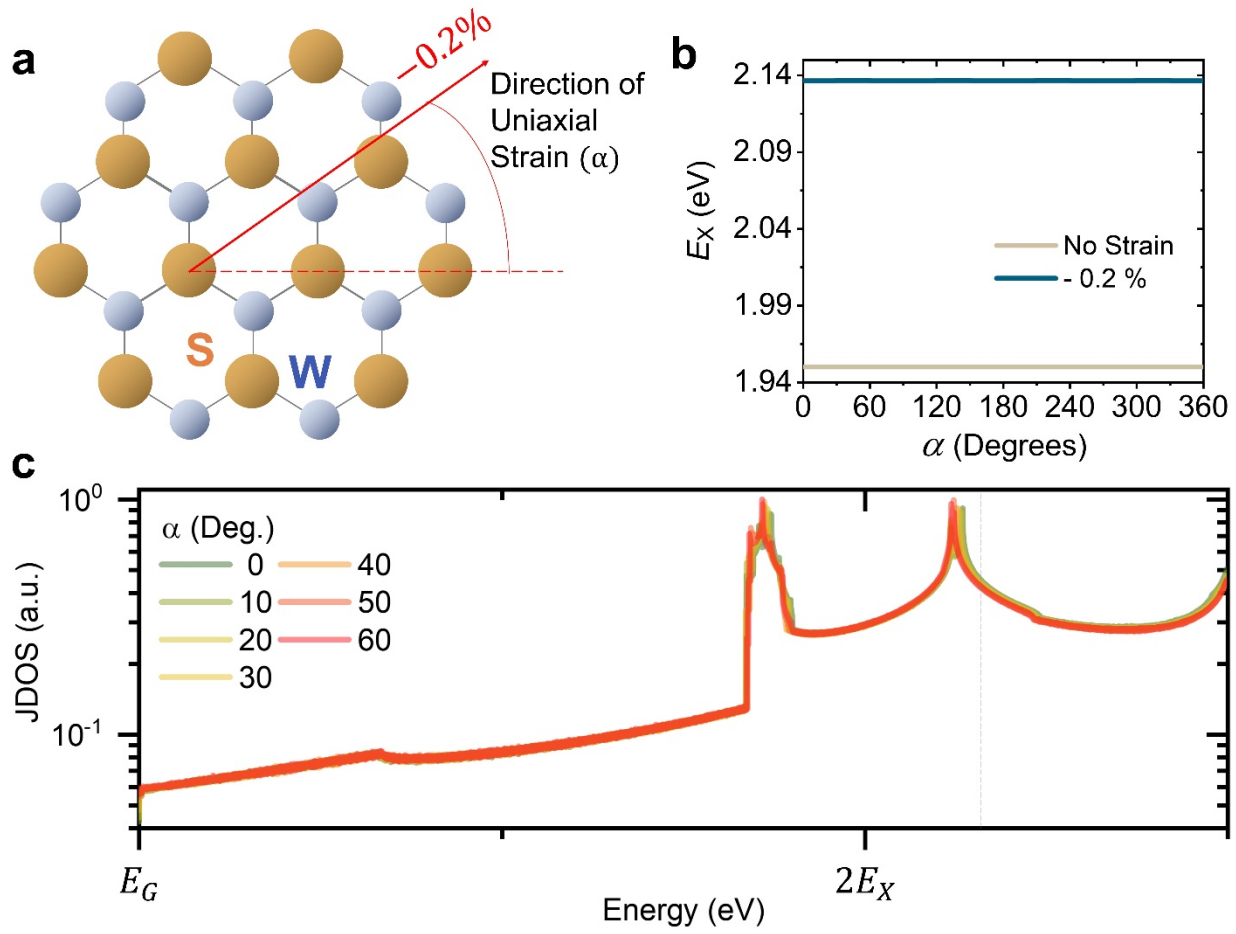

Fig. S4. a, Direction of uniaxial strain. **b,** Exciton transition energy as a function of strain direction. **c,** VHS is shifted from twice of exciton transition energy independent of compressive strain.

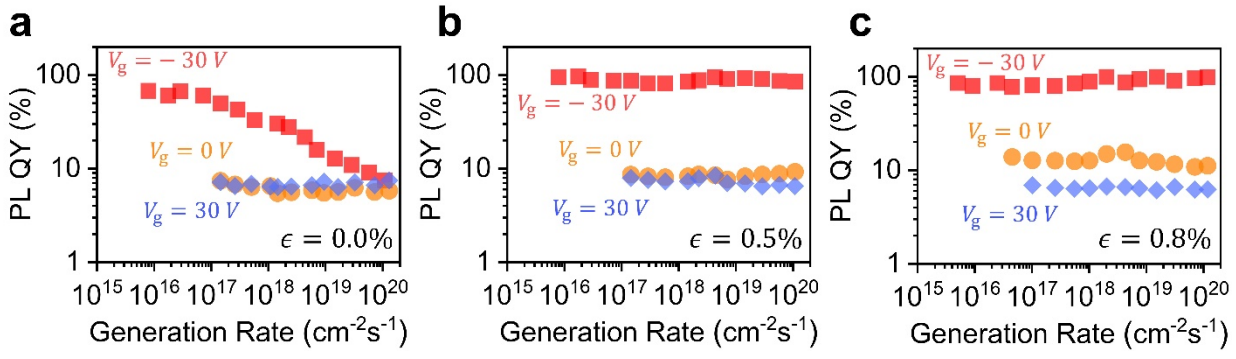

Fig. S5. a, **b, c,** PL QY of monolayer WSe_2 as a function of gate voltage, generation rate and strain.

Experimental and theoretical details

Device Fabrication

TMDC monolayers (WS_2 and WSe_2 from HQ Graphene, MoS_2 from SPI supplies) were mechanically exfoliated on top of 50 nm SiO_2/Si p^{++} substrates and were identified by optical contrast. 10 wt% polyvinyl alcohol (PVA, Alfa Aesar, 98–99% hydrolyzed, molecular weight 130,000 g/mol) solution were spin-coated at 1000 rpm for 40 seconds on the substrate with TMDC monolayer, and baked at 70 °C for 3 minutes to remove water solvent. Subsequently, a polyethylene terephthalate (PET, 125 μm thick) film is attached on top of the PVA film using adhesive (Super glue, Gorilla Glue Company) for ease of handling. Next, the entire flexible substrate (PVA/adhesive/PET) with the encapsulated monolayer TMDC is slowly peeled off from SiO_2 substrate using tweezer and resized so that the monolayer is at the center. Hexagonal boron-nitride (hBN, HQ Graphene) is mechanically exfoliated onto a 1×1 cm polydimethylsiloxane (PDMS) substrate. The flexible substrate is put on a sample stage under a modified optical microscope (bh2, Olympus) at room temperature and the hBN-exfoliated PDMS stamp was positioned upside down and aligned with the monolayer on the flexible substrate. The stamp was slowly brought into contact with the monolayer and peeled off rapidly, leading to transferred hBN on top of TMDC monolayer forming the insulator. In a similar fashion, Graphene (Graphenium, NGS Naturgraphit) is subsequently stamp-transferred on top of the TMDC monolayer/hBN stack to from source and top gate. Contacts are formed to the source and gate by applying silver conductive paste (EMS #12640, Electron Microscopy Sciences) to the graphene with a sharpened wooden tip under a Nikon stereomicroscope. Lastly, the device is encapsulated with PMMA (950 A11, Microchem) prior to measurement by dropcasting and subsequent soft-baking at 70 °C for 5 minutes.

To prepare compressively strained monolayer MoS_2, first MoS_2 was exfoliated on PDMS and then stamp was slowly brought into contact with the center of a piece of glycol-modified Polyethylene terephthalate (PETG, 2.54 mm thick, 3 cm length) at 90° C and peeled off, followed by rapid quenching of the MoS_2-transferred PETG down to room temperature. After the transfer, 3% Nafion perfluorinated resin solution (5 wt % in lower aliphatic alcohols and water, contains 15−20% water, Sigma Aldrich) diluted by ethanol was spin coated at 4000 rpm on the prepared MoS_2 sample with biaxial compressive strain.

Electrical and Optical Characterization

Devices were charged from an Keithley 2410 Source Meter Unit connected to the gate electrode,

while the graphene source contact was grounded. The PL QY was measured using a customized micro-PL instrument described in detail in previous study[1]. An Ar ion laser with a 514.5 nm line was used as the excitation source. All measurements reported in this paper are taken at room temperature, in an ambient lab conditions under nitrogen flow. The applied strain on the flexible substrate were calculated using the equation $\varepsilon = t / R$, where $2t$ and R are the substrate thickness and curvature radius. The thickness $2t$ of the entire flexible substrate is measured through the cross-section optical image. The curvature radius R were measured through the side-view photograph. All theory calculations are carried out in MATLAB.

References

1 Lien, D.-H. *et al.* Electrical suppression of all nonradiative recombination pathways in monolayer semiconductors. *Science* **364**, 468 (2019).

2 Ross, J. S. *et al.* Electrical control of neutral and charged excitons in a monolayer semiconductor. *Nature Communications* **4**, 1474 (2013).

3 Withers, F. *et al.* Light-emitting diodes by band-structure engineering in van der Waals heterostructures. *Nature Materials* **14**, 301-306 (2015).

4 Amani, M. *et al.* Near-unity photoluminescence quantum yield in MoS2. *Science* **350**, 1065 (2015).

5 Yu, Y. *et al.* Fundamental limits of exciton-exciton annihilation for light emission in transition metal dichalcogenide monolayers. *Physical Review B* **93**, 201111 (2016).

6 Wang, F., Wu, Y., Hybertsen, M. S. & Heinz, T. F. Auger recombination of excitons in one-dimensional systems. *Physical Review B* **73**, 245424 (2006).

7 Uddin, S. Z., Rabani, E. & Javey, A. Universal Inverse Scaling of Exciton–Exciton Annihilation Coefficient with Exciton Lifetime. *Nano Letters* **21**, 424-429 (2021).

8 Murawski, C., Leo, K. & Gather, M. C. Efficiency Roll-Off in Organic Light-Emitting Diodes. *Advanced Materials* **25**, 6801-6827 (2013).

9 Zou, W. *et al.* Minimising efficiency roll-off in high-brightness perovskite light-emitting diodes. *Nature Communications* **9**, 608 (2018).

10 Bae, W. K. *et al.* Controlling the influence of Auger recombination on the performance of quantum-dot light-emitting diodes. *Nature Communications* **4**, 2661 (2013).

11 Iveland, J., Martinelli, L., Peretti, J., Speck, J. S. & Weisbuch, C. Direct Measurement of Auger Electrons Emitted from a Semiconductor Light-Emitting Diode under Electrical Injection: Identification of the Dominant Mechanism for Efficiency Droop. *Physical Review Letters* **110**, 177406 (2013).

12 Green, M. A. Limits on the open-circuit voltage and efficiency of silicon solar cells imposed by intrinsic Auger processes. *IEEE Transactions on Electron Devices* **31**, 671-678 (1984).

13 Kavoulakis, G. M. & Baym, G. Auger decay of degenerate and Bose-condensed excitons in Cu2O. *Physical Review B* **54**, 16625-16636 (1996).

14 Aslan, O. B., Deng, M. & Heinz, T. F. Strain tuning of excitons in monolayer WSe2. *Physical Review B* **98**, 115308 (2018).

15 Van Hove, L. The Occurrence of Singularities in the Elastic Frequency Distribution of a Crystal. *Physical Review* **89**, 1189-1193 (1953).

16 Hirsch, J. E. & Scalapino, D. J. Enhanced Superconductivity in Quasi Two-Dimensional Systems. *Physical Review Letters* **56**, 2732-2735 (1986).

17 Li, Z. *et al.* Efficient strain modulation of 2D materials via polymer encapsulation. *Nature Communications* **11**, 1151 (2020).

18 Desai, S. B. *et al.* Strain-Induced Indirect to Direct Bandgap Transition in Multilayer WSe2. *Nano Letters* **14**, 4592-4597 (2014).

19 Landsberg, P. T. *Recombination in semiconductors*. (Cambridge University Press, 2003).

20 Abakumov, V. N., Perel, V. I. & Yassievich, I. N. *Nonradiative recombination in semiconductors*. (Elsevier, 1991).
21 Fang, S., Carr, S., Cazalilla, M. A. & Kaxiras, E. Electronic structure theory of strained two-dimensional materials with hexagonal symmetry. *Physical Review B* **98**, 075106 (2018).
22 Fang, S. *et al.* Ab initio tight-binding Hamiltonian for transition metal dichalcogenides. *Physical Review B* **92**, 205108 (2015).
23 Bassani, F., Parravicini, G. P., Ballinger, R. A. & Birman, J. L. Electronic States and Optical Transitions in Solids. *Physics Today* **29**, 58-59 (1976).
24 Cardona, M. & Peter, Y. Y. *Fundamentals of semiconductors*. (Springer, 2005).
25 Madéo, J. *et al.* Directly visualizing the momentum-forbidden dark excitons and their dynamics in atomically thin semiconductors. *Science* **370**, 1199 (2020).
26 Silver, M., Reilly, E. P. O. & Adams, A. R. Determination of the wavelength dependence of Auger recombination in long-wavelength quantum-well semiconductor lasers using hydrostatic pressure. *IEEE Journal of Quantum Electronics* **33**, 1557-1566 (1997).
27 Haug, A. Auger recombination in direct-gap semiconductors: band-structure effects. *Journal of Physics C: Solid State Physics* **16**, 4159 (1983).
28 Cho, J. *et al.* Centimeter-Scale and Visible Wavelength Monolayer Light-Emitting Devices. *Advanced Functional Materials* **30**, 1907941 (2020).

4

Actively Variable Spectrum Infrared Optoelectronics[*]

4.1 Introduction

Room-temperature optoelectronic devices that operate at shortwave and midwave infrared wavelengths (1-8 μm) can be used for numerous applications[1-5]. To achieve the operating wavelength range needed for a given application, a combination of materials with different bandgaps (e.g. superlattice/heterostructure)[6,7] or the variation of semiconductor alloy composition during growth[8,9] is used; however, these approaches involve fabrication complexity and the operating range is fixed post-fabrication. Although wide-range, active, and reversible tunability of the operating wavelengths in optoelectronic devices after fabrication is a highly desirable feature, no such platform has been yet developed. Here, we demonstrate high-performance room-temperature infrared optoelectronics with actively variable spectra by presenting black phosphorus (bP) as an ideal candidate. Enabled by the extraordinary sensitivity of its bandgap to strain, which varies from 0.22 to 0.53 eV, we show the continuous and reversible tuning of the operating wavelengths in bP light-emitting diodes and photodetectors. Furthermore, we leverage this platform to demonstrate multiplexed non-dispersive infrared gas sensing where multiple gases (e.g. CO_2, CH_4, and H_2O) are detected using a single light source. With its active spectral tunability

[*] The following section has been submitted for journal publication in a similar form. (H. Kim, S. Z. Uddin, D.-H. Lien, M. Yeh, N. S. Azar, S. Balendhran, T. Kim, N. Gupta, Y. Rho, C. P. Grigoropoulos, K. B. Crozier, A. Javey, "Actively Variable Spectrum Optoelectronics with Black Phosphorus", submitted, 2021)

while retaining high performance, our work bridges a technological gap, presenting a potential route to meet different emission/detection spectrum requirements in various optoelectronic applications.

The spectral range over which an optoelectronic device can operate is largely dictated by the bandgap of its photoactive material. To achieve the operating range needed for a given application, materials with varying compositions (i.e. by alloying to tune the bandgap) or complex structures consisting of materials with different bandgaps (e.g. superlattices or heterostructure) are used[10,11]. While effective, these come with increased fabrication complexity as they involve the precise control of material thickness and/or composition. In addition, these approaches produce devices whose operating wavelength ranges are fixed post fabrication. Although the absorption edge can be shifted by applying an electric field for Franz-Keldysh effect or Stark effect[12,13], the decrease in photoresponse and luminescence intensity at the extended spectral range as well as the requirement for additional gate electrodes to apply the bias field is a major bottleneck for developing tunable optoelectronics with high performance.

Strain is an effective knob to modulate the electronic and optical properties of semiconductors[14-16], which can achieve reversible and controllable tuning of the bandgap in semiconductors. Whereas only a limited amount of strain can be epitaxially applied in bulk crystalline materials, 2D materials can sustain much larger elastic strain, thus allowing for wide tuning of their optical bandgap[17,18]. Due to its puckered lattice structure, bP specifically has shown unique strain-dependent properties, including bandgap which is highly sensitive to strain[19-22], anomalous strain dependence of the bandgap[23], tunable van der Waals interaction[24], and piezoelectricity[25]. Strain can be applied in a reversible manner in bP due to its membrane nature which does not require a selective thinning and lift-off process[26,27]. The bandgap of multilayer bP also spans the portion of the IR region in which there is a rapidly increasing demand for optical communications, thermal imaging, health monitoring, spectroscopy, and gas sensing[28]. Moreover, the low Auger recombination velocity[29,30] and direct bandgap of bP at all thicknesses are advantageous for high-efficiency optoelectronic applications. However, despite considerable interest in developing actively tunable IR optoelectronic devices, no significant progress has been made in that direction.

In this study, we utilize the strain-tunable bandgap of bP for the demonstration of actively variable spectrum optoelectronic (AVSO) devices that operate in the infrared regime at room temperature. Covering from 2.3 μm to 5.5 μm, the bP bandgap exhibits a modulation rate of 1.70 μm/% by strain using our methods, which is the highest value reported for direct bandgap semiconductors. This enables wide range modulation of their spectral range in both light-emitting and detecting devices at will without sacrificing their performance. Continuous and reversible tuning of MWIR electroluminescence (EL) is demonstrated using bP-MoS_2 heterostructure on a flexible substrate. The detection range of highly-responsive bP photodetectors is additionally extended by applied strain. Finally, we detect multiple gases (e.g. CO_2, CH_4, and H_2O) using a single tunable IR light source. Owing to its reversibility and capacity for active spectral tunability while retaining high performance, our approach provides versatility in various fields where a tunable spectrum is required at room temperature.

Strain-tunable bandgap in bP. BP has a puckered hexagonal structure with two crystal orientations

in each layer: armchair (AC, *x*) and zigzag (ZZ, *y*) (Fig. 1a). The strain-induced actively variable bandgap of bP enables AVSO devices at room temperature that exhibit wide and reversible operating wavelength tunability (Fig. 1b). Mechanically exfoliated bP was transferred onto a pre-annealed polyethylene terephthalate glycol-modified (PETG) substrate at 95 °C (Fig. 1c). The rapid thermal quenching of the bP/PETG sample to room temperature resulted in the application of compressive strain to bP due to the coefficient of thermal expansion (CTE) mismatch between bP and PETG (Methods). Thereafter, the sample was bent to apply tensile strain. Here, we quantify the strain *via* its ZZ (*y*) direction component (Fig. S1a,b). Therefore, the strain in bP in this work is determined by the sum of the compressive (negative) strain in ZZ (*y*) direction induced by thermal expansion mismatch and tensile (positive) strain in ZZ (*y*) direction from bending stress. The strain-induced bandgap shift in bP was verified by IR photoluminescence (PL) spectroscopy (Fig. 1d). Before bending, the PL peaked at a wavelength of 5.5 μm (0.66 %, compressive). A large spectral blueshift of 3.2 μm was observed after mechanical bending (1.21 %, tensile), corresponding to a bandgap shift from 0.22 eV to 0.53 eV by applied strain. At 0 % strain, the PL had a peak position at 0.35 eV, which is in good agreement with the PL spectrum of unstrained bP from the literature[31]. Raman studies showed that the shifting rates with the applied strain were consistent with previous reports[25,32] (Fig. S1c-e). In addition, we found that built-in compressive strain plays a major role in preventing any partial relaxation or slippage during bending, retaining up to 1.21 % of tensile strain (Fig. 2a). Owing to the effective transfer of mechanical strain and extraordinary sensitivity of its bandgap to strain, our method offers a significantly broad and continuous bandgap tuning range at room temperature. The wavelength range spanned by our approach is from the short-wavelength infrared (SWIR) to the MWIR and could only be accessed otherwise by multiple devices comprising bulk semiconductor alloys with different compositions.

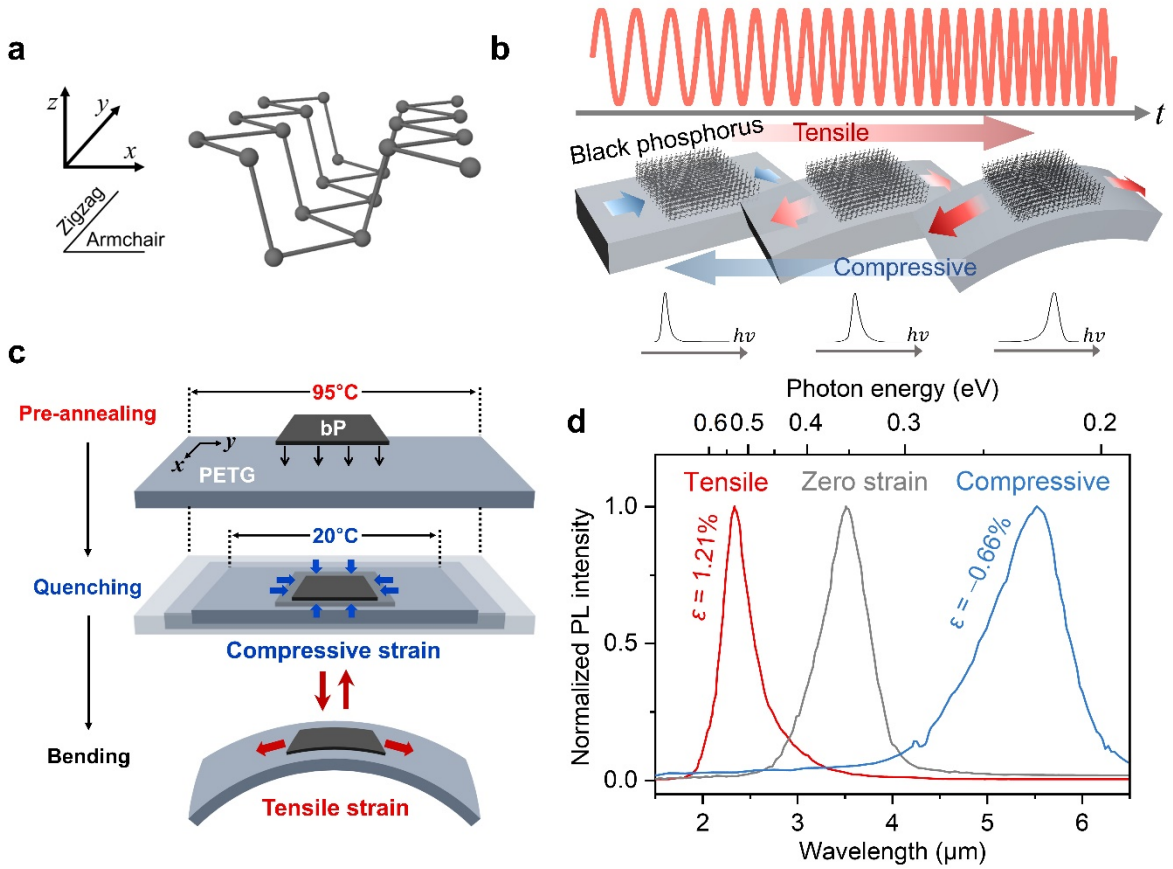

Fig. 1. a, Schematic illustrating the anisotropic crystal structure of bP along the armchair (AC) and zigzag (ZZ) directions. **b**, Schematic representation of actively tunable bandgap of bP using strain. Compressive and tensile strains induce redshift and blueshift of the bP bandgap, respectively. **c**, Schematic diagram illustrating strain application in bP. Compressive strain is applied by thermal expansion mismatch between bP and the substrate and tensile strain is applied by mechanical bending of the substrate. **d**, Normalized PL spectra of as-exfoliated bP, and bP under compressive strain (0.66 % along ZZ) and bP under tensile strain (1.21 % along ZZ). BP thickness is 20 nm, and the excitation light is polarized in the AC direction at an incident power of 22.5 W/cm^2 (there is no laser-induced thermal effect on the strain conditions of bP). Tensile strain is applied in the ZZ direction of the bP.

Detailed optical characterization was performed using IRPL spectroscopy to further investigate bandgap tunability in bP using strain. As the strain increased, the PL intensity increased and the wavelength of the spectral peak varied continuously from 5.5 μm to 2.3 μm (Fig. 2a). The blueshift rate of the bP bandgap by strain was found to be 1.70 μm/% (162 meV/%), which is substantially higher than other semiconductors with similar bandgaps (e.g. Ge and InAs) (Fig. 2b and Table S1). Changing the direction of tensile strain with respect to the crystal orientation of bP (AC and ZZ) did not have a large effect on the magnitude of the bandgap shift (Fig. S2c),

which agrees with previous work[22]. Additionally, light absorption at the PL excitation wavelength showed little dependence on strain (Fig. S2d). The relative PL QY in bP under different strains is thus given by the integrated luminous intensity divided by the incident power as well as light absorption (Fig. 2c). Strained bP exhibited a continuous PL QY increase in the high pump regime whereas in unstrained bP the QY remained constant. Because our incident power range is less than two orders of magnitude, which is limited by the measurement setup, it is not sufficient to extract recombination coefficients by fitting the incidence power-dependent data we have. This introduces uncertainty in determining which of parameters (Shockley-Read-Hall (SRH), radiative, or Auger) are affected by strain, with respect to carrier densities. The PL QY in bP under tensile strain (1.21 %) is higher than that in bP under compressive strain (0.66 %) and unstrained bP. These results can be attributed to the change in effective mass by strain. Namely, the uniaxial tensile strain strongly alters the effective mass, with a blueshift of the bandgap and an increase in the radiative recombination rate. As high current density operation is required in light-emitting devices, this property makes bP under tensile strain a suitable material for high-efficiency infrared light emitting devices.

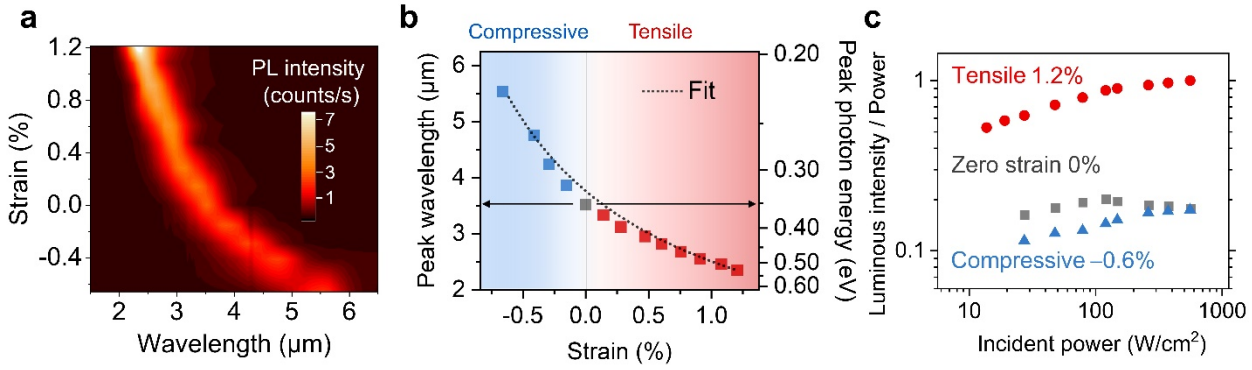

Fig. 2. a, PL spectra of bP as a function of strain along the ZZ (*y*) direction. **b**, Strain-dependent PL spectral peak shift in bP. The fit indicates that the peak modulation rate is 1.70 μm wavelength shift per percent of strain, covering from 5.5 to 2.3 μm. Laser-induced thermal effects on strain are precluded by using low excitation power, where the PL spectral peak is constant with increasing laser power density (Fig. S2b). **c**, Integrated PL intensity normalized by incident power as a function of power density for bP under different strain conditions. Note that bP thickness is 20 nm in the above measurements. We also demonstrated reversible and repeatable bandgap tuning, which indicates that there is no mechanical slip between bP and the substrate over multiple cycles (Fig. S2e).

4.2 Actively variable spectrum infrared light-emitting diodes

Recently, an electrically-pumped emission from bP shows great promises as a light source at MWIR wavelengths[33-35], due to its direct bandgap even in bulk limit and its low Auger recombination velocity[29,30]. By leveraging the property of bP whose bandgap can be widely modulated by strain, we developed strain-tunable LEDs based on bP/MoS_2 heterojunctions (Fig. 3a,b), where tensile strain is applied *via* bending along the ZZ (*y*) orientation of bP (Fig. 3c). Here, MoS_2 was used as an electron selective contact. Polyimide is used as the substrate to fabricate LEDs because PETG is not able to withstand conventional lithography processes (Methods). As strain was varied from compressive to tensile, the peak in EL spectrum continuously shifted from 4.07 μm (0.20 %, compressive) to 2.70 μm (1.06 %, tensile) (Fig. 3d). Similar to the trend observed in our PL results, the EL intensity also increased with tensile strain as the emission wavelength became shorter. The EL peak wavelength as a function of the current density was characterized for different current densities (Fig. S3a). The angular intensity distributions of the bP-LED were also simulated at two emission wavelengths (4.07 μm and 2.70 μm), which were found to be similar (Fig. S3b,c). We observed that, at all current densities, the bP-LED under tensile strain showed higher EL intensity than when in compressive strain (Fig. 3e). The EL enhancement with tensile strain was due to the resultant PL QY enhancement, as the injection efficiency did not improve with strain (Fig. S3d). The light emission from bP-LED was highly polarized, which is consistent with previous reports[33-35] (Fig. 3e, inset). Our bP-LED also shows stable emission wavelength tunability above room temperature (20 °C < *T* < 100 °C) (Fig. S4). However, the emission intensity decreases with increasing temperature, which can be attributed to the thermal activation of the nonradiative recombination centers at high temperature[31]. We extracted the internal quantum efficiency (IQE) of our bP-LED, which is plotted along with the theoretical PL QY of InAs, PbSe, GaSb, and bP as a function of carrier concentration (Fig. 3f). Our device showed a peak IQE of 0.73 % (0.2 %, compressive) and 2.47 % (1.0 %, tensile) at room temperature. A detailed discussion of measuring output power to calculate the IQE of the bP-LED is provided in Methods. For the case of a semiconductor with low background doping (i.e. $n = p$), the theoretical PL QY is calculated according to a standard *ABC* recombination model as:

$$\mathrm{QY} = \frac{B(n^2 - n_i^2)}{\frac{A(n^2 - n_i^2)}{n} + B(n^2 - n_i^2) + 2Cn(n^2 - n_i^2)} \tag{2}$$

where n_i is the intrinsic carrier concentration and *A*, *B*, and *C* are the SRH, radiative, and Auger recombination coefficient, respectively. The parameters for InAs, PbSe, GaSb, and bP used to calculate QY are summarized in Table S2. Since the SRH recombination coefficient is an extrinsic parameter and highly dependent on material quality, it was assumed to be zero for this analysis.

For small bandgap semiconductors, the Auger recombination is likely to be pronounced and a limiting factor for performance of LED. This originates from the relationship between the ratio of the Auger lifetime (τ_a) to the radiative lifetime (τ_r) and the bandgap (E_g) which is given by:

$$\frac{\tau_a}{\tau_r} \propto \exp\left[\left(\frac{\frac{m_e^*}{m_h^*}}{1+\frac{m_e^*}{m_h^*}}\right)\left(\frac{E_g}{k_B T}\right)\right] \tag{3}$$

where m_e^* and m_h^* are the effective masses of electrons and holes, respectively, k_B is Boltzmann's constant, and T is temperature[36,37]. Since m_e^* and m_h^* in bP have similar values, the effective mass ratio (m_e^*/m_h^*) is much higher than that of other small bandgap semiconductors. According to equation (3), this results in suppressed Auger recombination (longer Auger lifetime), which leads to bP's theoretical QY limit being much higher than that of other small bandgap semiconductors in the high injection regime.

We characterized the cyclic repeatability and stability of emission tuning in our bP-LED, exhibiting reversible and stable emission tuning over 500 bending cycles during ~6 hours of operation (Fig. 3g,h). A light source capable of active and continuous tuning of its operating wavelength within this spectral region is of particular significance, as this wavelength range consists of various wavelength bands essential for gas detection and chemical analysis. Our strain-tunable bP-LED not only provides wide tuning capability that is equivalent to the integration of numerous devices made from bP with a thickness range of 7–200 nm, but also enhances the performance of MWIR light-emitting devices by applied strains. Furthermore, the low operating power of our bP-LEDs and their potential for monolithic integration with silicon technology[35] would be advantageous for numerous applications.

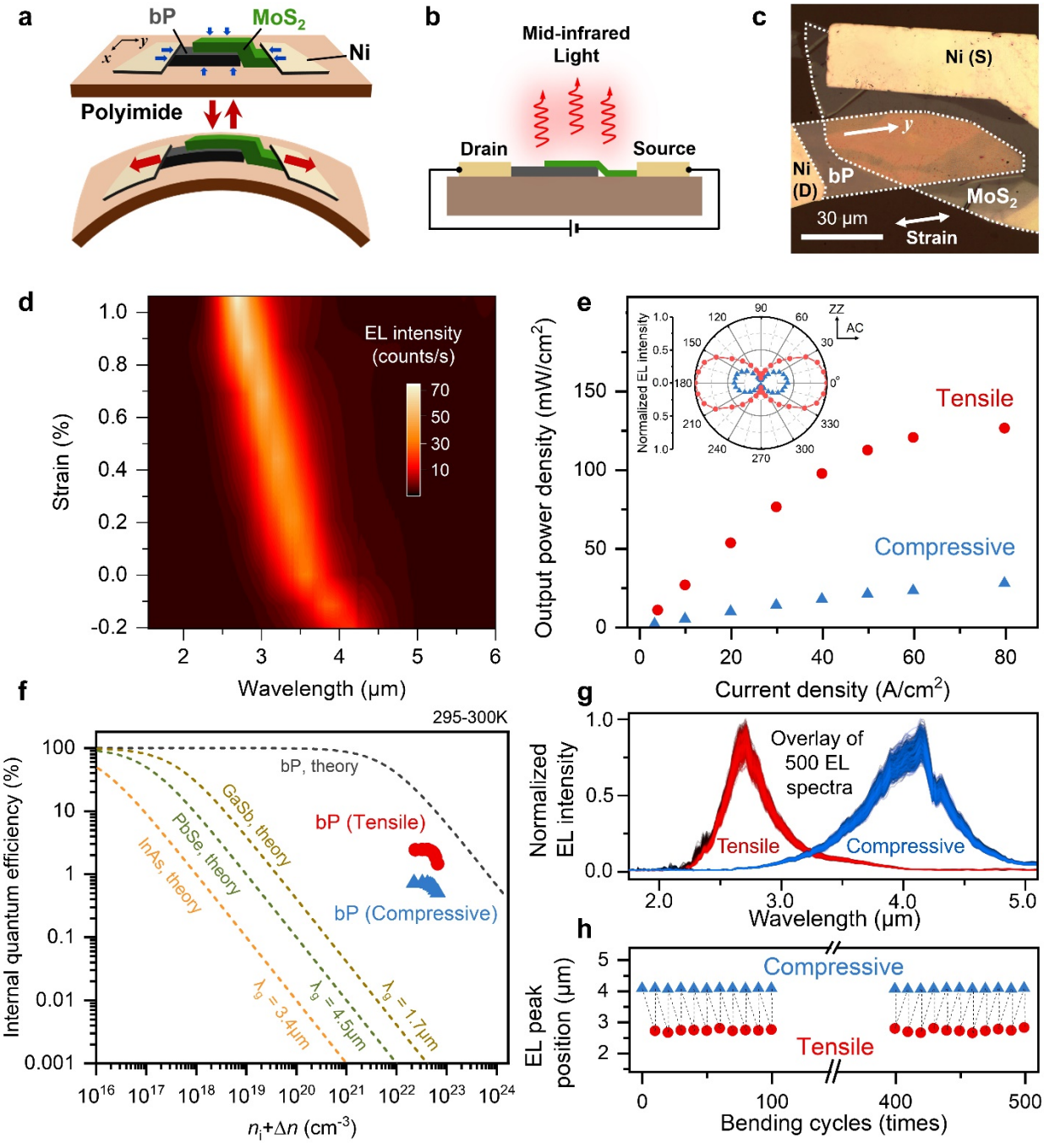

Fig. 3. a, Schematic of a strain-tunable bP/MoS_2 LED. **b**, Schematic of the device architecture, showing MWIR electroluminescence under forward bias across the bP/MoS_2 heterojunction. **c**, Optical micrograph of a representative device. **d**, Strain-dependent EL spectra. **e**, Light-current characteristics under 0.20 % compressive and 1.06 % of tensile strain. Inset: integrated EL intensity as a function of emission polarization angle. **f**, Theoretical Auger recombination-limited internal

QY for InAs, PbSe, GaSb, and bP at room temperature and the measured internal quantum efficiency of bP device shown in panel **e**. **g**, Overlay of 500 EL spectra and **h**, EL spectral peak shift observed in a bP-LED, during 500 cycles of bending (1.06±0.05 %, tensile) and relaxation. Note that bP thickness of the device is 20 nm and all the EL measurements were performed at a current density of 20 A/cm^2.

Non-dispersive infrared (NDIR) gas sensing has attracted great interest due to its fast response and stable lifetime[38]. Thermal emitters (e.g. tungsten filament lamps) are often used in NDIR gas sensors as light sources, but their slow modulation and high power consumption remain key challenges that make them disadvantageous for use in real-time gas monitoring devices with extended lifetime towards the 'Internet of Things'[39,40]. Therefore, strain-tunable bP-LEDs with low operating power, fast modulation, and rapid stabilization suggest a solution, permitting multiplexed gas detection with a single light source, where the emission wavelength can be tuned over a broad range to suit various target gases. Our NDIR gas sensing setup (Fig. 4a) and measurement process are detailed in Methods. The strain applied to our bP-LED is varied so that the peak wavelength of the EL spectrum is shifted to match the dominant absorption peaks of H_2O, CH_4, and CO_2 (Fig. S5a). Since the emission spectrum of our bP-LED under compressive strain had a large overlap with the absorption spectrum of CO_2 (Fig. 4b), the EL intensity from a bP-LED measured by the detector at 4.3 μm was attenuated by the CO_2 absorption, enabling detection over a wide range of CO_2 concentrations varying from 0.005 to 100 % (Fig. 4d). On the other hand, under 0.3 % tensile strain, the CH_4 gas with a concentration range of 0.05 to 2.5 % (50 % of the lower explosive limit) was detected, resulting from the attenuation of measured EL intensity corresponding to CH_4 absorption at 3.3 μm (Fig. 4c,e). Selectivity of gas sensing between CO_2 and CH_4 and the long-term stability of the setup were also characterized (Fig. S5b-e). The EL intensity measured by the photodiode as a function of target gas concentrations was fit using the modified Beer-Lambert law model, given by:

$$\mathrm{FA} = \frac{\left(I_{N_2} - I_x\right)}{I_{N_2}} = 1 - \exp(-kLx) \qquad (4)$$

where FA is fractional absorbance of the target gas, I_{N_2} and I_x are the EL intensity measured by the photodiode under a nitrogen purge and at a target gas concentration of x, respectively, k is a fitting constant, and L is the chamber length (2'') (Fig. 4d,e, inset). By leveraging the repeatable and continuous tuning capability of our strain-tunable bP-LED, we demonstrated multiplexed gas sensing (Fig. 4f). Responses from the individual gases (CH_4 only, CO_2 only, and water only) are measured to characterize the selectivity of our multiplexed gas sensing system. A sequence of responses from a mixture gas pulse consisting of 0.2 % CO_2, 2 % CH_4, and H_2O at 20 % relative humidity (R.H.) indicates that H_2O (1.0 % tensile strain), CH_4 (0.3 % tensile strain), and CO_2 (compressive strain) are detected with a single light source, upon the application

of different strains to tune the peak emission wavelength of the bP-LED.

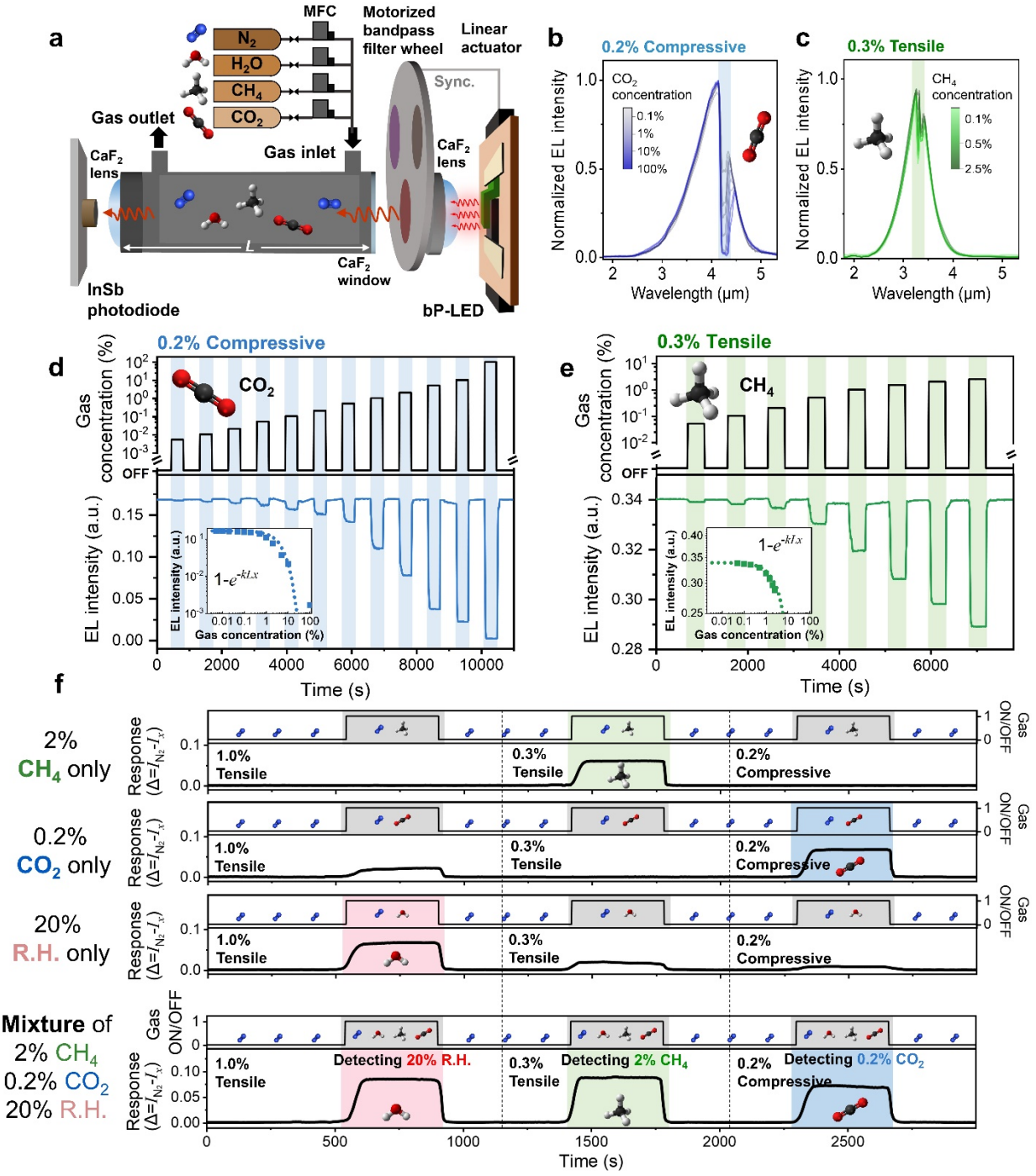

Fig. 4. a, Schematic diagram of the NDIR gas sensing system using a strain-tunable bP-LED. **b**,**c**,

Normalized EL spectra of a bP-LED (0.2 %, compressive) in the presence of CO_2 gas (**b**) and bP-LED (0.3 %, tensile) in the presence of CH_4 gas (**c**) at different concentrations. **d**,**e**, Sensor response characteristics using bP-LED (0.2 %, compressive) for varying concentrations of CO_2 pulses (**d**) and bP-LED (0.3 %, tensile) for varying concentrations of CH_4 pulses (**e**). Inset: the data fit using Beer-Lambert law model. **f**, Real-time multiplexed sensing of the individual target gas, from a gas mixture consisting of H_2O (20 % R.H.), CH_4 (2 %), and CO_2 (0.2 %), using bP-LED under 1.0 % tensile, 0.3 % tensile, and 0.2 % compressive strain, respectively. Responses from individual gases (CH_4, CO_2, and H_2O) are measured under different strains to characterize the selectivity of multiplexed gas sensing system. Note that the EL intensity (**d**-**e**) is the value recorded by the InSb photodiode on the opposite end of the gas cell.

4.3 Actively variable spectrum infrared photodetectors

Photodetectors based on bP have been extensively studied[41-48]. In this work, the same concept was applied to realize actively tunable photodetection with bP. Spectrally tunable bP-based photoconductors are fabricated on a PETG substrate to apply strain (Fig. S6a,b). As the tensile strain was applied in the ZZ (*y*) orientation of bP (Fig. S6c), the cutoff wavelength (the wavelength at which the responsivity is 50 % of the peak value) of the bP photoconductor was continuously tuned from 4.32 μm (0.4 %, compressive) to 2.44 μm (1.0 %, tensile) (Fig. S6d). Our strain-tunable bP photoconductor shows a peak D^* of 5.97×10^9 cm $Hz^{1/2}$ W^{-1} at $\lambda = 4.0$ μm (0.4 %, compressive) and a peak D^* of 8.45×10^9 cm $Hz^{1/2}$ W^{-1} at $\lambda = 2.0$ μm (1.0 %, tensile) (Fig. S7c), which are promising among the commercially available photodetectors, especially for room temperature operations. This suggests that our strategy can bridge the photodetection gap in the wavelength range between SWIR and MWIR. The strain-tunable bP photoconductor thus combines both benefits, i.e. high detectivity at room temperature and broadband tuning capability, arising from the highly strain-sensitive bP bandgap[19-22]. Detailed characterization and analysis for photodetection are provided in Methods and Fig. S6 and S7.

In summary, we utilized the strain-tunable bandgap of bP to develop actively tunable IR optoelectronic devices including LEDs and photodetectors at room temperature. The AVSO devices developed here have unprecedented versatility and thus important implications in fields such as optical communications, chemical sensing, and spectroscopy, where a tunable spectrum is required. To this end, we demonstrated one such application of this tunable optoelectronic platform by performing multiplexed gas sensing with a single device. By expanding upon this approach, one could potentially explore integration of devices on piezoelectric substrates or utilizing MEMS structure although there are a number of processing challenges that need to be overcome. Furthermore, it may be possible to extend to long-wave infrared (LWIR) wavelengths by further increasing the amount of compressive strain applied to bP through substrate engineering. This active strain tuning scheme may be applicable to other 2D materials as well, providing a path towards spectrally tunable optoelectronics across the electromagnetic spectrum.

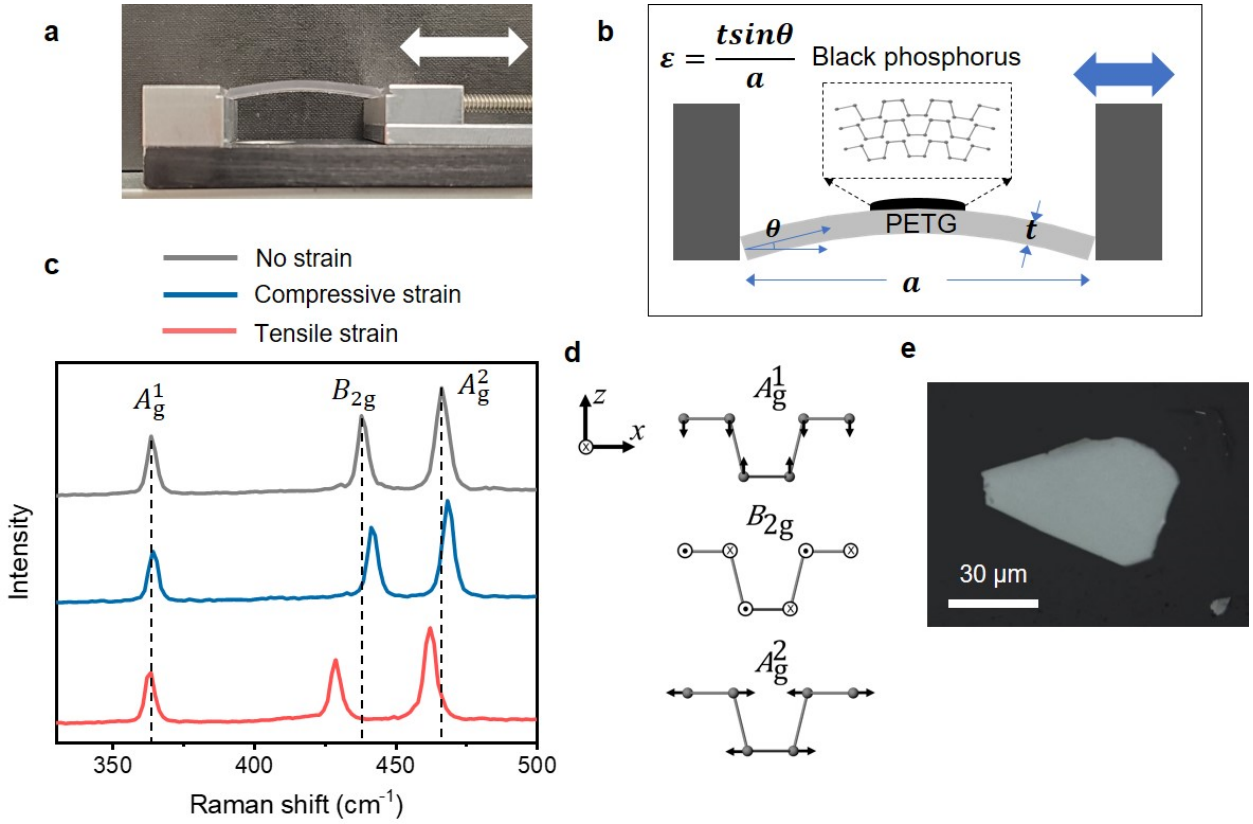

Fig. S1. a, Photographic image of two-point bending apparatus setup used in this work. An electrical linear actuator that can push/pull the one point of the two-point bending apparatus applies the continuous and precise amount of uniaxial tensile strain in bP. **b**, Schematic of the two-point bending apparatus. The strain is calculated as $\varepsilon = tsin\theta/a$ where ε is the amount of strain, t is the thickness of the substrate, a is the length of the substrate, and θ is the angle representing the bending, which is equal to $a/(2R)$ where R is the radius of the curvature[60]. Note that the circular arc approximation is not satisfied when θ is large at the strain > ~20 %[61]. **c**, Raman spectra of the bP measured in Fig. 1 and Fig. 2. **d**, Schematic of the atomic vibrations corresponding to Raman modes of A_g^1 (out-of-plane), B_{2g} (in-plane, zigzag), and A_g^2 (in-plane, armchair). **e,** Optical image of the strained bP flake on the PETG substrate.

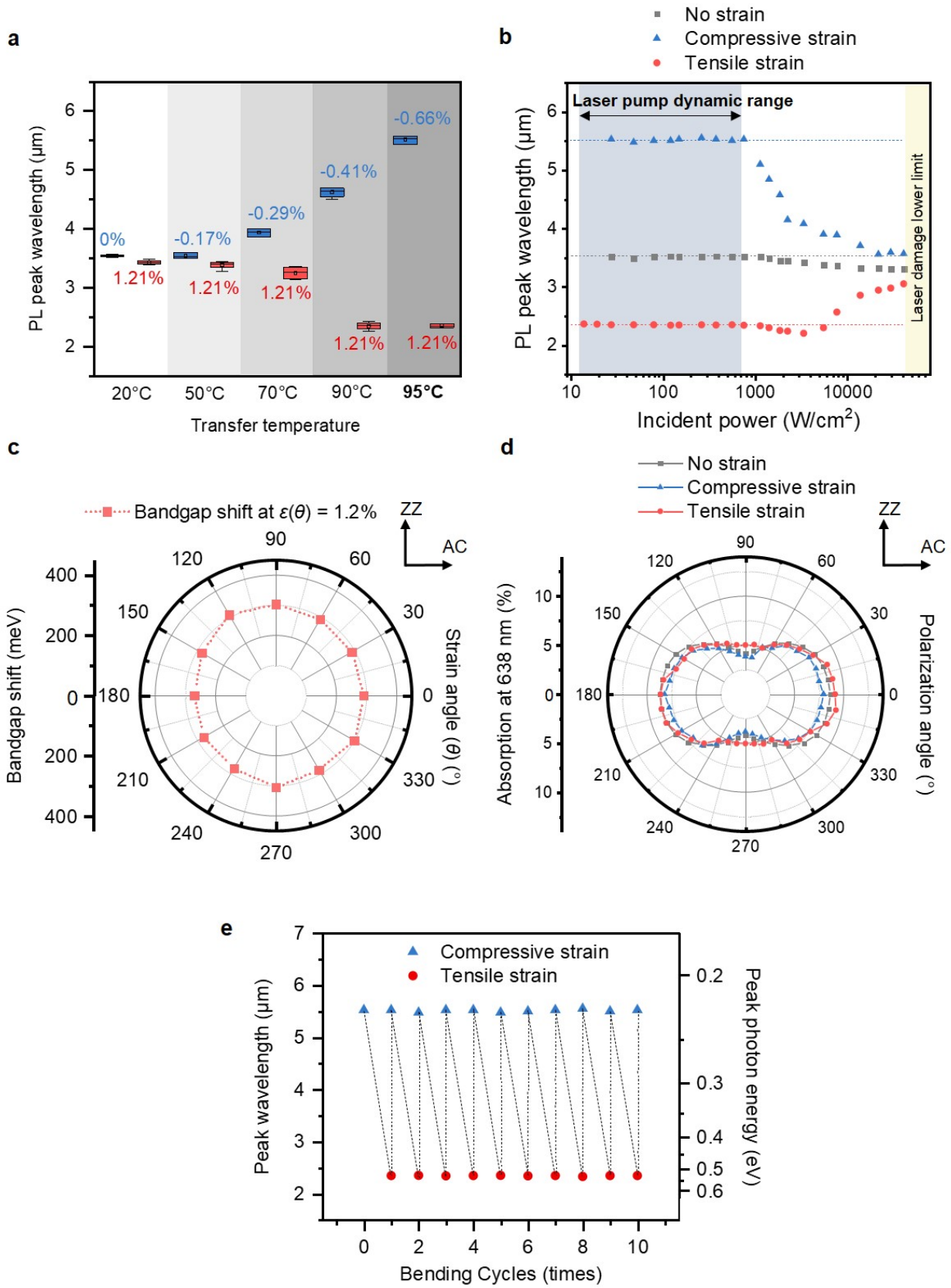
a
PL peak wavelength (μm)
0%
-0.17%
-0.29%
-0.41%
-0.66%
1.21%
1.21%
1.21%
1.21%
1.21%
20°C
50°C
70°C
90°C
95°C
Transfer temperature
b
No strain
Compressive strain
Tensile strain
Laser pump dynamic range
Laser damage lower limit
PL peak wavelength (μm)
Incident power (W/cm²)
c
Bandgap shift at ε(θ) = 1.2%
ZZ
AC
Bandgap shift (meV)
Strain angle (θ) (°)
d
No strain
Compressive strain
Tensile strain
ZZ
AC
Absorption at 638 nm (%)
Polarization angle (°)
e
Compressive strain
Tensile strain
Peak wavelength (μm)
Peak photon energy (eV)
Bending Cycles (times)

Fig. S2. a, PL peak wavelength as a function of transfer temperature. The PL peak wavelength as a function of biaxial compressive strain before and after application of tensile strain (1.21 %, ZZ) was characterized. Each measurement was performed for five samples of bP with thickness 20-22 nm. Samples were compressively strained by different amounts *via* different transfer temperature (T_{tr} = 20°C, 50°C, 70°C, 90°C, and 95°C). It was observed that the PL peak shift resulting from tensile strain increased with increasing biaxial compressive strain (as determined by transfer temperature). This is understood to be the result of the following. At high biaxial strain, the larger friction-induced resistance prevents the sliding of the 2D materials[55]. At lower transfer temperatures, i.e. with reduced biaxial compressive strain, the bP is thus more likely to slip during bending of the substrate, making the intended uniaxial tensile strain not be efficiently delivered to the bP. This could be due to the fact that at lower values of biaxial strain (i.e. lower transfer temperatures), the friction-induced resistance that would prevent the sliding of the bP is reduced. **b**, Laser power dependence of strain effect. We characterized the laser-induced heating effect on the bandgap shift by measuring PL peak wavelengths as a function of laser power. Since the excitation spot size was about similar or slightly smaller than the size of the bP, it helped preventing the thermal expansion of the surrounding PETG by laser excitation, which could have acted as unexpected strain/slippage of bP from the PETG[62]. Regardless of the strain in bP, the excitation power higher than 1500 W/cm^2 always resulted in the blueshift of the PL, which is attributed to the thermal heating by laser[63]. Although the PL peak position was recovered after cooling down to room temperature without the excitation, when the laser intensity was even higher (> ~20 kW/cm^2), there was a visible damage in bP, which did not return to its original PL peak position. Therefore, our laser incident power for the PL measurement in this work was maintained below 600 W/ cm^2, at which power the PL peak of the exfoliated sample also remained constant without any shift. Also, this is the power range much lower than the lowest laser pump (~20 kW/cm^2) which is known to have a laser thermal effect in bP and MoS_2 transferred on polyimide or PDMS[62,63]. **c**, Bandgap shift under different strain directions with respect to the crystal orientation of bP. With changing direction of tensile strain with respect to the crystal orientation of bP, there was no apparent difference in the amount of strain-induced bandgap shift. This observation is consistent with previous results from a similar bending experiment performed on 6L bP atop a polyethylene terephthalate (PET) substrate[22]. **d**, Absorption at excitation wavelength for bP without strain and bP with compressive strain and with 1.21 % of uniaxial tensile strain. It was observed that the strain did not have significant effects on the light absorption of bP at the PL excitation wavelength. Even though the bP bandgap was being modulated by strain, because our excitation wavelength was far from the absorption edge the PL enhancement cannot be attributed to increased absorption. **e**, The reversibility and repeatability of the bandgap tuning in bP using compressive strain (0.6%) and tensile strain (1.2%) are demonstrated. The PL peak from 20 nm bP is shifted and recovered throughout the 10 cycles of bending and relaxation. At much higher strain, the PETG turns into plastic deformation, exhibiting no return to its original state.

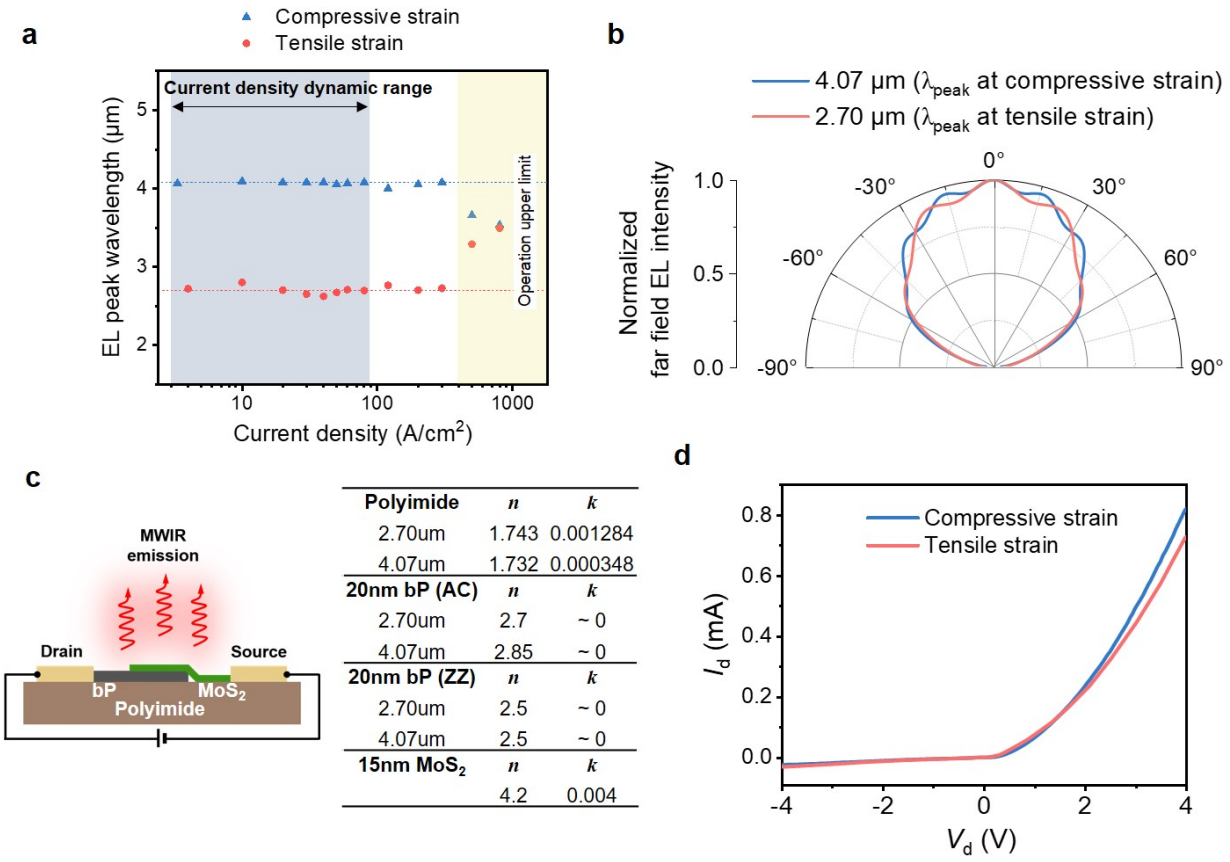

Polyimide	*n*	*k*
2.70um	1.743	0.001284
4.07um	1.732	0.000348
20nm bP (AC)	***n***	***k***
2.70um	2.7	~ 0
4.07um	2.85	~ 0
20nm bP (ZZ)	***n***	***k***
2.70um	2.5	~ 0
4.07um	2.5	~ 0
15nm MoS_2	***n***	***k***
	4.2	0.004

Fig. S3. a, Current density dependence of EL peak wavelength showing the reliability of strain-tunable emission in different injection levels. To prevent the degradation at elevated temperature and minimize the effect of the localized hot spots on the device performance, a polyimide film with high thermal conductivity was used in this study, coupled with Peltier module, to facilitate heat dissipation and keep the constant temperature during operation. Moreover, the forward current density was maintained below 20 % of the lowest injection level where thermal failure started to take place. When the current density was high, the devices failed earlier and the visible degradation was observed in the channel region. Therefore, the current levels were maintained within the range shown in the figure (4 A/cm^2 ~ 90 A/cm^2) and the device showed stable operations over ~8 hours, which will be discussed later (Fig. S5d,e). **b**, Angular intensity distribution of the strain-engineered bP-LED calculated with FDTD simulations (FDTD Solutions, Lumerical). **c**, Table showing the complex refractive indices of the polyimide substrate, bP, and MoS_2 from the literature[28,47,64-66], which was used for the simulation. While the precise computation awaits further study on the refractive index changes of bP with strains (compressive strain and tensile strain), we simply calculated the angular distribution of bP-LED at two different peak wavelengths, using the refractive indices of bP without strain from the literature. It was shown that the angular distributions at two different wavelengths were close enough to assume that there was no discrepancy between the power collections at these two emission wavelengths using the objective lens with a fixed collection angle. **d**, *I-V* curves of strain-tunable bP/MoS_2 LED measured at compressive strain and 1.06 % of tensile strain.

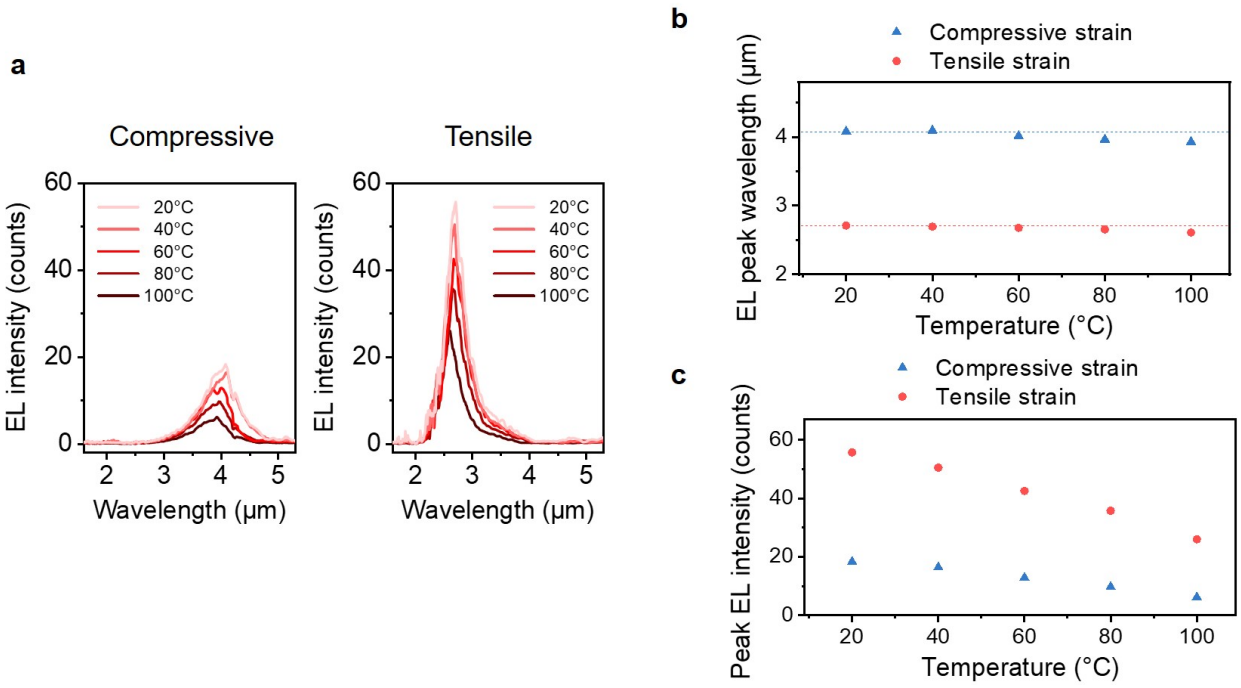

Fig. S4. a, EL spectra for bP-LED operating at constant current density of 20 A/cm^2 at different temperatures under compressive strain (0.2 %) and tensile strain (1.0 %). **b,c,** Peak wavelength (**b**) and peak intensity (**c**) of the EL from bP-LED under different strains at different temperature. Note that, for heat dissipation and uniform temperature control during the device operation, dry nitrogen gas was consistently purged, and a mechanically flexible heat sink was installed, which was connected to the cold finger of the cryostat.

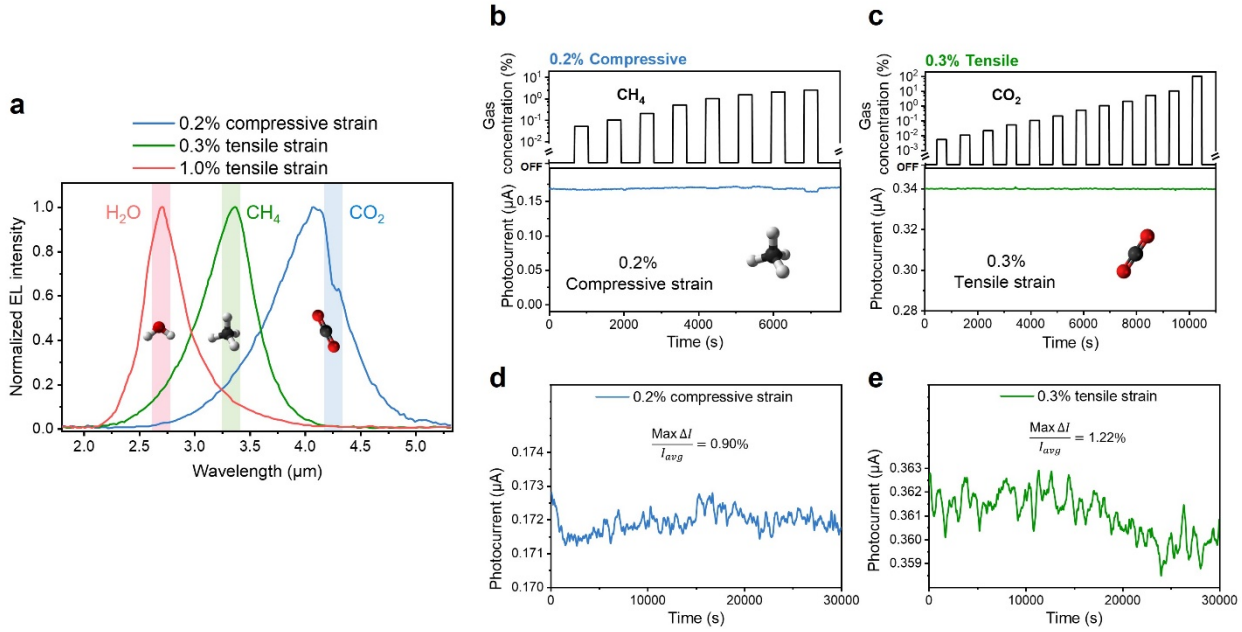

Fig. S5. a, Normalized EL spectra of bP-LED with compressive strain, 0.3 % tensile strain, and 1.0 % tensile strain for detecting CO_2, CH_4, and H_2O, respectively. **b**,**c**, The sensor response from the device under compressive strain in presence of CH_4 gas (**b**) and 0.3 % of tensile strain in presence of CO_2 gas (**c**). Our approach showed minimal detection at a concentration of 2.5 % under compressive strain, while at 0.3 % of tensile strain, it no longer showed the ability to detect CO_2 gas. **d**,**e**, The stability of the gas-sensing setup for the bP-LED measured under compressive strain (**d**) and 0.3 % of tensile strain (**e**). Both measurements were performed at the current density of 20 A/cm^2 with f_{mod}=1 kHz. Over 8 hours of measurement, the device exhibited a maximum drift of 0.90 % and 1.22% for compressive strain and 0.3 % tensile strain, respectively.

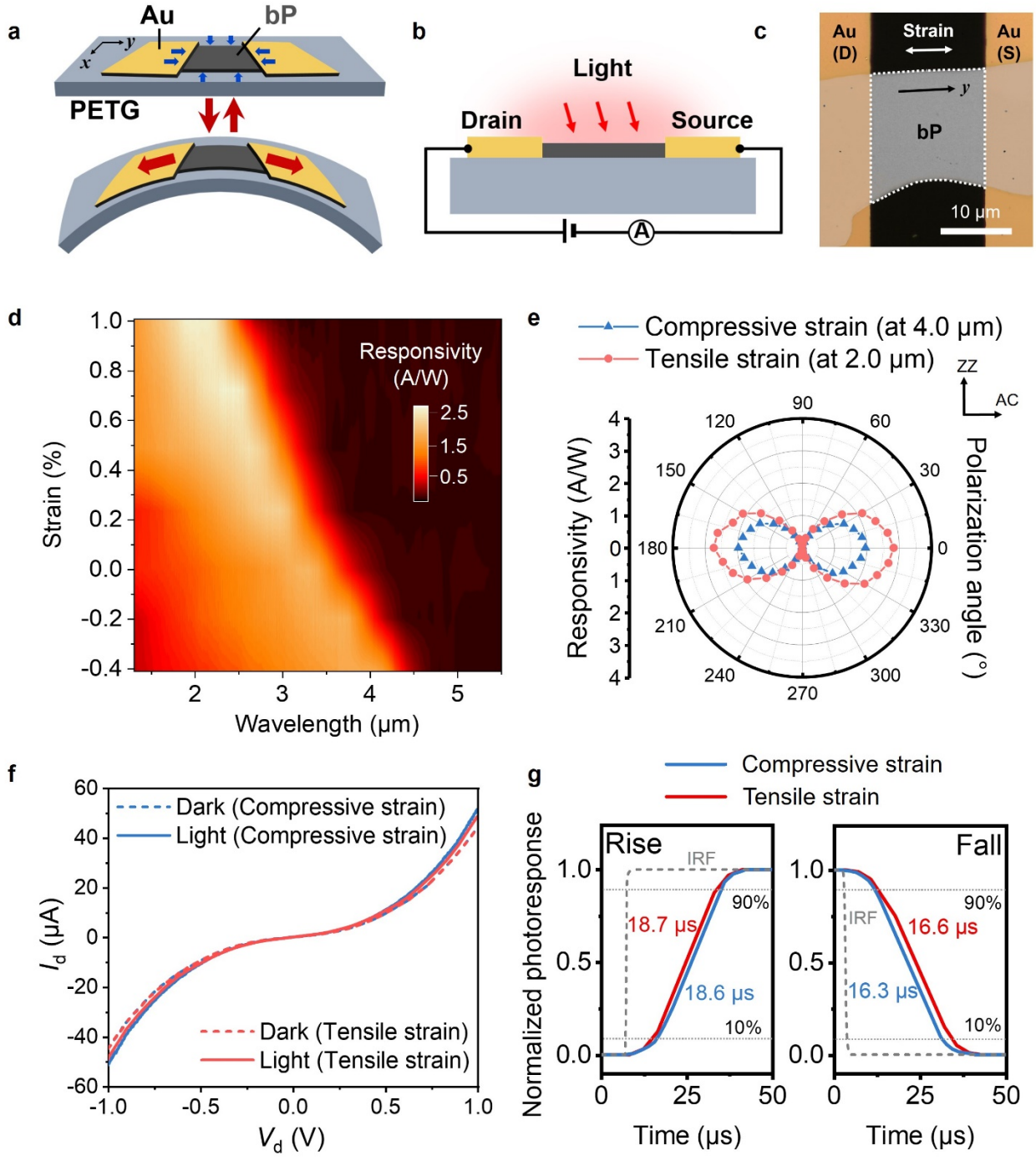

Fig. S6. a, Schematic of a strain-tunable bP photoconductor. **b**, Schematic of device architecture, showing the photocurrent generation at a bias voltage. **c**, Optical micrograph of the device. **d**, Strain-dependent spectral photoresponse. **e**, Polarization-dependent responsivity at 4.0 μm and 2.0 μm for the device under compressive and 1.0 % of tensile strain, respectively. **f**, *I-V* curves of

strain-tunable bP photoconductor measured in the dark and under illumination by a 1000 K black body. **g**, Rise and fall times (10-90 %) under 0.4 % compressive and 1.0 % tensile strain, using 1650 nm laser at ~ 10 mW/cm^2. All measurements were conducted at a bias voltage of 100 mV from a device with 22 nm bP thickness.

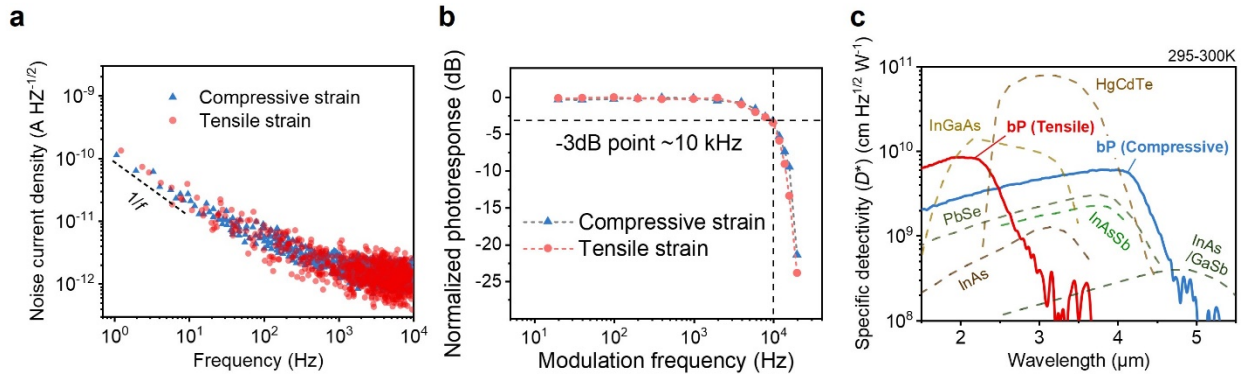

Fig. S7. a, Spectral noise density under 0.4 % compressive and 1.0 % tensile strain. Dashed line indicates the 1/*f* curve at low frequency. **b**, Normalized photoresponse of strain-tunable bP photoconductor measured as a function of modulation frequency. The device is measured at V_d = 100 mV and excited by a 1650 nm laser, showing a 3-dB frequency of 10 kHz. **c**, Specific detectivity (*D**) as a function of wavelength at room temperature, for the device with 0.4 % compressive and 1.0 % tensile strain as well as various commercially available photodetectors.

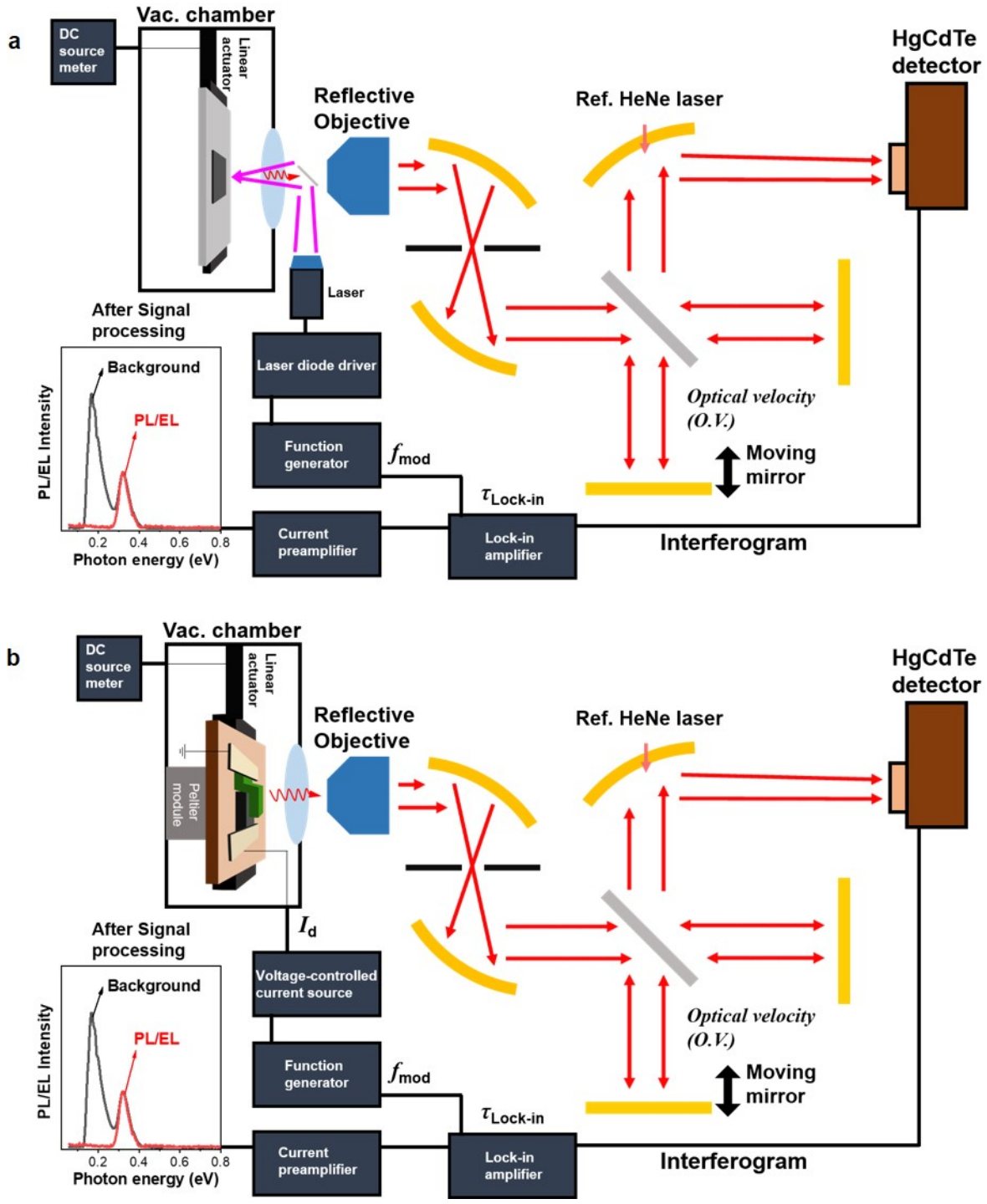

Fig. S8. a, Schematic diagram of the IRPL measurement setup and **b**, Schematic diagram of the IREL measurement setup used in this work. For both measurements, the emission from bP was collected by a reflective objective and sent to the external port of the FTIR, with f_{mod} = 5 kHz,

$\tau_{Lock\text{-}in}$ = 300 μs, and *O.V.* = 0.0633 cm/s. Both the total interferogram from the HgCdTe (MCT) detector and the modulated interferogram from the current amplifier were utilized to separate the PL/EL signal from the thermal background.

Table S1. Strain-induced bandgap shift of semiconductors in the SWIR/ MWIR range.

Material	Bandgap shift rate (meV/%)	Bandgap (ε = 0 %) (eV)	Applied strain		Reference
			Type	Value (%)	
bP	162	0.35	Uniaxial (ZZ)	-0.66 ~ 1.21	**This work**
InAs	36	0.35	Biaxial	-3.2	[67]
InN	10	0.7	Biaxial	-9.9	[68][69]
Ge	62	0.67	Biaxial	-0.13 ~ 1.78	[70]

Table S2.| Parameters used to calculate theoretical QY from ABC model.

Material	n_i (cm^{-3})	B (cm^3/s)	C (cm^6/s)	References
InAs	1.0×10^{16}	1.1×10^{-10}	1.1×10^{-26}	[71][72]
PbSe	3.0×10^{16}	8.0×10^{-11}	1.1×10^{-28}	[73][74]
GaSb	9.6×10^{11}	3.8×10^{-10}	9.3×10^{-28}	[71][75]
bP (25 nm)	2.5×10^{15}	2.7×10^{-21}	4.1×10^{-43}	[76]

Experimental and theoretical details

Sample preparation

BP crystals (Smart Elements) were mechanically exfoliated onto a polydimethylsiloxane (PDMS) substrate (1×1 cm^2) with PVC tape (SPV224, Nitto). Prior to the transfer process, the crystal orientation of bP was identified by polarization-resolved Raman spectroscopy, following the

method described in previous work[49]. The transfer process used here is similar to the dry-transfer process described previously[50]. It was performed in a modified optical microscope setup (Labophot, Nikon) with the sample stage replaced by a hotplate. A PETG substrate (2.54 mm thick, 3×3 cm^2) was placed on a hotplate at 95 °C. The exfoliated bP on PDMS stamp was positioned upside down and aligned with the center of the PETG substrate. The stamp was slowly brought into contact with the thermally expanded PETG and bP was transferred at 95 °C. The bP-transferred PETG substrate was immediately subjected to rapid thermal quenching, bring it down to room temperature. Due to the CTE mismatch and the rapid thermal quenching process, bP is subjected to biaxial compressive strain. After the transfer, the prepared bP sample with biaxial compressive strain was loaded into the two-point bending apparatus (Extended Data Fig. 1a) inside the optical cryostat (ST-100, Janis). All processes were performed inside a N_2-purged glovebox (830-ABC, Plas-Labs) or in environments with minimum moisture and light exposure, to avoid any ambient atmosphere-induced bP oxidation.

Device fabrication

For LED fabrication, electronic-grade polyimide (0.5 mm thick, 1×1 cm^2) was used as a substrate instead of PETG due to its compatibility with electron-beam lithography processes. The exfoliation and transfer process of bP and MoS_2 followed the same procedure as mentioned in the sample preparation section. BP (thickness ~15-22 nm) was first transferred onto the polyimide substrate at 180 °C, followed by rapid quenching to room temperature. Subsequently, MoS_2 (thickness ~10-15 nm, SPI Supplies) exfoliated on a PDMS stamp, was transferred on top of the bP at room temperature to form an electron contact to the bP. Source and drain electrodes were patterned by conventional electron-beam lithography using poly(methyl methacrylate) (PMMA) C4 resist (baked at 130 °C) and thermal evaporation of 40 nm Ni.

For photoconductor fabrication, bright field-mode photolithography was used, followed by subtractive wet chemical etching, where the opaque portion of the photomask is the desired electrode patterns. First, 100 nm Au was evaporated on the bP-transferred PETG, which was prepared by the methods mentioned earlier. S1818 (Shipley Microposit) was coated on bP-transferred PETG and the sample was baked at 80 °C for 3 min, which is below the glass transition temperature of PETG (90-95 °C). After the g-line exposure using a bright field photomask, followed by the development process (MF-26A, Microchem), the exposed Au region was completely etched using a gold etchant (potassium iodide, Transene). Finally, the residual photoresist layer was removed by flood exposure followed by the development process.

Optical characterization

All optical measurements were performed in a customized cryostat (ST-100, Janis) with a CaF_2 window, which was evacuated to a base pressure $<10^{-5}$ Torr. A two-point bending apparatus was installed with the electric actuator inside the cryostat, so that the amount of uniaxial tensile strain can be simultaneously controlled during the measurement. For PL and EL measurements, a 15x reflective objective was installed at the auxiliary entrance port of the FT-IR (iS50, Thermo Fisher), collecting the sample signal and sending it to the FT-IR spectrometer equipped with a CaF_2 beam splitter and a liquid N_2-cooled HgCdTe (MCT) detector. A laser diode (Thorlabs, λ=638 nm) and

a laser diode controller (LDC500, Thorlabs) were used as the excitation source for the PL measurements. A mirror was installed at the obscured center of the reflective objective to reflect the focused excitation beam onto the sample. The polarization of the excitation laser was aligned to be parallel to the AC orientation of bP by rotating the polarization plane using a linear polarizer followed by a half-wave plate. For EL measurement, a voltage controlled current source (CS580, Stanford Research Systems) was used to apply a forward current bias. The instrument response function of the setup accounted for different wavelengths and polarizations, following the same procedure as described in our previous work[47]. For the spectrum calculation process, double modulation was used to separate the PL/EL signal from the thermal background in the modulated interferogram, which was obtained through a lock-in amplifier (SR865, Stanford Research Systems) and low-noise current preamplifier (SR560, Stanford Research Systems). Details of the PL and EL measurement setup are further described in Fig. S8.

Photodetector characterization was performed at the auxiliary exit port of the FT-IR, where the bP photoconductor was excited by modulated 1000 K blackbody illumination. The device was biased at 100 mV. The generated photocurrent was amplified by the low-noise current preamplifier (SR570, Stanford Research Systems) and sent to the external detector interface of the FT-IR system, in order to resolve the full spectral responsivity. A BaF_2 linear polarizer was placed at the unpolarized excitation path for the polarization resolved photoresponse measurements. For temporal photoresponse measurements, a laser diode (Thorlabs, λ=1650 nm) was modulated by a square wave generated using a function generator (81150A, Agilent). The FT-IR system was calibrated following the procedure described in our previous work[47]. An internal deuterated-triglycine sulfate (DTGS) detector was used to measure the relative spectral intensity of the excitation. A NIST-calibrated Ge photodiode (Thorlabs) and InSb photodiode (Teledyne Judson Technologies) were used as reference to determine the absolute responsivity of our bP photoconductors, as a function of wavelength. Raman measurement was performed in a commercial setup (inVia, Renishaw) with a 532 nm laser excitation, which was linearly polarized along 45° with respect to the AC and ZZ orientation of bP, in order to optimize the signal intensity from all three characteristic Raman modes (A_g^1, B_{2g}, and A_g^2) at the same time. For both PL and Raman measurements, the lowest excitation power that gave a perceptible signal-to-noise ratio (SNR) was used, to prevent any localized heat-induced strain effects in bP. The effects of laser-induced heating on the strain conditions of bP is characterized in Fig. S2b.

NDIR gas sensing characterization

In the NDIR gas sensing setup, target gases and diluent gas (N_2) were injected into an enclosed gas cell, which was illuminated by the bP-LED at one end. At the opposite end, a commercial InSb photodiode was used to measure the light intensity passing through the gas cell (Fig. 4a). EL spectra (Fig. 4b,c) were measured by the internal MCT detector in the FT-IR system, under the constant flow of a target gas at various concentrations. NDIR gas sensor responses (Fig. 4d,e and Extended Data Fig. 5b,c) were characterized by a commercial liquid N_2-cooled InSb photodiode to a sequence of target gas pulses and purging cycles of N_2 gas. A pair of CaF_2 plano-convex lenses or 15x reflective objectives were used to improve the dynamic range of the measurements. A motorized filter wheel (FW102C, Thorlabs) was used with the bandpass filters for H_2O (Center

wavelength (CWL) = 2700 nm, Iridian), CH_4 (CWL = 3330 nm, Thorlabs), and CO_2 (CWL = 4260 nm, Thorlabs) detection. The bP-LED was modulated at 1 kHz and the generated photocurrent for the InSb photodiode was amplified using a low-noise current preamplifier (Stanford Research Systems) and measured by the lock-in amplifier (Stanford Research Systems). CH_4 gas cylinder (2.5 %), CO_2 gas cylinder (> 99.9 %), and moisture-containing N_2 gas cylinder were connected to individual mass flow controllers (Alicat) to mix and deliver the gas pulse with precise concentrations. Humidity inside the gas cell was monitored by a commercial digital humidity sensor (SHT2x, Sensirion). At room temperature (292-295 K), the current density was kept at 20 A/cm^2 for all measurements using 20 nm bP-LED. It is noted that the baseline current (I_{N_2}) was different when the system was configured to sense the different gases. This is attributed to the changing emission intensity from the bP-LED subjected to applied strain conditions, different transmission values of the filters used for each gas detection, and the varying spectral response of the InSb photodiode.

BP for strain application

Exfoliated bP flakes with cracks or wrinkles did not show any strain-induced bandgap modification with our methods described in this work. Significant efforts were thus made during the sample preparation and fabrication to avoid cracks/wrinkles within bP flakes. We mainly focused on the demonstration of bandgap tuning and its device applications for bP with thicknesses of 15-22 nm. For this thickness range, carrier transport is less susceptible to environment than thinner bP, while strain-induced bandgap tuning has a higher yield than its thicker counterpart. We found that the strain-induced bandgap modification using our method started to become less effective for bP thicker than 22 nm, possibly due to slippage between the bP and the substrate. On the other hand, bP thinner than 15 nm had a lower yield of bandgap tuning by strain, which could be attributed to the difficulty in processing thinner bP without cracks, and accelerated oxidation in thinner bP from layer-by-layer thinning[51]. Since the thickness characterization of bP was challenging with direct atomic force microscopy (AFM) on a soft polymer substrate, we used the method described in the previous work[20] to identify the bP with a suitable thickness.

Compressive strain application

Negative bending (i.e. in opposite direction to that used for tensile strain) was first used with the goal of applying compressive strain. However, this induced decoupling of bP from the substrate and buckling of bP possibly due to the Poisson effect. Therefore, to apply compressive strain, thermal expansion mismatch between bP and substrate was used instead. PETG is the material that was selected as a substrate as it was found to have favorable properties compared to other polymers (e.g. Polypropylene (PP), Polyethylene (PE), Ethylene-vinyl acetate (EVA), Polycarbonate (PC), Polyvinylidene fluoride (PVDF), PDMS, Nylon, Polyvinyl chloride (PVC), Polystyrene (PS), and Teflon). A transfer temperature of 95 °C was used, which is slightly higher than the glass transition temperature of PETG. The CTE of PETG was experimentally measured to be 80.5 ± 2.5 ppm/°C and 520 ± 32 ppm/°C, over the temperature range of 20-90 °C and 90-95 °C, respectively, indicating that the thermal expansion rate rapidly increases at the glass transition temperature[52]. It was found that the higher transfer temperature (T = 100 °C) resulted in wrinkles and delamination of bP due to the low adhesion and excessive compressive strain from the substrate[53] and did not

contribute to larger modulation range by strain. Therefore, we did not use transfer temperatures in excess of 95 °C. BP has anisotropic CTEs of 33 (AC) and 22 (ZZ) ppm/°C[54]. The compressive strain applied in bP due to the CTE mismatch can thus be calculated as follows:

$$\varepsilon(T_{\mathrm{tr}}) = \int_{20^{\circ}\mathrm{C}}^{T_{\mathrm{tr}}} \alpha_{\mathrm{sub}}(T)dT - \int_{20^{\circ}\mathrm{C}}^{T_{\mathrm{tr}}} \alpha_{\mathrm{bP}}(T)dT \qquad (1)$$

where T_{tr} is the transfer temperature of bP onto the substrate, α_{sub} is the CTE of the substrate, and α_{bP} is the CTE of bP. The compressive strain resulting from this quenching process was 0.58 % in the AC direction and 0.66 % in the ZZ direction. The strain in AC (x) direction can be obtained using the Poisson's ratio of bP.

Substrate for device fabrication

The chemical instability of bP has been a main roadblock in demonstrating strain-tunable optoelectronic devices based on bP. Here, we developed a method and procedure that are compatible with conventional lithography, while maintaining the material composition and device performance of bP. Although the polyimide has a lower CTE (experimentally measured to be 34.8 ± 1.5 ppm/°C at 20-200 °C) and is softer than PETG, it was used for bP/MoS_2 LEDs for following reasons. Polyimide is chemically stable, resistant to high temperature (>100 °C), and compatible with conventional lithography processes and organic solvent processing. These enable electrode patterning with a desired shape and higher spatial resolution, which reduces the series resistance of the LEDs. In addition, the electronic-grade polyimide we use has a higher thermal conductivity than PETG, which is advantageous for repeated operations over long periods of time without performance degradation due to thermal failure and charging issues.

Preserving strain and stability during fabrication

The built-in strain between a 2D transition metal dichalcogenide (TMDC) monolayer and the substrate can be released by solvent evaporation-mediated decoupling process[55]. However, we find that the bP-MoS_2 LED in our work still preserved partial compressive strain after the fabrication. This can be attributed to the source/drain electrodes and MoS_2 being on top of the bP, which serve as a clamp to prevent the complete release of the biaxial compressive strain between bP and the polyimide substrate. During the lift-off process, acetone evaporation was avoided and toluene was used instead of isopropyl alcohol (IPA), which prevents the release the built-in strain in 2D materials due to evaporation. For the fabrication of bP photoconductor, the photoresist developer (MF-26A) and the gold etchant (potassium iodide) did not affect the biaxial compressive strain in bP, which was mostly maintained after the fabrication was completed. Moreover, the gold film evaporated on bP could have functioned as a clamping agent, adding/holding the biaxial compressive strain in bP. It is reported in our earlier work that metal evaporation on 2D materials results in the biaxial compressive strain due to the thermal expansion mismatch between the metal and material[56,57]. During photoconductor fabrication, except the 5s of g-line exposure, visible light exposure of bP was minimized to prevent photooxidation. In agreement with the previous work[58], we observed that the gold etchant (potassium iodide) and DI water alone did not induce bP oxidation and the device performance was not degraded during the fabrication. It is understood

that water, oxygen, and visible light are simultaneously required for oxidation of bP.

Measurement accuracy

Rather than using extinction spectra to estimate the bandgap, we instead used IRPL spectroscopy to characterize the bandgap modification in bP under strain. For EL and PL measurement, it is important to note that the measurement setup was calibrated for each value of strain, to capture the absolute intensity of light emission from the non-planar surface. This was required to exclude the possibility of focal plane drift upon bending of the substrate. For the PL measurements, the excitation laser spot size (~ 1600 μm^2) was maintained to be slightly smaller than the size of the bP flake. At each measurement, the polarization of excitation with respect to the bP crystal orientation was verified by comparing the results between rotating the polarizer in the excitation path and rotating the sample with respect to a fixed laser polarization. BP absorption at the PL excitation wavelength (638 nm) was observed to be weakly dependent on the polarization angle, while it is expected to have the highest anisotropy near the absorption edge[43]. For photoconductor characterization, a fixed voltage bias of V_{ds} = 100 mV (smaller than the bP bandgap) was used for all measurements to maintain the responsivity of the photoconductor in a linear regime.

LED efficiency calibration

To quantify the light emission efficiency of our bP-LEDs, we used 4.05 μm quantum cascade laser (QF4050T1, Thorlabs) and an infrared reflectance standard (Labsphere). The laser output power was measured using a high sensitivity thermal power sensor (Ophir) at the focal plane of the objective. The laser signal intensity reflected by the Lambertian reflectance standard at the focal plane was measured by the FT-IR under the same measurement conditions. Using the ratio of the output power measured from the power sensor to the signal intensity measured by the MCT detector in the FT-IR, we can convert the emission intensity from bP-LED measured by the FT-IR into output power. The instrument response function (IRF) of the MCT detector is taken into consideration when accounting for the difference between the laser and bP-LED emission wavelengths. In addition, since the reflective objective has a fixed collection angle, the angular collection factor was calculated to account for the difference between the angular distribution of emission of the bP-LEDs and of the Lambertian emitter. The output power of our bP-LED is then calculated by:

$$\text{Power}_{\text{bPLED}} = \text{Intensity}_{\text{bPLED (FTIR)}} \times \frac{\text{Power}_{\text{laser (power meter)}}}{\text{Intensity}_{\text{laser (FTIR)}}} \times \frac{\text{IRF}\ (\lambda_{\text{bPLED}})}{\text{IRF}\ (\lambda=4.05\ \mu\text{m})} \times \frac{\text{Angular collection}_{\text{bPLED}}}{\text{Angular collection}_{\text{laser}}} \qquad (1)$$

where IRF (λ_{bPLED}) and IRF (λ=4.05 μm) are the instrument response function of the MCT detector at the bP-LED emission wavelength and 4.05 μm, respectively, and $\text{Angular collection}_{\text{bPLED}}$ and $\text{Angular collection}_{\text{laser}}$ are the collected signal with the objective lens when the on-axis (0°) emission intensity is assumed to be 1. Note that to estimate the instantaneous carrier concentration in the bP-LED at different current densities in Fig. 3f, we assume that the carriers are uniformly rdistributed in the bP volume.

Strain-tunable photodetection

As expected from the highly polarization-dependent absorption of bP[59], we observed the highest photoresponse when light was polarized in the AC direction and the lowest photoresponse when it was polarized in the ZZ direction (Fig. S6e). The *I-V* characteristics of the photoconductors under compressive and tensile strain conditions displayed no obvious difference (Fig. S6f). Under compressive strain, the rise and fall times of the photoconductors were measured to be 18.6 μs and 16.3 μs, respectively (Fig. S6g). Under tensile strain, they showed similar values of 18.7 μs and 16.6 μs, respectively. The noise current density did not show any significant variation between compressive strain and tensile strain conditions, and the low frequency noise dominated by the contribution from 1/*f* noise (Fig. S7a).

To estimate the performance of our tunable photoconductor, the specific detectivity (*D**) was calculated as

$$D^* = \frac{\sqrt{A\Delta f}}{NEP} \qquad (5)$$

where A is the device area, Δf is the bandwidth, and NEP is the noise equivalent power. The bandwidth of the photoconductor is measured to be 10 kHz under both compressive and tensile strain (Fig. S7b). A detailed discussion of the process we used to estimate *NEP* is provided in the latter part of Methods, where we utilized the experimentally extracted noise current to avoid an overestimation of D^*. Given a constant device area and integration time, the optimum bP thickness that maximizes the *D** of a bP photoconductor is reported to be ~25-35 nm, which originates from the balance between increasing absorption from greater thickness and reducing noise in fewer layers[48]. By applying strain to a photoconductor based on bP with a thickness close to this range, we can extend its spectral photoresponse while preserving optimal device performance. The detectivity could be further improved by enhancing the light collection efficiency of the device and/or implementing a gate bias to compensate for background doping[47,48].

Noise equivalent power (NEP) calculation

NEP is the optical power that gives a SNR of unity for a given measurement bandwidth of a photodetector. It is determined by calculating the photocurrent (I_{ph}= Responsivity (R_λ) × *NEP*) when SNR = 1 = I_{ph}^2 / $<i_{\mathrm{n}}^2>$. Since the total noise current is mainly determined by the sum of the contributions from shot noise and Johnson noise, we can formulate it as follows: $<i_{\mathrm{n}}^2> = 2e\left(I_{\mathrm{ph}} + I_{\mathrm{dark}}\right)\Delta f + \frac{4k_{\mathrm{B}}T}{R}\Delta f$, where e is the electron charge, Δf is the bandwidth, k_{B} is the Boltzmann constant, T is the temperature, and R is the dark resistance which is determined from the *I-V* characteristics of the photoconductor (Fig. S6f). Solving the equation ($I_{\mathrm{ph}}^2 - 2e\left(I_{\mathrm{ph}} + I_{\mathrm{dark}}\right)\Delta f - \frac{4k_{\mathrm{B}}T}{R}\Delta f = 0$) gives the value of I_{ph}, where all the other parameters in the equation are obtained from the experimental data. Therefore, NEP is calculated as $6.54476 \times 10^{-11}/R_\lambda^{\mathrm{compressive}}$ for compressive strain and $6.69445 \times 10^{-11}/R_\lambda^{\mathrm{tensile}}$ for tensile strain.

References

1. Kahn, J. M. & Barry, J. R. Wireless infrared communications. *Proc. IEEE* **85,** 265-298 (1997).
2. Vollmer, M. & Mollmann, K.-P. *Infrared thermal imaging: fundamentals, research and applications.* (Wiley-VCH, Weinheim, ed. 2, 2018).
3. Bagavathiappan, S., Lahiri, B. B., Saravanan, T., Philip, J. & Jayakumar, T. Infrared thermography for condition monitoring – a review. *Infrared Phys. Technol.* **60,** 35-55 (2013).
4. Baker, M. J. et al. Using Fourier transform IR spectroscopy to analyze biological materials. *Nat. Protoc.* **9,** 1771-1791 (2014).
5. Gibson, D. & Macgregor, C. A novel solid state non-dispersive infrared CO_2 gas sensor compatible with wireless and portable deployment. *Sensors* **13,** 7079-7103 (2013).
6. Haugan, H. J., Szmulowicz, F., Brown, G. J. & Mahalingam, K. Bandgap tuning of InAs/GaSb type-II superlattices for mid-infrared detection. *J. Appl. Phys.* **96,** 2580-2585 (2004).
7. Kang, J., Tongay, S., Zhou, J., Li, J. & Wu, J. Band offsets and heterostructures of two-dimensional semiconductors. *Appl. Phys. Lett.* **102,** 012111 (2013).
8. Wu, J. et al. Universal bandgap bowing in group-III nitride alloys. *Solid State Commun.* **127,** 411-414 (2003).
9. Ning, C.-Z., Dou, L. & Yang, P. Bandgap engineering in semiconductor alloy nanomaterials with widely tunable compositions. *Nat. Rev. Mater.* **2,** 17070 (2017).
10. Yang, Z. et al. Single-nanowire spectrometers. *Science* **365,** 1017-1020 (2019).
11. Kramer, I. J., Levina, L., Debnath, R., Zhitomirsky, D., & Sargent, E. H. Solar cells using quantum funnels. *Nano Lett.* **11,** 3701-3706 (2011).
12. Whitney, W. S. et al. Field effect optoelectronic modulation of quantum-confined carriers in black phosphorus. *Nano Lett.* **17,** 78-84 (2017).
13. Liu, Y. et al. Gate-tunable giant stark effect in few-layer black phosphorus. *Nano Lett.* **17,** 1970-1977 (2017).
14. Yablonovitch, E. & Kane, E. O. Band structure engineering of semiconductor lasers for optical communications. *J. Lightwave Technol.* **6,** 1292-1299 (1988).
15. Thompson, S. E. et al. A 90-nm logic technology featuring strained-silicon. *IEEE Trans. Electron Dev.* **51,** 1790-1797 (2004).
16. Chen, Y. et al. Strain engineering and epitaxial stabilization of halide perovskites. *Nature* **577,** 209 (2020).
17. Lee, C., Wei, X., Kysar, J. W. & Hone, J. Measurement of the elastic properties and intrinsic strength of monolayer graphene. *Science* **321,** 385-388 (2008).
18. Bertolazzi, S., Brivio, J. & Kis, A. Stretching and breaking of ultrathin MoS_2. *ACS Nano* **5,** 9703-9709 (2011).
19. Rodin, A. S., Carvalho, A. & Neto, A. C. Strain-induced gap modification in black phosphorus. *Phys. Rev. Lett.* **112,** 176801 (2014).
20. Quereda, J. et al. Strong modulation of optical properties in black phosphorus through strain-engineered rippling. *Nano Lett.* **16,** 2931-2937 (2016).

21. Zhang, Z. et al. Strain-modulated bandgap and piezo-resistive effect in black phosphorus field-effect transistors. *Nano Lett.* **17,** 6097-6103 (2017).
22. Zhang, G. et al. Infrared fingerprints of few-layer black phosphorus. *Nat. Commun.* **8,** 14071 (2017).
23. Çakır, D., Sahin, H. & Peeters, F. M. Tuning of the electronic and optical properties of single-layer black phosphorus by strain. *Phys. Rev. B* **90,** 205421 (2014).
24. Huang, S. et al. Strain-tunable van der Waals interactions in few-layer black phosphorus. *Nat. Commun.* **10,** 2447 (2019).
25. Ma, W. et al. Piezoelectricity in multilayer black phosphorus for piezotronics and nanogenerators. *Adv. Mat.* **32,** 1905795 (2020).
26. Sanchez-Perez, J. R. et al. Direct-bandgap light-emitting germanium in tensilely strained nanomembranes. *Proc. Natl Acad. Sci. USA* **108,** 18893-18898 (2011).
27. Takei, K. et al. Quantum confinement effects in nanoscale-thickness InAs membranes. *Nano Lett.* **11,** 5008-5012 (2011).
28. Ling, X., Wang, H., Huang, S., Xia, F. & Dresselhaus, M. S. The renaissance of black phosphorus. *Proc. Natl Acad. Sci. USA* **112,** 4523-4530 (2015).
29. Ge, S. et al. Dynamical evolution of anisotropic response in black phosphorus under ultrafast photoexcitation. *Nano Lett.* **15,** 4650-4656 (2015).
30. Bhaskar, P., Achtstein, A.W., Vermeulen, M. J. W. & Siebbeles, L. D. A. Radiatively dominated charge carrier recombination in black phosphorus. *J. Phys. Chem. C* **120,** 13836-13842 (2016).
31. Chen, C. et al. Bright mid-infrared photoluminescence from thin-film black phosphorus. *Nano Lett.* **19,** 1488-1493 (2019).
32. Du, Y. et al. Auxetic black phosphorus: a 2D material with negative Poisson's ratio. *Nano Lett.* **16,** 6701-6708 (2016).
33. Wang, J. et al. Mid-infrared polarized emission from black phosphorus light-emitting diodes. *Nano Lett.* **20,** 3651-3655 (2020).
34. Zong, X. et al. Black phosphorus-based van der Waals heterostructures for mid-infrared light-emission applications. *Light: Sci. Appl.* **9,** 114 (2020).
35. Chang, T.-Y. et al. Black phosphorus mid-infrared light-emitting diodes integrated with silicon photonic waveguides. *Nano Lett.* **20,** 6824-6830 (2020).
36. Haug, A. Auger recombination in direct-gap semiconductors: band-structure effects. *J. Phys. C: Solid State Phys.* **16,** 4159 (1983).
37. Kurtz, S. R., Biefeld, R. M. & Dawson, L. R. Modification of valence-band symmetry and Auger threshold energy in biaxially compressed $InAs_{1-x}Sb_x$. *Phys. Rev. B* **51,** 7310 (1995).
38. Lee, D. D. & Lee, D. S. Environmental gas sensors. *IEEE Sens. J.* **1,** 214-224 (2001).
39. Dinh, T.-V., Choi, I.-Y., Son, Y.-S. & Kim, J.-C. A review on non-dispersive infrared gas sensors: improvement of sensor detection limit and interference correction. *Sens. Actuators, B* **231,** 529-538 (2016).
40. Gomes, J., Rodrigues, J. J., Rabêlo, R. A., Kumar, N. & Kozlov, S. IoT-enabled gas sensors: technologies, applications, and opportunities. *J. Sens. Actuator Netw.* **8,** 57 (2019).
41. Deng, Y. et al. Black phosphorus-monolayer MoS_2 van der Waals heterojunction p-n diode. *ACS Nano* **8,** 8292-8299 (2014).

42. Youngblood, N., Chen, C., Koester, S. J. & Li, M. Waveguide-integrated black phosphorus photodetector with high responsivity and low dark current. *Nat. Photonics* **9,** 247-252 (2015).
43. Yuan, H. et al. Polarization-sensitive broadband photodetector using a black phosphorus vertical p–n junction. *Nat. Nanotechnol.* **10,** 707-713 (2015).
44. Guo, Q. et al. Black phosphorus mid-infrared photodetectors with high gain. *Nano Lett.* **16,** 4648-4655 (2016).
45. Huang, M. et al. Broadband black-phosphorus photodetectors with high responsivity. *Adv. Mat.* **28,** 3481-3485 (2016).
46. Chen, X. et al. Widely tunable black phosphorus mid-infrared photodetector. *Nat. Commun.* **8,** 1-7 (2017).
47. Bullock, J. et al. Polarization-resolved black phosphorus/molybdenum disulfide mid-wave infrared photodiodes with high detectivity at room temperature. *Nat. Photonics* **12,** 601-607 (2018).
48. Amani, M., Regan, E., Bullock, J., Ahn, G. H. & Javey, A. Mid-wave infrared photoconductors based on black phosphorus-arsenic alloys. *ACS Nano* **11,** 11724-11731 (2017).
49. Wu, J., Mao, N., Xie, L., Xu, H. & Zhang, J. Identifying the crystalline orientation of black phosphorus using angle-resolved polarized Raman spectroscopy. *Angew. Chem. Int. Ed.* **54,** 2366-2369 (2015).
50. Castellanos-Gomez, A. et al. Deterministic transfer of two-dimensional materials by all-dry viscoelastic stamping. *2D Mater.* **1,** 011002 (2014).
51. Favron, A. et al. Photooxidation and quantum confinement effects in exfoliated black phosphorus. *Nat. Mater.* **14,** 826-832 (2015).
52. Foo, E., Jaafar, M., Aziz, A. & Sim, L. C. Properties of spin coated epoxy/silica thin film composites: effect of nano- and micron-size fillers. *Composites, Part A* **42,** 1432-1437 (2011).
53. Mei, H., Landis, C. M. & Huang, R. Concomitant wrinkling and buckle-delamination of elastic thin films on compliant substrates. *Mech. Mater.* **43,** 627-642 (2011).
54. Madelung, O. *Semiconductors: Data Handbook* (Springer, Berlin, ed. 3, 2004).
55. Kim, H. et al. Synthetic WSe_2 monolayers with high photoluminescence quantum yield. *Sci. Adv.* **5,** eaau4728 (2019).
56. Gramling, H. M. et al. Spatially precise transfer of patterned monolayer WS_2 and MoS_2 with features larger than 10^4 μm^2 directly from multilayer sources. *ACS Appl. Electron. Mater.* **1,** 407-416 (2019).
57. Nguyen, V. et al. Deterministic assembly of arrays of lithographically defined WS_2 and MoS_2 monolayer features directly from multilayer sources into van der Waals heterostructures. *J. Micro Nano-Manuf.* **7,** 041006 (2019).
58. Huang, Y. et al. Degradation of black phosphorus (BP): the role of oxygen and water. Preprint at https://arxiv.org/abs/1511.09201 (2016).
59. Qiao, J., Kong, X., Hu, Z. X., Yang, F. & Ji, W. High-mobility transport anisotropy and linear dichroism in few-layer black phosphorus. *Nat. Commun.* **5,** 1-7 (2014).

60. Desai, S. B. et al. Strain-induced indirect to direct bandgap transition in multilayer WSe_2. *Nano Lett.* **14,** 4592-4597 (2014).
61. Matthewson, M. J., Kurkjian, C. R. & Gulati, S. T. Strength measurement of optical fibers by bending. *J. Am. Ceram. Soc.* **69,** 815-821 (1986).
62. Plechinger, G. et al. Control of biaxial strain in single-layer molybdenite using local thermal expansion of the substrate. *2D Mater.* **2,** 015006 (2015).
63. Luo, W., Song, Q., Zhou, G., Tuschel, D. & Xia, G. Study of black phosphorus using angle-resolved polarized Raman spectroscopy with 442 nm excitation. Preprint at https://arxiv.org/abs/1610.03382 (2016).
64. Zhang, Z. M., Lefever-Button, G. & Powell, F. R. Infrared refractive index and extinction coefficient of polyimide films. *Int. J. Thermophys.* **19,** 905-916 (1998).
65. Sherrott, M. C. et al. Anisotropic quantum well electro-optics in few-layer black phosphorus. *Nano Lett.* **19,** 269-276 (2019).
66. Beal, A. R. & Hughes, H. P. Kramers-Kronig analysis of the reflectivity spectra of 2H-MoS_2, 2H-$MoSe_2$ and 2H-$MoTe_2$. *J. Phys. C* **12,** 881 (1979).
67. Hori, Y., Ando, Y., Miyamoto, Y. & Sugino, O. Effect of strain on band structure and electron transport in InAs. *Solid State Electron.* **43,** 1813-1816 (1999).
68. Delimitis, A. et al. Strain distribution of thin InN epilayers grown on (0001) GaN templates by molecular beam epitaxy. *Appl. Phys. Lett.* **90,** 061920 (2007).
69. Orsal, G. et al. Bandgap energy bowing parameter of strained and relaxed InGaN layers. *Opt. Mater. Express* **4,** 1030-1041 (2014).
70. Sanchez-Perez, J. R. et al. Direct-bandgap light-emitting germanium in tensilely strained nanomembranes. *Proc. Natl Acad. Sci. USA* **108,** 18893-18898 (2011).
71. Varshni, Y. P. Band-to-band radiative recombination in groups IV, VI, and III-V semiconductors (I). *Phys. Status Solidi* **19,** 459 (1967).
72. Vodopyanov, K. L., Graener, H., Phillips, C. C. & Tate, T. J. Picosecond carrier dynamics and studies of Auger recombination processes in indium arsenide at room temperature. *Phys. Rev. B.* **46,** 13194 (1992).
73. Rogalski, A. & Jóźwikowski, K. The intrinsic carrier concentration in $Pb_{1-x}Sn_xTe$, $Pb_{1-x}Sn_xSe$, and $PbS_{1-x}Se_x$. *Phys. Status Solidi* **111,** 559 (1989).
74. Klann, R., Höfer, T. & Buhleier, R. Fast recombination processes in lead chalcogenide semiconductors studied *via* transient optical nonlinearities. *J. Appl. Phys.* **77,** 277 (1995).
75. Marchetti, S., Martinelli, M. & Simili, R. The Auger recombination coefficient in InAs and GaSb derived from the infrared dynamical plasma reflectivity. *J. Phys. Condens. Matter* **14,** 3653-3656 (2002).
76. Ge, S. et al. Dynamical evolution of anisotropic response in black phosphorus under ultrafast photoexcitation. *Nano Lett.* **15,** 4650-4656 (2015).

5

Conclusion

2D semiconductors offer unprecedented tuning capability because their properties can be easily modulated using various knobs such as chemical/electrostatic doping and strain. In this dissertation, different strategies to overcome the inherent limitations of 2D semiconductors have been presented, which makes them advantageous over conventional bulk semiconductors for developing next-generation optoelectronic applications.

In Chapter 2, it is described that through proper material processing, 2D TMDC monolayers with high optoelectronic quality can be obtained in both mechanically exfoliated and synthesized samples. The encapsulation of monolayers with fluoropolymer followed by subsequent chemical counterdoping leads to highly stable and near-unity PL QY in MoS_2 and WS_2. A combination of optimized growth conditions and the simple substrate-decoupling method enables the high PL QY WSe_2 which can be synthesized in a centimeter scale.

In Chapter 3, entirely radiative TMDC monolayers at all exciton densities have been demonstrated. Because most optoelectronic devices operate at high photocarrier densities, degraded PL QY at high exciton densities in monolayer semiconductors, which is attributed to VHS has impeded their utility in practical applications. By applying small mechanical strain, we circumvent this VHS resonance and achieve near-unity PL QY in TMDC monolayers at all exciton densities, which paves the way for developing LEDs that will retain high efficiency at all brightness.

In Chapter 4, we utilize the strain-tunable bandgap of bP to demonstrate actively variable spectrum optoelectronic devices that are operating in infrared wavelengths at room temperature. Enabled by the extraordinary sensitivity of its bandgap to strain, bP-based LEDs and photodetectors show active spectrum tunability while retaining high performance. Our approach therefore presents a facile and general route to bypass the key challenges in conventional infrared optoelectronics,

representing a new class of devices.